



UNIVERSITY OF MESSINA  
DEPARTMENT OF ENGINEERING

PhD Course in Engineering and Chemistry of Materials and Construction  
XXXV cycle

MECHANICAL DESIGN OF A NOVEL  
LATTICE STRUCTURE

Tutor: Prof. Eng. Gabriella Epasto

Co-Tutor: Prof. Eng. Salvatore Pasta

Candidate:  
Fabio Distefano

SSD: ING/IND-14 – Progettazione meccanica e costruzione di macchine  
SSD: ING/IND-34 – Bioingegneria industriale

a.a. 2021/2022



---

## ABSTRACT

The main objective of the present PhD thesis is the design of a novel lattice material, named Triply Arranged Octagonal Rings (TAOR).

Lattice materials, thanks to their unique combination of properties, attract a great deal of interest in several engineering field, for instance automotive, aerospace and biomedical. The design and the subsequent investigations of the novel lattice material aimed to meet the mechanical and morphological requirements for biomedical applications.

Biomimetic theory, the Gibson-Ashby model and a static finite element (FE) analysis of regular polygons were taken into account in the development of the new lattice material. Eight octagons of the same dimensions were combined to each other forming a ring; to obtain an isotropic lattice structure, cubic symmetry was imposed, each unit cell is made of three rings mutually perpendicular, one ring for each principal direction.

Extensive experimental and numerical investigations were conducted to evaluate the mechanical performance of the TAOR lattice and assess its suitability for applications in biomedical devices used as bone substitutes.

Compressive tests were carried out and a comparison with other lattice materials currently used in the biomedical field was conducted. A scanning electron microscope (SEM) was useful to perform a morphological analysis in which the matching between designed and actual geometric parameters was evaluated. Moreover, SEM was used to evaluate the failure mode of the structures together with visual inspection. The Gibson-Ashby model was applied for the mechanical characterization of the TAOR cell. The model allows a direct comparison between the mechanical properties of given lattice materials and it helps to estimate their compressive behaviour. The mechanical properties, calculated through the compressive tests, were plotted in a graph against the relative density and their power-law relationships were estimated. The Gibson-Ashby model confirmed that the TAOR lattice presents a bending-dominated behaviour, already previously estimated from the application of the Maxwell stability criterion.

A linear static FE model of the TAOR lattice was developed to estimate its elastic modulus, the stress distribution within the structure and the cell size effect. Non-linear FE models of the single unit cell and of lattices with 2 or 3 unit cells for each specimen edge were developed. The model of the single unit cell aimed to investigate the compressive behaviour and the failure mode of the cell, without the presence of adjacent

cells that affect the deformation process. The model of the specimens aimed to evaluate the mechanical properties of the lattice material and compare the results with those obtained in the experimental tests.

The results of the investigations allow to assert that the proposed TAOR cell meets the mechanical and morphological requirements for application in the biomedical field, thus it can represent a relevant design choice to produce bone scaffold. Further investigations are needed to assess the TAOR suitability with the biological requirement for application in the biomedical field.

A case study, regarding the application of lattice structures in biomedical implants was conducted. In the present study, the rhombic dodecahedron, which is one of the most used lattice structures for applications in the biomedical field, was selected; in preparation for a future development of the research with the inclusion of the novel TAOR cell. The risk of subsidence was analysed for two different intervertebral body fusion devices. The subsidence represents a serious clinical issue during the healing process, mainly when the interfaces between the implant and the vertebral bodies are not well designed. The devices present the same shape, but one of them includes a filling rhombic dodecahedron structure. The effect of the lattice structure on the subsidence behaviour of the implants was evaluated by means of experimental tests and finite element analyses.

Compressive tests were carried out by using blocks made of grade 15 polyurethane, which simulate the vertebral bone. Non-linear, quasi-static finite element analyses were performed to simulate experimental and physiological conditions. The experimental tests and the FE analyses showed that the subsidence risk is higher for the device without the lattice structure, due to the smaller contact surface. Moreover, in this device an overload in the central zone of the contact surface was detected and it could cause the implant failure. On the contrary, the presence of the lattice structure allows a homogenous pressure distribution at the implant - bone interface.

The first part of the PhD was mainly focused on the study of strut-based lattice materials. To have a global view of the issue, a period of six months was spent at KU Leuven University in Belgium. During the stay, the focus of the research shifted on TPMS lattice materials. Compressive tests were carried out, in conformity to the ISO 13314 standard, to evaluate the mechanical behaviour of TPMS gyroid scaffolds. Gyroid lattice has been vastly investigated in literature and a wide range of mechanical properties have been evaluated; thus, an in-depth analysis was conducted to compare the results of the

compressive tests with published models from literature. The data of the experimental tests and of the selected models from literature were plotted in a Gibson-Ashby diagram. The comparison shows that the mechanical properties of all the selected models match well for lower relative densities, while the results diverge at the increase of the relative density.



# CONTENTS

<b>1. INTRODUCTION .....</b>	<b>1</b>
1.1. BACKGROUND .....	1
1.2. BASICS.....	1
1.2.1. Cellular solids .....	1
1.2.2. Additive manufacturing .....	4
1.2.3. Biomimetic design.....	5
1.3. OBJECTIVE OF THE THESIS .....	6
1.4. OUTLINE OF THE THESIS .....	8
<b>2. DESIGN OF A NOVEL UNIT CELL.....</b>	<b>9</b>
2.1. LATTICE STRUCTURES.....	9
2.1.1. Classification .....	9
2.1.2. Compressive behaviour.....	16
2.1.3. Properties .....	21
2.1.4. Fields of application.....	24
2.2. TAOR CELL .....	26
<b>3. MECHANICAL ANALYSIS OF LATTICE STRUCTURES.....</b>	<b>38</b>
3.1. EXPERIMENTAL ANALYSIS .....	38
3.1.1. Specimens production.....	38
3.1.2. Morphological analysis.....	41
3.1.3. Compressive tests .....	47
3.1.4. Gibson-Ashby diagram .....	50
3.1.5. Failure mode analysis .....	54
3.2. FINITE ELEMENT ANALYSIS .....	56
3.2.1. Linear static finite element analysis.....	56
3.2.2. Johnson-Cook constitutive material model.....	69
3.2.3. Finite element analysis of the single unit cell.....	77
3.2.4. Finite element analysis of the lattice structure.....	87
<b>4. MECHANICAL ANALYSIS OF POROUS DEVICES .....</b>	<b>91</b>
4.1. SUBSIDENCE OF INTERVERTEBRAL BODY FUSION DEVICES .....	91

4.2. DESCRIPTION OF THE DEVICES .....	93
4.3. EXPERIMENTAL INVESTIGATIONS.....	96
4.3.1. Experimental set-up.....	96
4.3.2. Experimental investigations results.....	98
4.4. FINITE ELEMENT ANALYSIS OF THE RISK OF SUBSIDENCE.....	100
4.4.1. Finite element models .....	100
4.4.2. Finite element analysis results.....	104
<b>5. EXPERIMENTAL ANALYSIS OF TPMS GYROID SCAFFOLDS .....</b>	<b>109</b>
5.1. GYROID SPECIMENS PRODUCTION .....	109
5.2. COMPRESSIVE TESTS OF GYROID LATTICES .....	114
5.3. GIBSON-ASHBY MODEL OF THE GYROID LATTICE .....	124
<b>6. CONCLUSIONS.....</b>	<b>127</b>
<b>FIGURES AND TABLES.....</b>	<b>131</b>
<b>REFERENCES .....</b>	<b>137</b>
<b>LIST OF PUBLICATIONS.....</b>	<b>157</b>

# **Chapter 1**

## **INTRODUCTION**

### **1.1. BACKGROUND**

Lattice materials attract a great deal of interest in several engineering disciplines, such as automotive, aerospace and biomedical fields thanks to their high strength to weight ratio, thermal conduction properties, and enhanced mechanical energy absorption [1], [2].

Three classes of lattice materials are currently studied for engineering applications; the first class is strut-based structures, while the second and third classes are derived from the mathematically created triply periodic minimal surfaces (TPMS), namely; the skeletal-TPMS and sheet-TPMS cellular structures [3].

In the recent years, the use of lattice structures in several engineering applications is grown increasingly due to the progress in Additive Manufacturing (AM). Freedom of design, mass customisation, waste minimisation and the ability to manufacture complex structures, as well as fast prototyping, are the main benefits of AM technologies [4].

The progress in AM also helped to exploit the potential of biomimetic (or biomimicry) design which can be increasingly realised in engineering applications. Biomimicry is the practice of learning from and emulating nature. In engineering it involves the study of biological systems, specifically with the aim to use the information learned from nature in solving engineering problems, or for use in engineering applications [5].

These topics will be discussed in detail in the present PhD thesis and will be applied for the design of a novel lattice material.

### **1.2. BASICS**

#### **1.2.1. Cellular solids**

A cellular solid is made up of an interconnected network of solid struts or plates which form the edges and faces of cells. It is a material with voids deliberately integrated in his structure [6]. In engineering field, three typical categories of cellular solids are studied: honeycombs, foams and lattices as shown in Fig. 1.

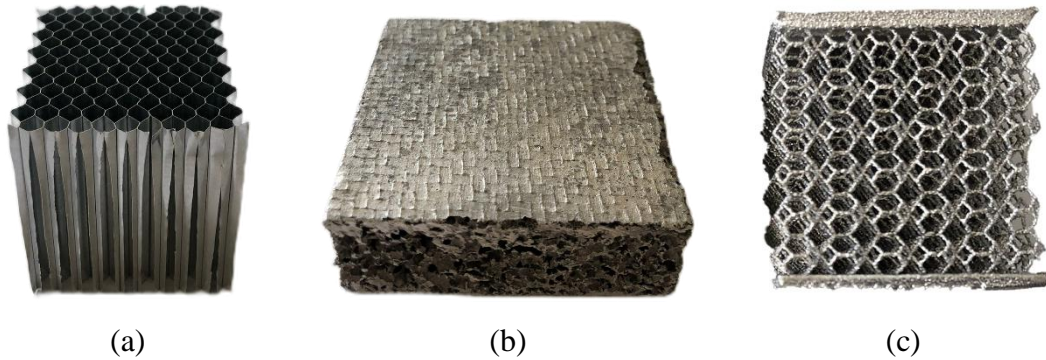


**Fig. 1** Cellular solids: (a) honeycomb; (b) foam; (c) lattice

The simplest structure is the honeycomb (Fig. 1a), a two-dimensional array of polygons which pack to fill a plane area like the hexagonal cells of the bee. More commonly, the cells are polyhedral having a random orientation, which pack in three dimensions to fill space; thus, the obtained three-dimensional cellular materials are called foams (Fig. 1b) [6]. Foams may be either open, with solid only at the edges of the polyhedra; or closed, with solid membranes over the faces of the polyhedra [7]. It can be seen that the microstructure of such a foam has a three-dimensional open-cell topology and may be represented by a tetrahedral repeating unit containing four struts [8]. In particular, [9] were the first to model open-cell foams with tetrakaidecahedral cells shown that the repeating strut corresponds to a regular tetrakaidecahedron with all of its vertices connected by slender struts and each vertex shared by four struts.

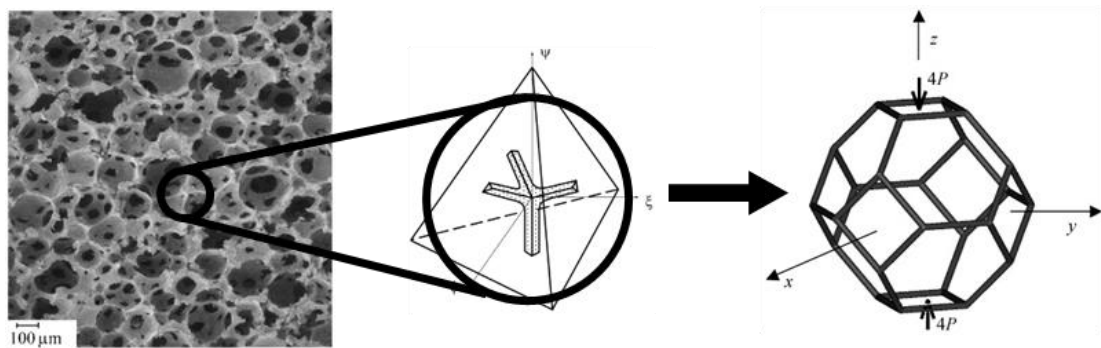


**Fig. 2** From foam to lattice structure [8]

When the unit cells are equiaxed and packed to fill a periodical pattern of struts with the same size, the properties of the foam are isotropic; in these cases, the structure are called lattice (Fig. 1c). The unit cells are defined by the dimensions and connectivity of their

constituent strut elements, which are connected at specific nodes [10]. Additive Manufacturing (AM) technologies allow to achieve several unit cell shapes and dimensions. Different shapes influence the mechanical properties of the lattice structure [11].

As above mentioned, a lattice is a connected network of struts. In the structural engineering, a lattice truss or space frame represents an array of struts, pin-jointed or rigidly fixed at their vertices, usually made of conventional materials, such as steel or aluminium. Lattice truss structures find application in different field, such us: civil engineering [12] or in the frame of quadcopter wings [13] with the aim to create stiff, strong load-bearing structures using as little material as possible. Referring to cellular solids lattice structures, they are also usually mentioned as lattice materials. These materials differ from the lattices of the structural engineering in one important regard: that of the scale. That of the unit cell of lattice materials is one of millimetres or micrometres, and it is this that allows them to be viewed both as structures and as materials. They can be analysed using classical methods of mechanics, just as any space frame is analysed. But they can also be seen as a new material, with its own set of effective properties, allowing direct comparison with those of the bulk material constituting the strut of the lattice structure [14].

The most important parameter to be determined in the analysis of a cellular solid is its relative density, defined as: the density of the cellular material, divided by that of the solid from which the cell struts/walls are made [6]. As the relative density increase, the cell struts thicken and the pore space shrinks; above 0.3 there is a transition from a lattice structure to a structure that can be thought as a solid containing isolated pores. Indeed, most of the known lattice structures only cover relative densities values from 0.1 up to 0.5 [15].

Cellular materials offer unique functional properties including high strength to weight ratio, heat dissipation and heat transfer control, and enhanced mechanical energy absorption. Justifiably, they attract a great deal of interest in several engineering disciplines, particularly for biomedical [16], aerospace [17] and automotive [18] fields. For biomedical applications lattice structures can be used to reduce the stiffness of metallic medical implants to be closer to that of bone [19] thereby avoiding stress shielding while allowing fluid flow due to their porosity with a large surface area-to-volume ratio to facilitate osseointegration [20]. The high strength-to-weight ratio and thermal conduction properties make them attractive for aerospace and automotive

applications [21]. Cellular materials find application as heat exchangers [22] due to their large surface area, as energy absorbers due to their ability to undergo great deformation at a relatively low stress level [23], and as acoustic insulators due to their large number of internal pores [24].

By tuning lattice structural parameters, such as cell topology or cell size and strut dimension, the physical response of these structures can be significantly altered to exhibit properties unachievable by their parent materials [10].

### 1.2.2. Additive manufacturing

Additive Manufacturing (AM) has grown considerably in recent years, with improvements in technology and resulting material properties. The ability to create components with complex parts with customisable material properties is one of the most important advantages of this technology, allowing the production of complex functional objects from various materials unattainable by conventional manufacturing methods [25]. This has led to the industrial use of AM parts even in highly critical applications, most notably in aerospace, automotive and biomedical applications. Different AM technologies are currently used for the fabrication of parts used in this fields, from metallic fine powders; for instance: Selective Laser Melting (SLM) [26], Direct Metal Laser Sintering (DMLS) [27], Electron Beam Melting (EBM) [28].

However, due to the rapid proliferation of a wide variety of technologies associated with AM, there is a lack of a comprehensive set of design principles, manufacturing guidelines, and standardization of best practices. AM techniques require process optimization and quality control to ensure accuracy and reliability [29]. This requirement is critically important for parts with complex geometries, such as lattice structures, which include curved surfaces and thin connecting features. Different factors such as machine selection, processes and materials, orientation and position of the geometry, and finishing can alter the resulting quality of the printed part [30]. A major limitation is the minimum feature size for the AM system used [31], the achievable feature resolution is inherently constrained by the fact that powder-based systems require particles that are larger than  $20\text{ }\mu\text{m}$  so that the powder can be successfully spread during the recoating step [32]. An additional limitation is placed on the part design, most notably the build angles [33]. When extremely complex structure such as truncated icosahedra are printed with dimensions in the order of micrometres, some feature cannot be reproduced [34]. An

important attribute is the surface quality, which is mainly determined by the thickness of each printed layer. Surface quality is also dependent on the form of the raw material; powder bed AM processes have poorer surface quality than others due to large and partially melted powder particles that reside on the printed part's surface [30].

In order to advance research interest and investments, AM technologies goal is to face these and other challenges to ensure the quality of the 3D printed products [35].

### 1.2.3. Biomimetic design

Biomimetic is the practice of learning from and emulating nature [5]. Benyus J.M. [36] defined biomimetic as “innovation inspired by nature” or alternatively, “the conscious emulation of nature’s genius”. In engineering, it involves the study of biological systems, specifically with the aim to use information learned from nature in solving engineering problems, or for use in engineering applications. The potential of biomimetic can be exploited in engineering applications due to progress in AM, with its freedom of design and complex production capabilities [5].

Two broad approaches of biomimetic design exist: problem driven design, which seek a solution from nature for a particular engineering problem; and solution driven design, which is inspired by an observation of nature, that leads to a technological design [37].

In addition to these approaches, three ways to design a biomimetic model exist: customised and freeform design, simulation driven design, cellular and lattice design. Customised and freeform design is typically used to directly replicate natural structures, with the aim to create custom and unique designs fit for a particular application while maintaining functionality [38]. This process is the simplest of the biomimetic design methods, particularly useful for customisation of biomedical implants, in which the design requirement is taken from a biological shape, hence the biomimetic description. Indeed, customised biomedical devices aim at directly replicating the bone shape for replacement [39]. Simulation driven design involves topology optimization and is especially useful for lightweight design. The method consists in an iterative process of simulation and material removal to optimize the required material distribution or material stiffness for a given set of expected load cases [40], [41]. This process of stepwise optimization is similar to most evolutionary processes in nature, and removal of material in areas of low stress is a similar optimization strategy as is used in natural systems, hence the motivation to categorize this process as biomimetic. The cellular and lattice design

approach is often combined with the other described methods; for instance, the incorporation of lattice structures into natural optimised or topology optimised designs [42]. Natural systems often consist of cellular structures and these are widely used in bio-inspiration for the use of lattices in engineering applications, hence the categorization as biomimetic. In a broader sense, this method can be applied to create a design principle without using any measurement, namely generic bio-inspiration; for instance, honeycomb structures used as lightweight design [43].

### 1.3. OBJECTIVE OF THE THESIS

The main objective and novelty of the thesis is the biomimetic design of a new lattice structure, named Triply Arranged Octagonal Rings (TAOR).

The design of a lattice structure cannot be performed following the rules and theories of classical mechanics; therefore, the Gibson-Ashby model, which is the most notable and commonly accepted model for the study of a lattice structure, was applied in the design and development of the novel lattice material. Moreover, Maxwell stability criterion was applied to estimate the deformation behaviour of the structure.

The design and the subsequent investigations of the novel TAOR lattice aimed to meet the mechanical and morphological requirements for applications in biomedical devices as bone substitutes. In the biomedical field, a successful porous metallic implant should restore the physiological function of the bone and promote bone regeneration and osteointegration, these are mechanically affected by the stiffness and the porosity of the implant. Despite recent advances in biomaterials and tissue engineering, repair of massive bone defect remains a challenge. Therefore, the goal of the proposed TAOR cell is to find a good compromise between low stiffness and adequate pore size, while maintaining appropriate mechanical strength of the implant.

An extensive experimental investigation was performed for the mechanical and morphological characterization of the TAOR lattice made of Ti6Al4V ELI alloy and produced via EBM. A comparison between TAOR cell and other lattice structures with similar geometric features that are currently used in the biomedical field have been performed to evaluate the mechanical suitability of the proposed lattice for applications in devices used as bone substitutes. Quasi-static compressive tests of lattice specimens were carried out: the morphological features, the microstructure and the fracture surfaces were observed with a scanning electron microscope (SEM) to analyse the failure modes

of the structures. Morphological analyses also included the surface roughness evaluation, which was performed by a confocal microscope.

Numerical models were implemented to investigate the mechanical performance of the TAOR lattice. A preliminary static FE model was developed to estimate the elastic modulus of the TAOR cell, the stress distribution within the lattice structure and the cell size effect. A non-linear FE model of TAOR and other lattice materials was developed to evaluate the compressive behaviour and the failure mode of the single cells, without the presence of adjacent cells that affect the deformation process. Finally, a non-linear FE model of TAOR specimens was developed to evaluate the mechanical properties of the lattice material and compare the results with those obtained in the experimental tests.

A case study regarding the application of lattice structures in intervertebral body fusion devices, made of Ti6Al4V ELI alloy and produced by EBM, was conducted. In the present study, the rhombic dodecahedron, which is one of the most used lattice structures for applications in the biomedical field, was selected; in preparation for a future development of the research with the inclusion of the novel TAOR cell. The risk of subsidence was analysed for two different types of lumbar devices by means of experimental tests and finite element analyses. The devices present the same shape, but one of them includes a filling lattice structure. The first implant is characterized by the presence of both porous and solid structures; the second implant has only a solid structure (not filled), with the same shape of the first case. Compressive tests were carried out by using blocks made of grade 15 polyurethane, which simulate the vertebral bone. Non-linear, quasi-static finite element analyses were performed to simulate the experimental and the physiological conditions.

The effect of the lattice structure on the subsidence behaviour of the implants was evaluated to verify the improvement of subsidence performance resulting from the introduction of the lattice structure, which ensure a smoother contact pressure at the vertebrae-cage interfaces without modifying the solid structure, which guarantees the mechanical stability of the implant.

The first part of the PhD was mainly focused on the study of strut-based lattice materials. To have a global view of the issue, a period of six months was spent at KU Leuven University in Belgium. The activity performed during this period is also part of the thesis of another PhD student. During the stay in Leuven, the focus of the research shifted on TPMS lattice materials. TPMS scaffolds have attracted considerable attention for

applications in the biomedical field in general and (bone) tissue engineering in particular, owing to their interesting combination of mechanical and biological properties.

Experimental tests were carried out with the aim to evaluate the mechanical properties of TPMS gyroid. A range of cylindrical scaffolds, made of Ti6Al4V ELI alloy, was designed varying the relative densities from 10% to 80% and produced via DMLS technology.

Compressive tests were performed, according to the ISO 13314 standard, on a universal testing machine equipped with a 250 kN load cell. Stiffness, compressive stress and strain, plateau stress and energy absorption were evaluated according to that standard, and their relationship to porosity was established.

Gyroid structure has been vastly investigated in literature and a wide range of mechanical properties have been evaluated; thus, an in-depth analysis was conducted to compare the results of experimental tests and published models from literature.

#### 1.4. OUTLINE OF THE THESIS

The thesis is outlined as follows:

Chapter 2 discussed in detail the current state of the art of lattice structures. In this chapter is presented the design of the new TAOR cell, and the steps that conducted to the final shape of novel lattice material have been detailed discussed.

Chapter 3 presented an extensive experimental and numerical investigation to evaluate the mechanical properties of the TAOR cell, and to assess its suitability for applications in the biomedical field as bone substitutes.

Chapter 4 presented a case study regarding the application of lattice structures intervertebral body fusion devices, to analyse the risk of subsidence of such devices.

Chapter 5 presented the activity performed during the period spent at KU Leuven University, regarding the evaluation of the mechanical properties of TPMS gyroid lattice.

Chapter 6 highlighted the main conclusions.

## Chapter 2

# DESIGN OF A NOVEL UNIT CELL

### 2.1. LATTICE STRUCTURES

#### 2.1.1. Classification

Lattice structures are topologically ordered structures based on one or more repeating unit cells [44]. From the study of Gibson-Ashby on cellular solids, the unit cells are defined by the dimensions and connectivity of their constituent strut elements, which are connected at specific nodes [6].

Three classes of lattice structures are commonly studied in literature: the first class is strut-based structures, while second and third classes are derived from the mathematically created triply periodic minimal surfaces (TPMS), namely; skeletal-TPMS and sheet-TPMS lattice structures.

During their study, Gibson-Ashby developed a strut-based unit cell [6], [45], as shown in Fig. 3.

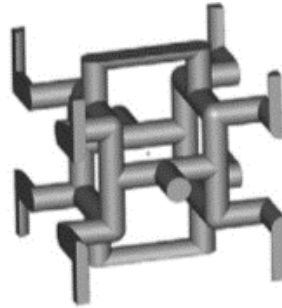


**Fig. 3** Gibson-Ashby lattice structure

The most common strut-based cell topologies that have been investigated, which are named after analogous crystalline structures, are body centred cubic (BCC) and face centred-cubic (FCC), or variations of these, which include the z-struts: BCCZ and FCCZ. Other strut-based topologies also exist, such as the cubic, octet-truss and diamond. In Fig. 4 are shown strut-based lattice structures.

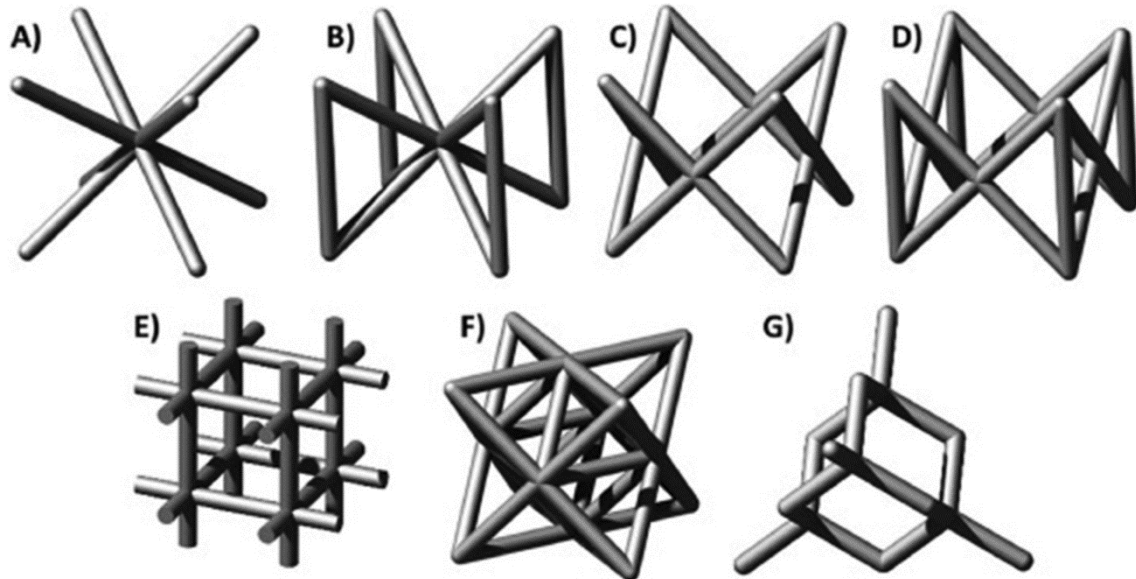


**Fig. 4** Strut-based lattice structures: (a) BCC; (b) BCCZ; (c) FCC; (d) FCCZ; (e) cubic; (f) octet-truss; (g) diamond [10]

The octet-truss cell is composed of an octahedral cell (black part) and a tetrahedral cell (light grey part), as shown in Fig. 5.

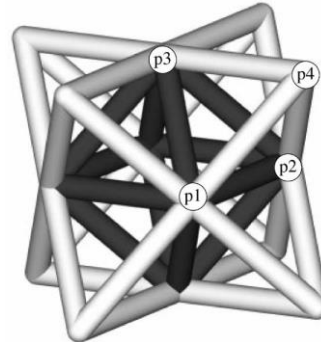


**Fig. 5** Structure of the octet-truss lattice material [46]

Other variations of the BCC lattice are represented by the G7 unit cell and the simple cubic body centred cubic (SCBCC) as shown in Fig. 6.

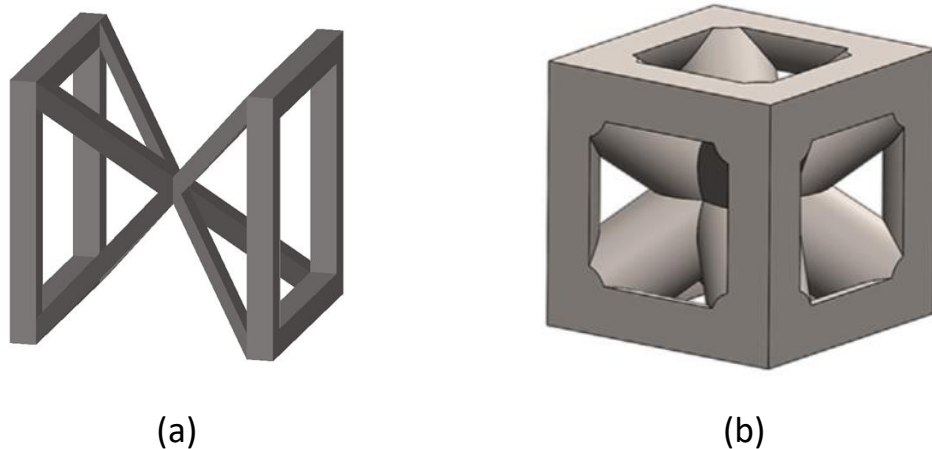


**Fig. 6** BCC derived lattice structures: (a) G7; (b) SCBCC [15]

Lattice materials with cubic symmetry, strut-based cell topology such as Archimedean solids or Catalan solids have also been vastly investigated over the years. Archimedean solids are a group of 13 solids, first enumerated by Archimedes. They are convex uniform polyhedra composed of regular polygons meeting in identical vertices. Catalan solids are the dual polyhedron of the Archimedean solids. Most studied Archimedean solids include cuboctahedron [47], [48], truncated cube [49], [50], truncated octahedron (Kelvin cell) [51], [52], rhombicuboctahedron [50], [53], truncated cuboctahedron [50], [54]. Among Catalan solids, researchers mostly focused their study on the rhombic dodecahedron [50], [55]. In Fig. 7 are shown lattice structures based on Archimedean and Catalan solids.

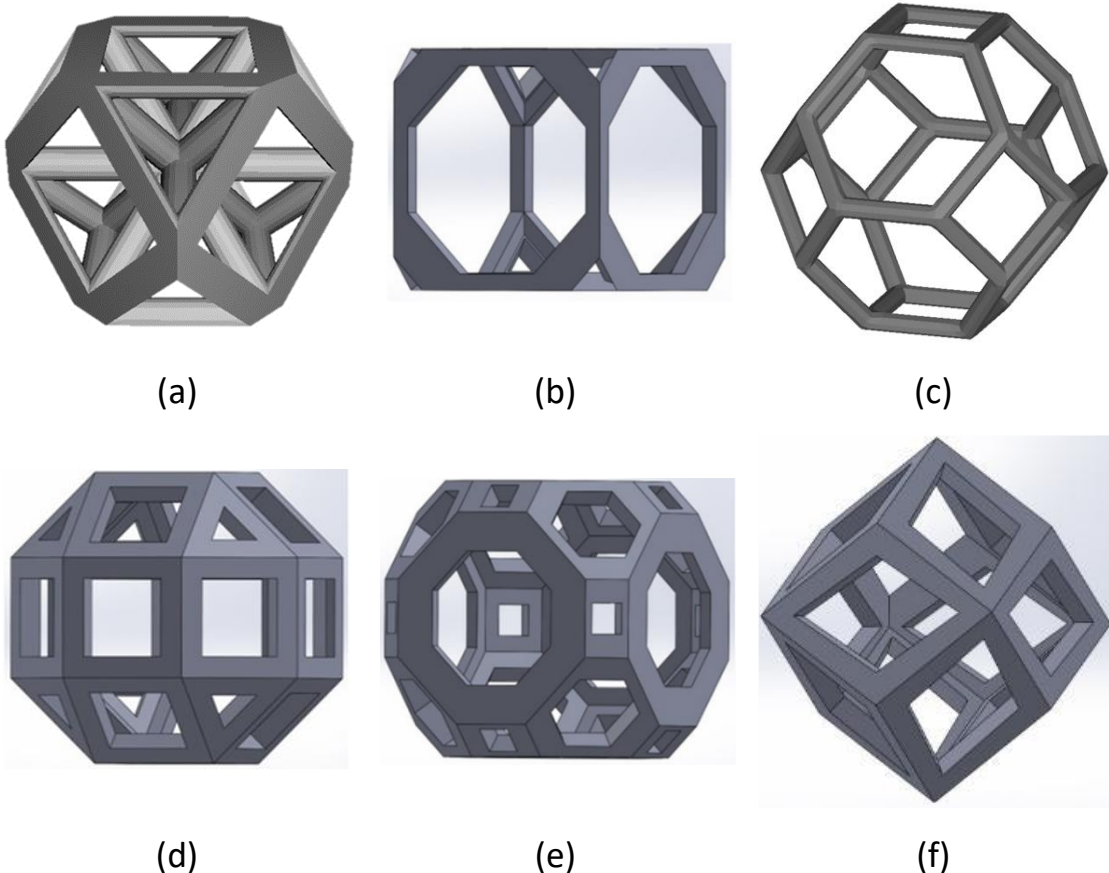


**Fig. 7** Archimedean and Catalan solids lattice structures: (a) cuboctahedron; (b) truncated cube; (c) truncated octahedron (Kelvin); (d) rhombicuboctahedron; (e) truncated cuboctahedron; (f) rhombic dodecahedron [48], [50]

Recently, focus shifted towards cellular structures with mathematically defined architectures, that is TPMS based topologies [3]. A minimal surface is a surface that have its mean curvature equal to zero in all points; thus, a TPMS is characterised as a minimal surface which is periodic in three independent directions [56]. TPMS mathematical representation is defined by a system of coordinates, these can be calculated using the Enneper-Weierstrass parametric representation as follows.

$$\begin{cases} x = \operatorname{Re} \left( e^{i\theta} \int_{w_0}^w (1 - \tau^2) R(\tau) d\tau \right) \\ y = \operatorname{Re} \left( e^{i\theta} \int_{w_0}^w i(1 - \tau^2) R(\tau) d\tau \right) \\ z = \operatorname{Re} \left( e^{i\theta} \int_{w_0}^w 2\tau R(\tau) d\tau \right) \end{cases} \quad (1)$$

Where  $\tau$  is a complex variable,  $\theta$  is the Bonnet angle,  $R(\tau)$  represents a function that varies for different TPMS and can be expressed as follows.

$$R(t) = \frac{1}{\sqrt{1 - 14t^4 + t^8}} \quad (2)$$

Compared to the parametric form, a TPMS has a simpler and unified representation, which can be express by sinusoid terms, and can be explicitly defined as follows.

$$\varphi(\gamma) = \sum_{k=1}^K A_k \cos \left[ \frac{2\pi(h_k \cdot \gamma)}{\lambda_k} + p_k \right] = C \quad (3)$$

where  $\gamma$  represents position vectors in Euclidean space,  $A_k$  denotes the amplitude factor,  $h_k$  is the  $k$ <sub>th</sub> grid vector in the reciprocal space,  $\lambda_k$  stands for the periodic wavelength,  $p_k$  represents the phase offset and  $C$  is a constant factor related to porosity [56]. More generally, the TPMS can be approximately defined as combinations of trigonometric functions in an implicit form. The most common TPMS unit cells include: Schwarz primitive, gyroid, diamond, IWP and their equations in the implicit form are expressed as follows (Michielson and Kole, 2003):

$$\varphi_{\text{primitive}} \equiv \cos x + \cos y + \cos z = C \quad (4)$$

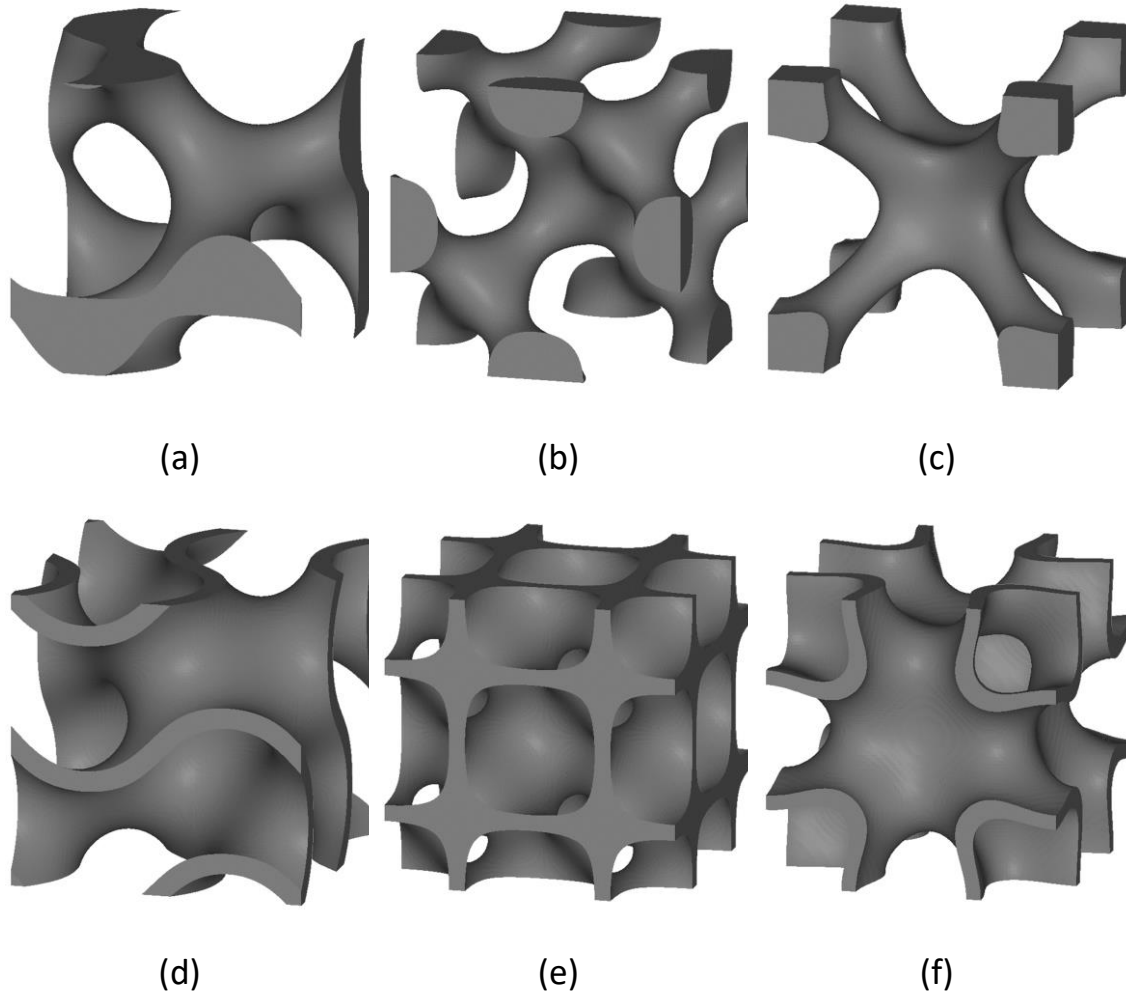
$$\varphi_{\text{gyroid}} \equiv \sin x \cos y + \sin z \cos x + \sin y \cos z = C \quad (5)$$

$$\varphi_{\text{diamond}} \equiv \cos x \cos y \cos z - \sin x \sin y \sin z = C \quad (6)$$

$$\begin{aligned}\varphi_{IWP} \equiv & 2(\cos x \cos y + \cos y \cos z + \cos z \cos x) \\ & - (\cos 2x + \cos 2y + \cos 2z) = C\end{aligned}\quad (7)$$

Two classes of TPMS lattices can be considered, namely: sheet TPMS and skeletal TPMS. Some TPMS structures have been investigated in both versions, such as: gyroid [58], [59], diamond [60], [61] and IWP [62], [63]. Other TPMS structures have been studied only in the sheet-based version: Schwarz primitive [64], [65], FRD [62], [66] and Neovius [67], [68]. In Fig. 8 are shown the most studied TPMS lattice structures.

It can be noticed that diamond cell is present in all the three classes of lattice structures. However, strut-based diamond and TPMS diamond are structures conceptualised and developed in different ways. As well as G7 and SCBCC lattices, also IWP is a BCC derived structure.



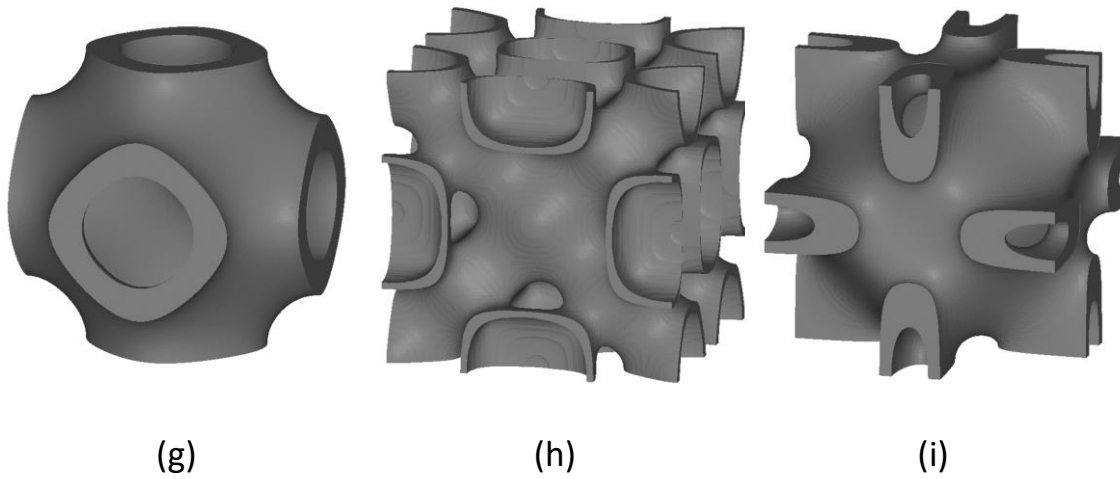


**Fig. 8** TPMS lattice structures: (a) skeletal gyroid; (b) skeletal diamond; (c) skeletal IWP; (d) sheet gyroid; (e) sheet diamond; (f) sheet IWP; (g) Schwarz primitive; (h) FRD; (i) Neovius

Several studies proposed novel unit cells, as shown in Fig. 9. Cao et al. [69] designed a lattice structure based on the Schwarz unit cell by using a MATLAB script to generate, transform and export the P-Lattice unit cell. Mahbod et al. [70] proposed a novel unit cell named double pyramid dodecahedron and developed by deriving the analytical relations in order to estimate the mechanical properties of the structure. Alomar et al. [71] designed a new lattice structure with a circular-based constituent cell.

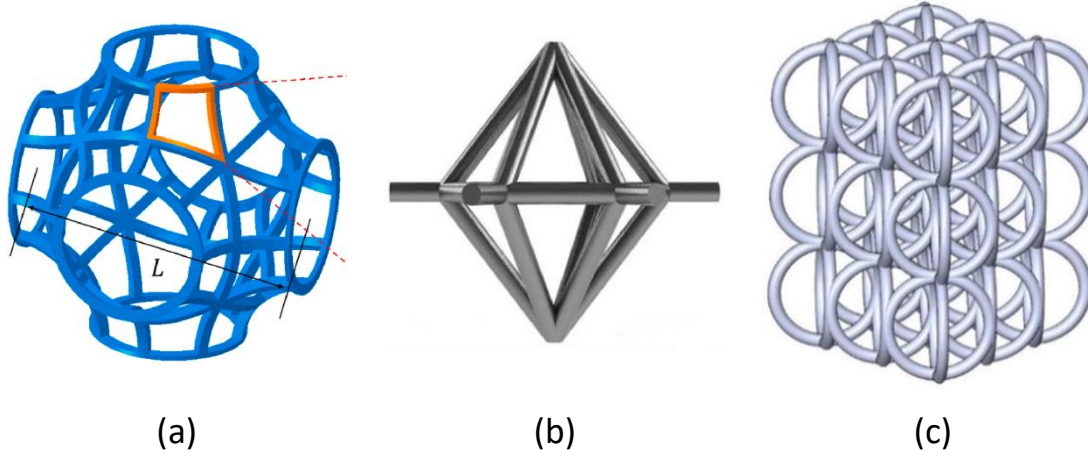
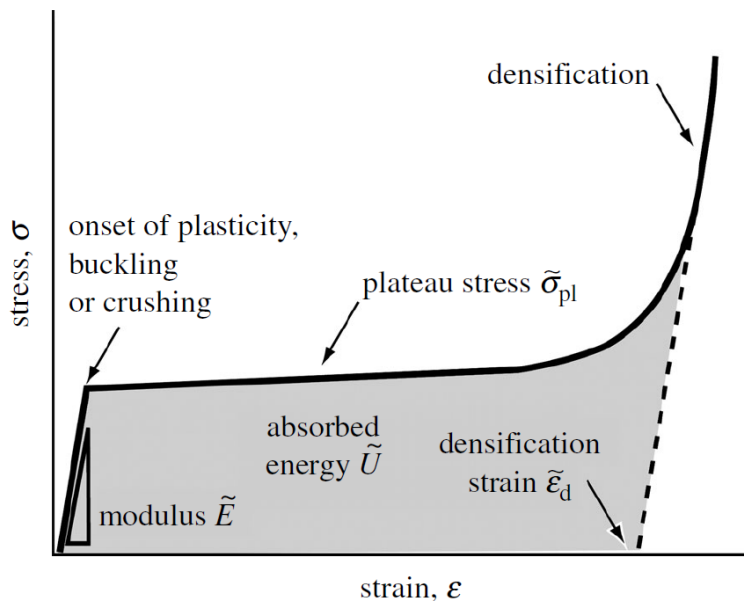


**Fig. 9** Novel lattice structure present in literature [69]–[71]

### 2.1.2. Compressive behaviour

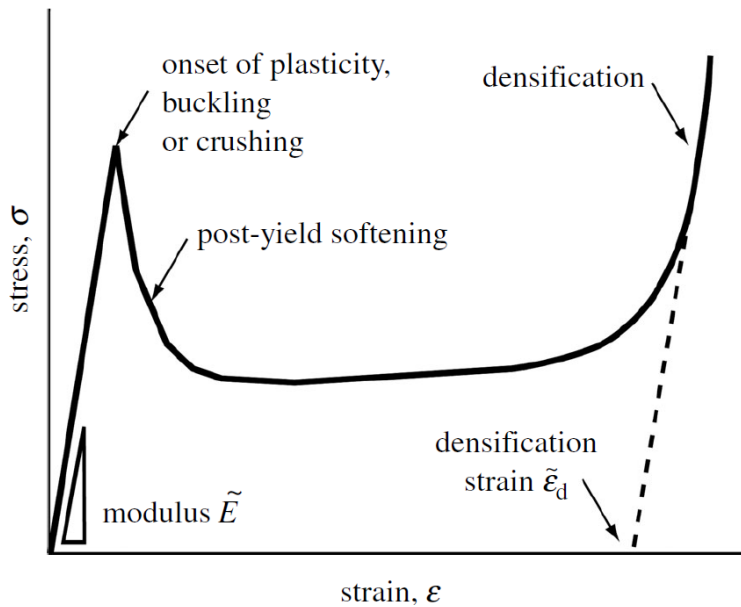
Lattice structure can be categorised based on their mechanical response as bending-dominated or stretch-dominated. Bending-dominated structures are compliant and absorb energy well when compressed, stretch-dominated structures have greater stiffness and compressive strength compared to bending-dominated lattices, for a given relative density [14].

Fig. 10 shows the compressive stress-strain curve of a bending-dominated lattice.



**Fig. 10** Stress-strain curve of a bending-dominated lattice [14]

The deformation behaviour can be divided into three stages: linear elastic deformation, plastic deformation and densification. In the first stage, the lattice material response is linear elastic with a Young's modulus proportional to the structure material's elastic modulus. The struts of lattice structures are susceptible to three collapse mechanism under compression: yield, buckling or crushing. They compete until the mechanism with the lowest stress threshold is reached. Once the elastic limit is reached, plastic deformation begins and the structure continues to collapse at a nearly constant stress, referred to as the plateau stress, until opposite side of the cells impinge, constraining further deformation. The densification strain is reached, and densification begins as stress rises steeply [10], [14]. Fig. 11 shows the compressive stress-strain curve of a stretch-dominated lattice.



**Fig. 11** Stress-strain curve of a bending-dominated lattice [14]

When subjected to a tensile/compressive loading, a stretch-dominated lattice material first responds by the elastic stretch of the struts; on average, in the first stage of the curve only one-third of its strut bears loads [14]. Also in this case, the elastic limit is reached when one or more sets of struts yield plastically, buckle or crush. Once the elastic limit is reached, the whole lattice material bears the loads and the structure fails by strut fracture. The stretch-dominated mechanisms of deformation involve hard modes (stretching) compared to the soft ones (bending) of the bending-dominated structures; therefore, initial yield is followed by plastic buckling or brittle collapse of the struts, leading to post yield softening, with oscillation of the stress required for further deformation. After that, the densification strain is reached and the stress steeply increase.

The deformation behaviour of strut-based topologies can be estimated by the Maxwell's stability criterion, by evaluating the Maxwell number  $M$ , which is dependent on the number of struts  $S$  and nodes  $N$  of the lattice material.

$$M = S - 3N + 6 \quad (8)$$

If  $M < 0$ , the structure is bending dominated; if  $M \approx 0$ , the structure is stretching-dominated; if  $M > 0$ , the structure is over-stiff [72].

The Gibson-Ashby model is the most notable and commonly accepted model for the prediction of the mechanical properties of lattice structure [6]. Mechanical properties are dependent on the type of response exhibited by the structure (bending or stretch-dominated) and have a positive power relationship with the structure's relative density. Gibson-Ashby provided the formulae relating elastic modulus and strength of a lattice structure to its relative density:

$$\frac{E^*}{E_s} = C_1 \left( \frac{\rho^*}{\rho_s} \right)^{n_1} \quad (9)$$

$$\frac{\sigma^*}{\sigma_s} = C_2 \left( \frac{\rho^*}{\rho_s} \right)^{n_2} \quad (10)$$

Where  $E^*$  and  $\sigma^*$  are the elastic modulus and the compressive strength of the lattice structure,  $E_s$  and  $\sigma_s$  are the elastic modulus and the compressive strength of the parent material.  $C_1$ ,  $n_1$ ,  $C_2$ ,  $n_2$  are constant values dependent on the unit cell topology and are derived from experimental tests.

The exponent  $n$  values can be predicted based on the lattice deformation behaviour. In a stretching-dominated structure, both stiffness and strength scales linearly as a function of the relative density and are higher than that of bending-dominated structures in which elastic modulus scale quadratically with the relative density, while the strength scales with a factor of 3/2 [3].

The results of the experimental tests can be summarised in a graph in which relative elastic modulus and relative strength are plotted against relative density, as shown in Fig. 12 and Fig. 13. By the interpolation of the data, the constant values reported in equations 9 and 10 can be calculated for a given lattice structure.

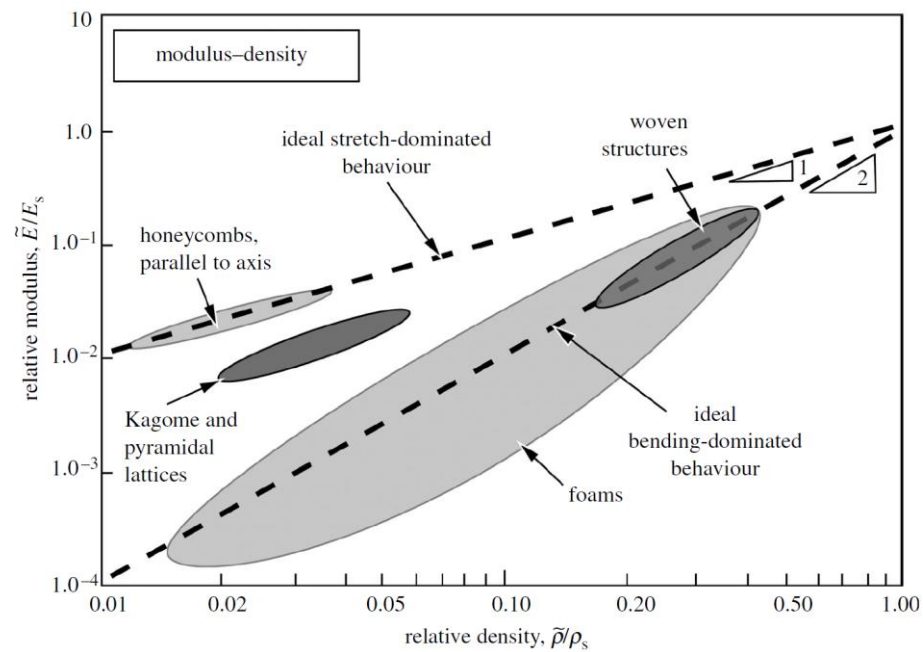


**Fig. 12** Gibson-Ashby model: relative modulus against relative density [14]

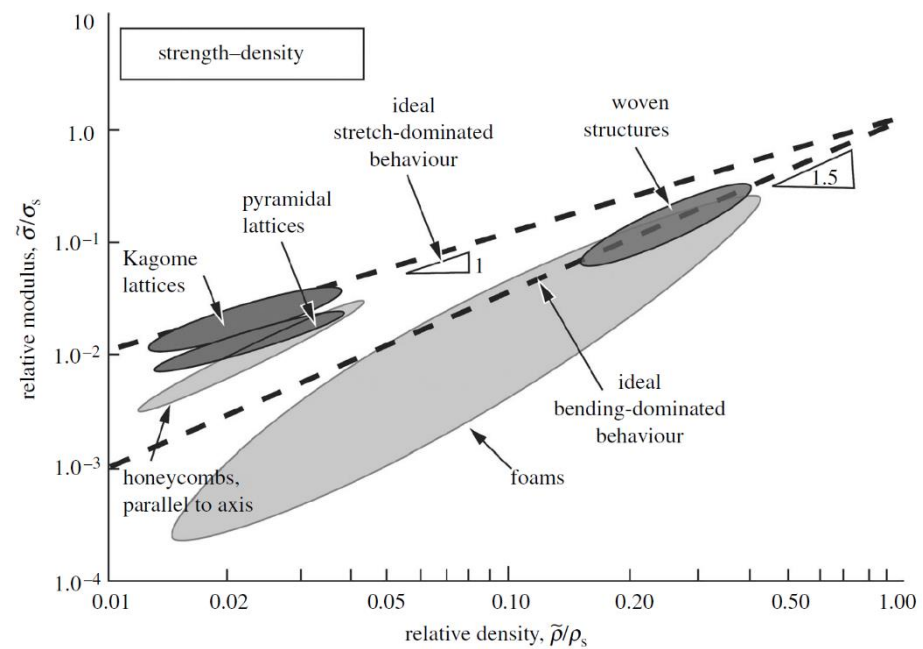


**Fig. 13** Gibson-Ashby model: relative strength against relative density [14]

During the deformation process, three compressive failure modes can be distinguished: successive cell collapse, propagation of cracks through the lattice and diagonal shear [73]. Cells collapse appears in planes perpendicular to the loading direction due to buckling or crushing, as shown in Fig. 14.

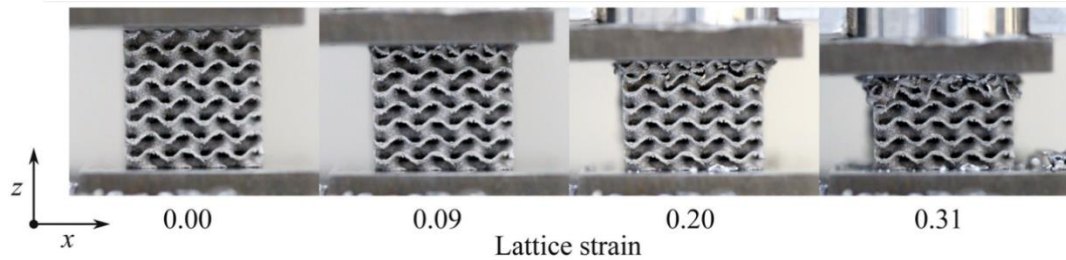


**Fig. 14** Successive cell collapse failure mode [73]

Crack propagation usually originates from a pre-existing defect, such as an internal pore or surface irregularity, as shown in Fig. 15.

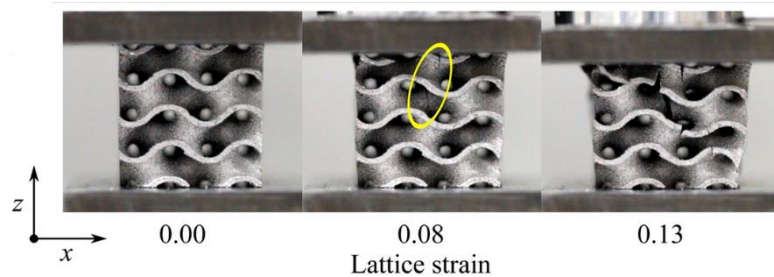


**Fig. 15** Crack propagation through the lattice failure mode [73]

Diagonal shear results in an initial loss of around 50% strength, followed by a uniform strengthening during densification, as shown in Fig. 16.

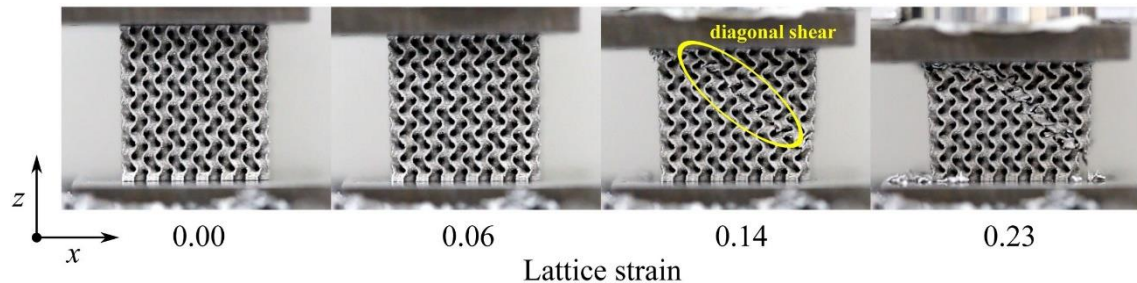


**Fig. 16** Diagonal shear failure mode [73]

### 2.1.3. Properties

As described in section 1.2.1. the most important parameter to be determined in the analysis of a cellular solid is its relative density  $\rho^*/\rho_s$ , defined as: the density of the cellular material, divided by that of the solid from which the cell struts/walls are made [6]. It can also be expressed in terms of volume fraction, as the ratio between the volume occupied by the strut  $V_{strut}$  of the unit cell and total volume  $V_{tot}$  of the geometry [74]:

$$\frac{\rho^*}{\rho_s} = \frac{V_{strut}}{V_{tot}} \quad (11)$$

The porosity, calculated as percentage value, is defined as the inverse function of the relative density:

$$\text{Porosity (\%)} = \left(1 - \frac{\rho^*}{\rho_s}\right) \cdot 100 \quad (12)$$

The geometric parameters that characterise the strut-based and the TPMS skeletal lattice structures are reported in Fig. 17.

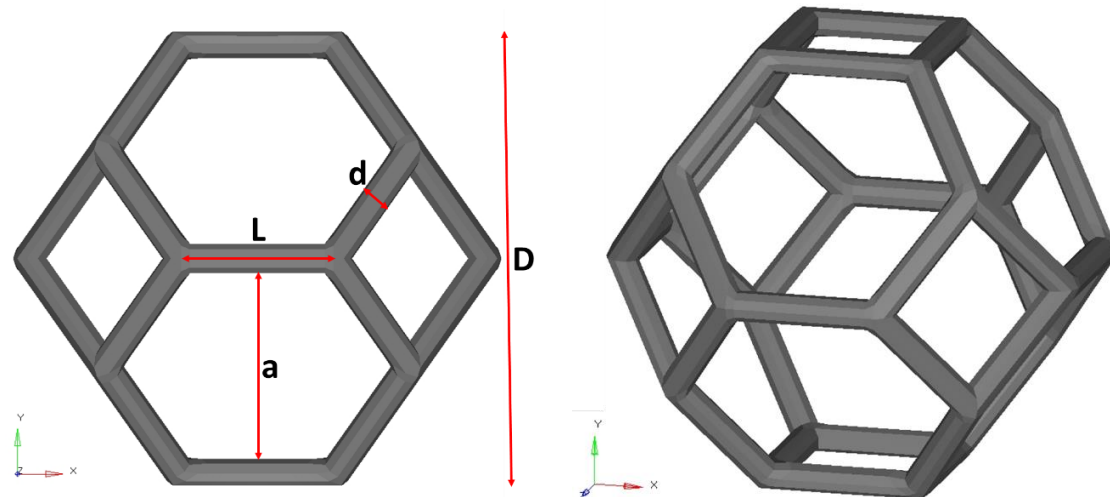


**Fig. 17** Geometric parameters of the truncated octahedron (strut-based) lattice structure

Where D is the cell size, d is the strut diameter, L is the edge length and a the pore size. The geometric parameters that characterise the TPMS sheet lattice structures are shown in Fig. 18.

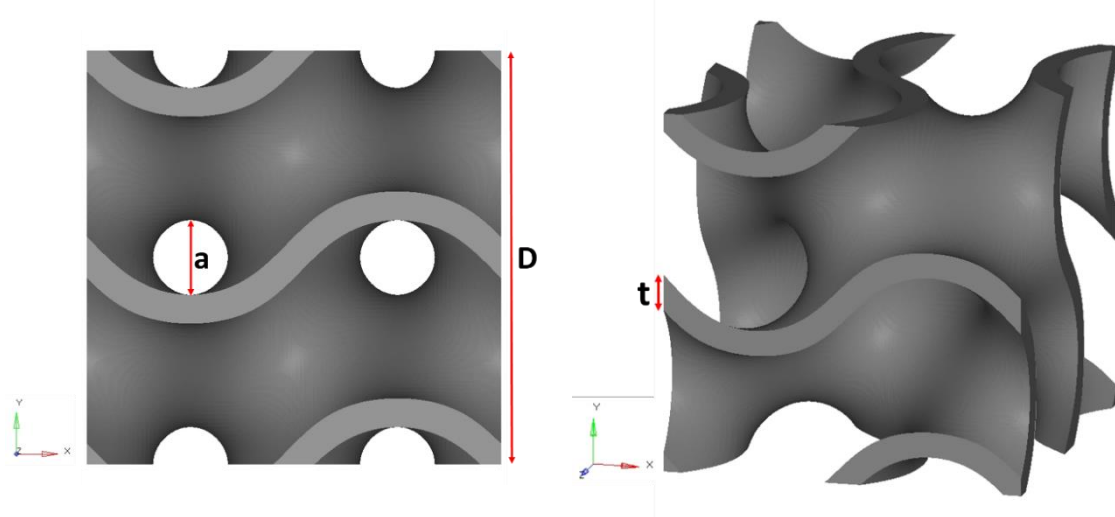


**Fig. 18** Geometric parameters of the TPMS gyroid (sheet-based) lattice structure

Where t is the wall thickness.

Research efforts were invested to find the most optimum cell topology that can provide the best mechanical properties with the least amount of material invested. As a result, several studies focused on the role of cell topology on enhancing the mechanical properties.

Al-Ketan et al. [3] evaluated the mechanical properties of various strut-based, TPMS skeletal and TPMS sheet lattice structures by carrying out compressive tests. Results showed that TPMS sheet lattice materials exhibited a near stretching-dominated deformation behaviour, while TPMS skeletal showed a bending-dominated behaviour. The Kelvin and Gibson-Ashby structures exhibited a mixed mode of deformation while the Octet-truss showed a stretch-dominated behaviour. TPMS sheet lattices showed superior mechanical properties among all the tested structures. TPMS diamond showed the best mechanical performance with nearly independence of relative density. It was also observed that at decreased relative densities the effect of the geometry on the mechanical properties is more pronounced.

Ahmadi et al. [50] studied the relationship between relative density and the compressive properties (elastic modulus, maximum stress, plateau stress, yield stress and energy

absorption) of strut-based lattice materials including various Archimedean and Catalan solids and the strut-based cubic and diamond. Each of the compressive properties increased with increase in relative density, with a power law type relationship. Results showed that structures may be divided into two groups: those that are stiff, such as cubic, truncated cube, truncated cuboctahedron, rhombicuboctahedron; and those that are compliant, including diamond and rhombic dodecahedron.

Abueidda et al. [75] investigated experimentally and computationally the mechanical properties of three TPMS sheet lattice materials; showing that for a given relative density, the specimens sizes affect the mechanical properties. The Neovius and IWP lattices have a similar mechanical response, and it is found that they have higher stiffness and strength than the Schwarz primitive structure.

Zhang et al. [76] investigated the mechanical properties and energy absorption capabilities of three types of TPMS sheet lattice (Schwarz primitive, diamond and gyroid) and strut-based BCC lattice structure. Compressive test results reveal the superior stiffness, plateau stress and energy absorption ability of TPMS sheet structures compared to the BCC lattice, with sheet diamond performing best. Non-linear FE analysis results also show that diamond and gyroid sheet structures display relatively uniform stress distributions across all lattice cells under compression, leading to stable collapse mechanisms and desired energy absorption performance. In contrast, Schwarz primitive lattice display rapid diagonal shear band development followed by localized wall buckling.

Mazur et al. [77] experimentally investigated the role of cell topology, cell size, number of unit cells on the mechanical performance of various strut-based lattice materials made of titanium and aluminium alloys. They analysed the mechanical properties as well as deformation and failure characteristics and compared them with theoretically predicted behaviour. BCC structure shows the lowest elastic modulus, attributable to its high structural compliance caused by under-stiff behaviour. The highest observed elastic modulus was exhibited by FBCCXYZ lattice for titanium alloy and FBCCZ structure for aluminium alloy. However, the highest specific modulus was exhibited by FCCZ structure. BCC structures exhibit the lowest overall and specific compressive strengths. For titanium alloy, FBCCXYZ and FCCZ structures showed high overall and specific strength values, respectively. For aluminium alloy, FBCCZ and FCCZ structures showed high overall and specific strength values, respectively. Failure modes of tested lattices structures under compression occurred through pronounced bending of diagonal struts

and buckling of vertical struts, followed by strut fracture and subsequent lattice cell collapse predominantly across diagonal shear bands. For topologies with a low Maxwell number and no struts aligned in the loading direction, such as BCC and FCC, significant deflection occurred before failure. For topologies with a high lateral stiffness, i.e., FBCCZ and FBCCXYZ, failure was observed by horizontal layer crushing. The observed response of lattice structures is in accordance with the theoretical response of bending and stretch dominated structures. However, topologies which were classified as bending-dominated according to the Maxwell criterion (FCCZ and FBCCZ) were found to correspond with stretch-dominated behaviour. Authors attributed this result to the presence of vertical struts aligned with the loading direction, which exhibited stretch-dominated deformation mechanisms. The results highlighted that the Maxwell criterion is a necessary but not sufficient condition for predicting mechanical response.

#### 2.1.4. Fields of application

As described in section 1.2.1., lattice structures find application in different fields, thanks to their combination of properties, for instance: aerospace, automotive, biomedical.

The lightweight concept of lattice structures means they are of great interest to the aerospace and aeronautic industries. These fields leverage the benefits of lattice structures, in the replacement of internal solid volumes with lattices with a similar strength, aiming to increase the performance-to-weight ratio of components to improve the efficiency of the vehicles [78]. Thermal properties of lattice materials, such as the ability to produce conformal cooling channels also makes them an attractive option for applications in these fields [21]. Thermal controllers are important components to manage the temperature of various electronics parts, yet traditional designs considerably add to the spacecraft's weight. The use of lattice sandwich structures, allow to produce thermal controllers with 50% increased thermal capacity compared to traditional alternatives with similar mass [79].

Applications of lattice structures in the automotive industry have also been developed to reduce weight, decrease noise conduction, and increase the ease of recycling automotive parts [80]. The energy absorption properties of the lattice structures are particularly attractive for protective applications in aerospace and automotive fields. As the lattice materials are able to propagate energy through their structure, they are very useful in distributing an impact shock across the object and therefore serve as a sacrificial

protection [81].

Lattice materials are widely used in the biomedical field, for applications in devices used as bone substitutes [82]–[88]. Bone is a complex tissue that continually undergoes dynamic biological remodelling, this feature of bone underpins its ability to remodel itself to repair damage [89]. However, the bone's ability for self-regeneration of massive defects can be limited because of deficiencies in blood supply or in the presence of systemic disease [90]. Therefore, when a bone defect exceeds a critical non-healable size, external intervention is required to supplement self-healing if the defect is to be bridged. Despite recent advances in biomaterials and tissue engineering, repair of such a critical bone defect remains a challenge [91]. Implants made of metals and alloys are usually stiffer than human bones, this may lead to stress shielding, which represents a major issue for bone resorption and eventual failure of the implants [92]. Cortical bone has elastic modulus ranging from 3 to 30 GPa, while cancellous bone has significantly lower elastic modulus, between 0.02 and 2 GPa [89]. The regulation of the internal architecture of a lattice structure, i.e., porosity, pore size, and pore interconnectivity, can lower the equivalent elastic modulus of the bulk implant material, thus matching the mechanical requirements of bone substitutes, to reduce or eliminate stress shielding, and to meet anatomic loading requirements to avoid mechanical failure [93], while maintaining appropriate mechanical strength of the implant [89], [94]; indeed, porous scaffolds also have load-bearing function. A successful porous metallic implant should restore the physiological function of the bone and promote bone regeneration and osteointegration. An ideal bone scaffold should possess the following characteristics: biocompatibility, suitable surface for cell attachment, proliferation, differentiation and migration [89]. Such abilities of bone-lining cells are affected by the size and shape of the scaffold pores; higher porosity promotes cell ingrowth and transport of nutrients [95]. Several studies evaluated the influence of pore size on the bone ingrowth. Although there are controversial views, the consensus seems to be that the optimal pore size for bone ingrowth is 100–400  $\mu\text{m}$  [89]. Itala et al. [96] implanted triangle-shaped titanium implants of 250 and 500  $\mu\text{m}$  thickness with pore size ranging from 50 to 125  $\mu\text{m}$  into rabbit femur and found that the amount of ingrown new bone was independent of the pore size and implant thickness. Bai et al. [97] suggested a 400  $\mu\text{m}$  upper limit of pore size for vascularization, beyond which no significant differences were observed with increasing pore sizes. Taniguchi et al. [98] implanted 300  $\mu\text{m}$ , 600  $\mu\text{m}$  and 900  $\mu\text{m}$  titanium porous scaffolds into rabbit tibia and they found that 600  $\mu\text{m}$  and 900  $\mu\text{m}$  scaffolds demonstrated

significantly higher bone ingrowth than 300 µm scaffolds.

In addition, another factor that affects bone ingrowth is the specific surface area of scaffolds. Implants with smaller pores are considered to have larger surface area and therefore more space for bone tissue ingrowth [89]. An important feature of porous implants is their permeability, since the transportation of cells, nutrients and growth factors require the flow of blood through the porous scaffolds. High permeability of titanium implants enhances the osseointegration process [99].

In summary, porosity, pore size and pore interconnectivity are important factors that affect the mechanical and biological properties of scaffolds and influence bone ingrowth and transportation of cells and nutrients. However, it is complicated evaluating the effects of these factors on porous scaffolds, since they are in conflict to each other in certain circumstances. Therefore, finding the optimal topologies for scaffolds is a major goal in the biomedical field.

## 2.2. TAOR CELL

Biomimetic theory was applied in the design of the novel unit cell. Following the generic bio-inspiration approach [5], several natural structures have been taken into account and analysed; finally, the attention was focused on the structure of rocks, in particular on the evolution of polygonal fracture patterns in volcanic rocks.

Many volcanic rocks, especially basaltic lava flows, due to cooling-induced fractures, also known as columnar joints, are divided into slender prismatic columns with polygonal cross sections. The columnar joints form polygonal patterns that vary from being tetragonal to nearly hexagonal [100].

Joint intersection analysis allows to determine the processes that are responsible for the observed patterns. The most common types of joint intersections are T, curved T and Y. The first two intersection types are common at the surfaces where early joints form sequentially [101] The polygons so formed are typically tetragonal; in contrast, joint patterns in a flow interior mostly consist of hexagonal polygons and Y-type intersections with angles of about 120°. This suggests that columnar joint patterns evolve from mostly tetragonal ones to mostly hexagonal ones as the joints grow inward from the flow surfaces [102]. Progressively, erosion phenomena, revealed the polygonal patterns of the interior surface of lava flows. Further analyses, conducted in several volcanic sites, showed that the polygonal patterns evolve from tetragonal, not only in hexagonal shape but also in

pentagon, heptagon and octagon [103]. The formation of polygonal joint networks is favoured because they minimize the surface energy and the strain energy of the system [100]; indeed, concepts in fracture mechanics assess that fracture initiation occurs when the strain-energy density reaches a critical value [104].

Starting from the concept above mentioned, an analysis of regular polygons has been conducted. Only polygons with an even number of edges have been analysed, in order to have two parallel edges on which apply boundary conditions; thus, static FE analysis on holed prisms with cross-sectional area of: square, hexagon, octagon, decagon and dodecagon have been carried out.

Two sets of analyses were conducted on prisms with the same strut thickness or with the same volume. By referring to Fig. 19, in the first set of analyses, the selected polygon size  $L$  was 10 mm while strut thickness and width were both 1 mm. In the analyses of the polygons with the same volume, the square prism dimensions had kept unchanged; while, keeping unvaried the size  $L$  and the strut thickness  $t$ , the width  $w$  of the other prisms was selected in order to obtain the same volume of the square prism, as reported in Table 1.

**Table 1** Width dimension of the prisms in the second set of analysis

	<b>Hexagon</b>	<b>Octagon</b>	<b>Decagon</b>	<b>Dodecagon</b>
<b>w [mm]</b>	1.18	1.24	1.27	1.28

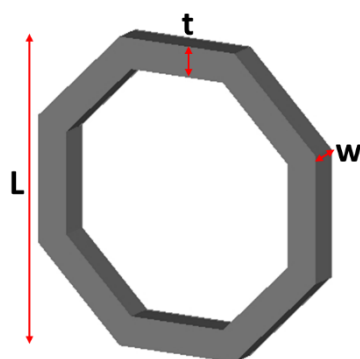


**Fig. 19** Regular polygon dimensions

All the prisms were meshed using first order hexahedral elements of 0.3 mm dimension, in order to have a minimum of three elements on the strut thickness. The selected material for the analysis is the titanium alloy Ti6Al4V ELI, the main mechanical properties are reported in Table 2.

**Table 2** Ti6Al4V ELI alloy mechanical properties [105]

	E [GPa]	$\nu$	$\rho$ [kg/m <sup>3</sup> ]
<b>Ti6Al4V ELI</b>	115	0.34	4430

Boundary conditions were applied as reported in Fig. 20 for the first set of analysis.

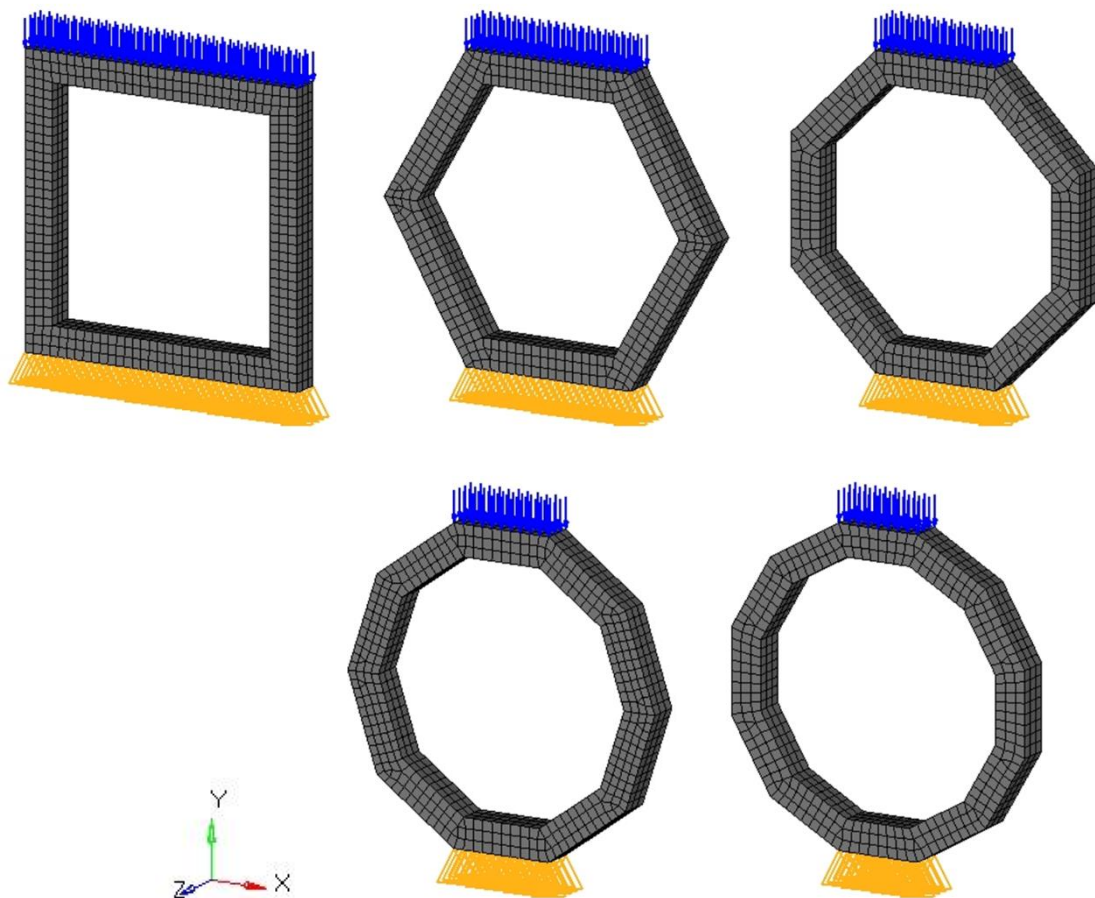


**Fig. 20** Boundary conditions of the first set of analyses on polygonal prisms

Blue arrows represent a compressive load of 10 N, orange triangles represent a fixed constraint. The same boundary conditions have been applied to the second set of analysis. The results of both set of analysis are reported in Fig. 21.

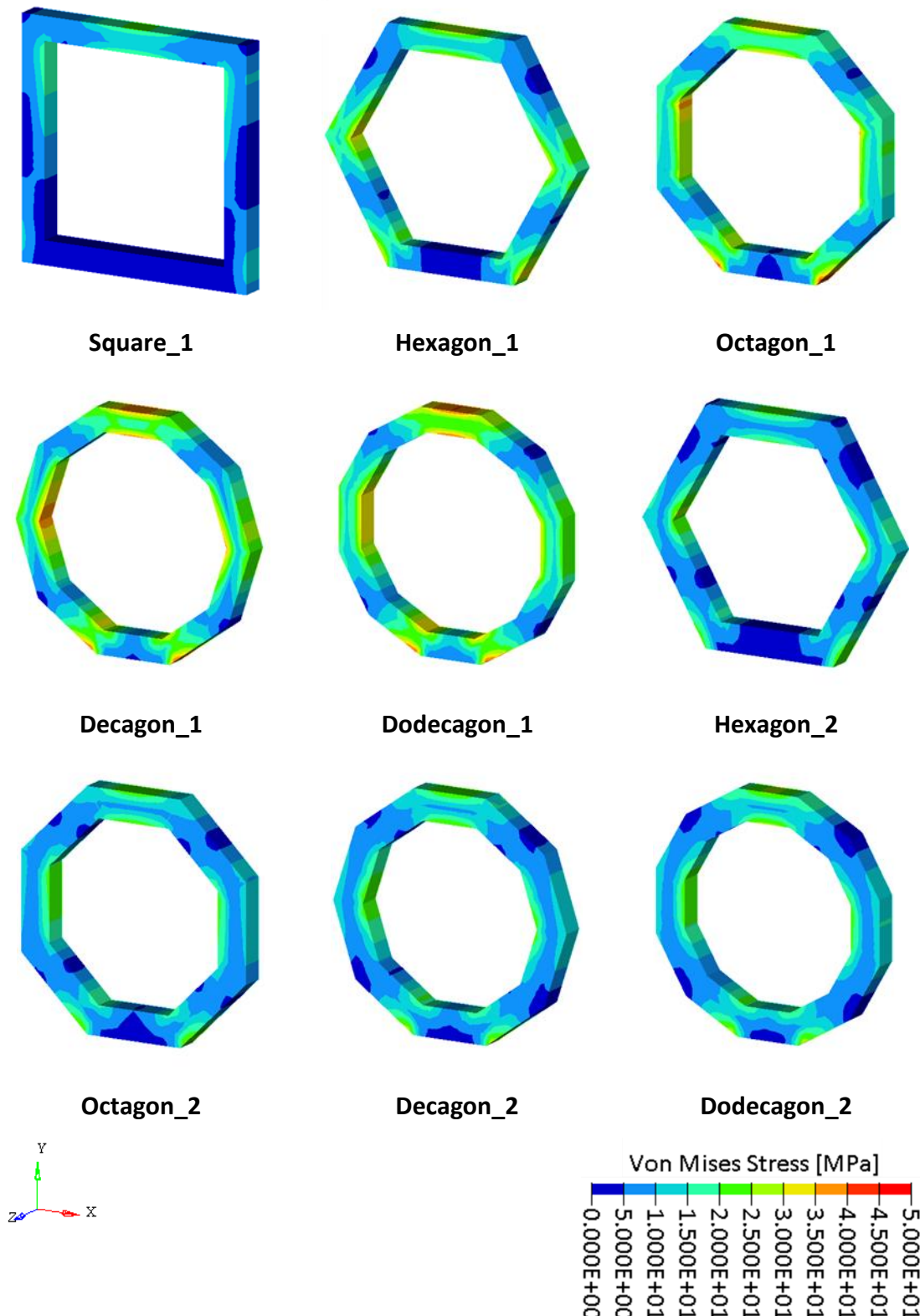


**Fig. 21** Polygonal prisms FE analysis results

The name “Polygon\_1”, refers to the prisms of the first set of analysis, while “Polygon\_2” to the prisms of the second one.

From the analysis of the first set, it can be seen that the square presents the lowest stress values. Both hexagon and decagon present a stress increase in the central node, more accentuated in the decagon. The comparison of the polygons with vertical central strut shows that: octagon presents a stress increase at the top vertex, while the rest of the strut and the bottom vertex show low stress values. It is reasonable foreseeing a buckling failure mode for a structure in which is present an octagon subjected to compressive load. On the other hand, the dodecagon which presents a shorter strut compared to the octagon, does not show stress peaks at the vertices, but a uniform distribution with an average stress value higher than the one presented by the octagon.

As reported in section 2.1.2, lattice structures are compared to each other with the same relative density, that is with the same volume. The analysis of the second set of polygonal prisms, all with the same volume, shows that the stress values are similar in all the shapes tested. Concerning the stress distribution, the same considerations reported for the analysis of the first set can be done; however, thanks to the thicker struts, all the polygons considered present lower peak stress values at the node, with a smoother stress distribution around the vertices.

In the choice of the most suitable polygonal shape, alongside the FE analysis results, the complexity of the structure has been taken into account. As seen in section 1.2.2., lattice structures with a high number of faces, edges and vertices are hardly achievable, especially when small cell size values, in the order of micrometres or few millimetres, are considered. In these cases, the real shape of the lattice not always match well the designed one. In the design of the novel unit cell, it was not considered an exact parameter that evaluate the complexity, since many factors influence the achievable shape, such as: AM technology, manufacturing machine, material, cell size, relative density. It was therefore decided, to maintain the level of complexity of the structure in the order of the one of the strut-based unit cells most commonly used in the production of lattice structures, described in section 2.1.1.

Due to all the above considerations, the octagon was selected as the optimal shape for the design of the novel unit cell.

The idea was to combine with each other octagons of the same dimensions forming a ring. To this purpose, an octagon was considered as the edge of the polygon that defines the

perimeter of the ring generated by the combination of multiple octagons, as shown in Fig. 22.

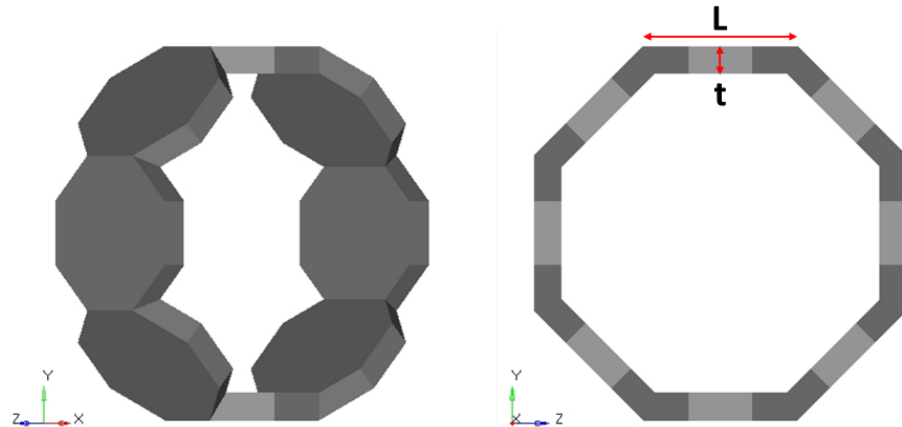


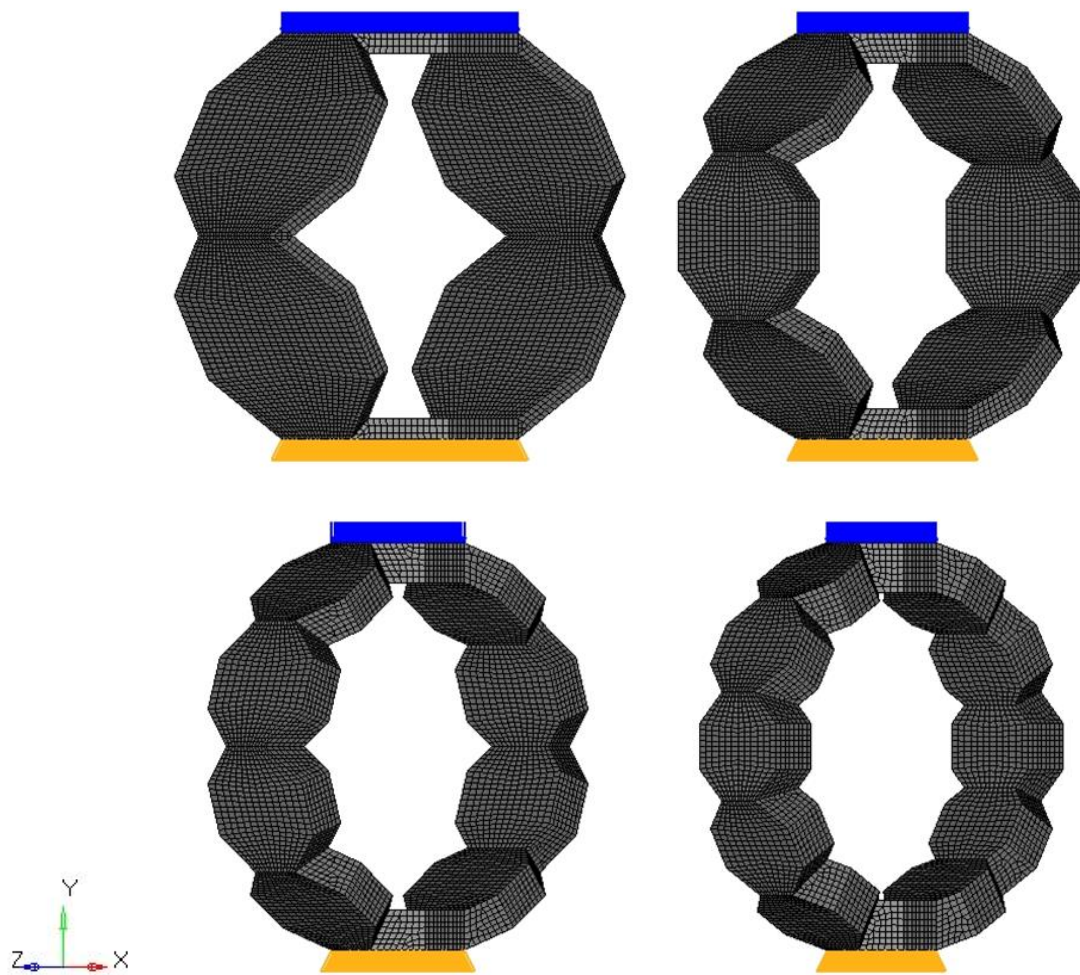
**Fig. 22** Ring generated by the combination of multiple octagons

A static FE analysis was carried out to choose the number of octagons; thus, rings with six, eight, ten and twelve octagons were analysed. As previously done in the analysis of the regular polygons, also in this case, only rings with an even number of edges have been analysed, in order to have two parallel edges on which apply boundary conditions. All the polygons forming the perimeter of the rings have an apothem of 10 mm, thus the edges length  $L$  have been accordingly sized; while, thickness  $t$  values were selected in order to obtain rings with the same volume, as reported in Table 3.

**Table 3** Dimensions of the polygons forming the perimeter of the rings

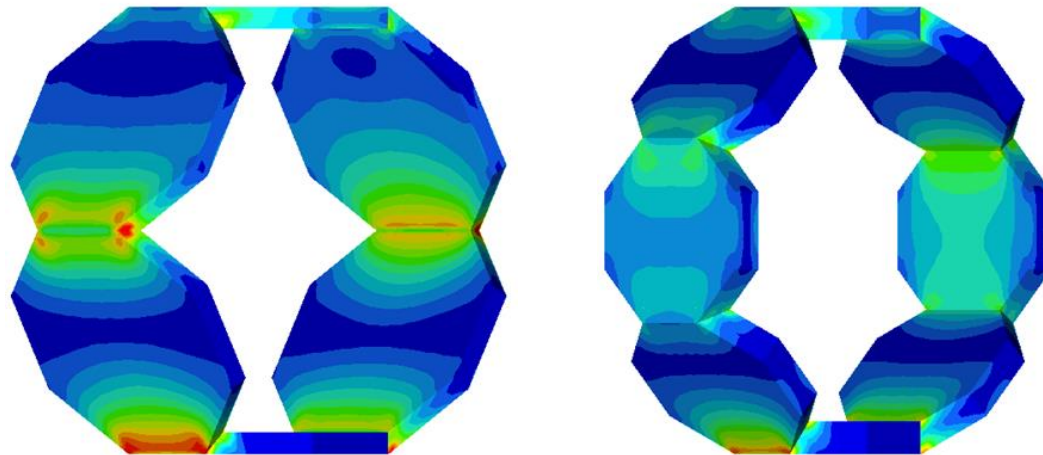
	<b>Hexagonal</b>	<b>Octagonal</b>	<b>Decagonal</b>	<b>Dodecagonal</b>
<b>L [mm]</b>	11.55	8.28	6.5	5.36
<b>t [mm]</b>	1	1.48	1.95	2.44

Mesh parameters and material properties are the same reported in the analysis of regular polygons, while boundary conditions are shown in Fig. 23.



**Fig. 23** Boundary conditions of the analysis on polygonal rings

Blue arrows represent a compressive load of 100 N, orange triangles represent a fixed constraint. The results of the analysis are reported in Fig. 24.



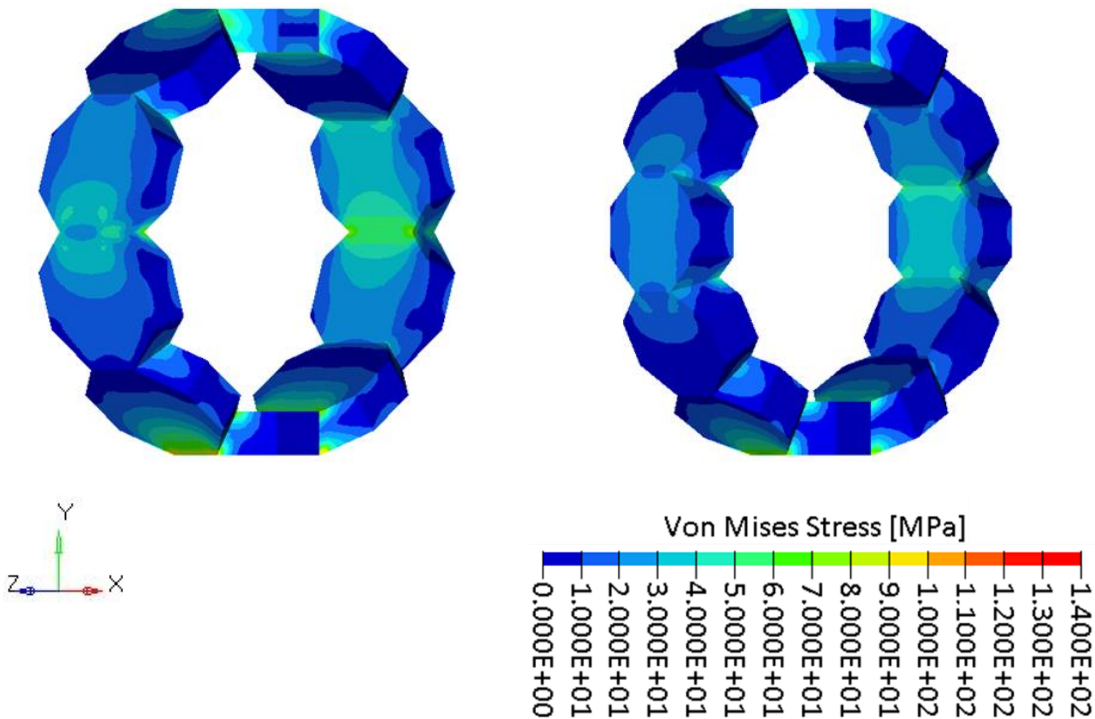


**Fig. 24** Polygonal rings FE analysis results

Stress distribution at the contact between two octagons, forming the edges of the polygon, have been analysed. All the polygonal rings present comparable stress distribution with peak stresses on the nodes of the polygon between two adjacent octagons. Stress values decrease while increasing the number of edges forming the ring; in particular, hexagonal ring was discarded because it presents higher stresses compared to the other shapes. Octagonal and decagonal rings present comparable stress values, while they decrease in the dodecagonal ring. Decagonal ring was therefore discarded, because with equal stress values, the octagonal ring was chosen due to the less complexity. Between octagonal and dodecagonal ring, the first one was chosen, because the advantage of the dodecagonal ring of presenting lower stress values was not considered sufficient to justify the higher complexity of the structure.

To obtain an isotropic lattice structure, cubic symmetry was imposed. Therefore, each unit cell is made of three rings mutually perpendicular, one ring for each principal direction, as shown in Fig. 25. Combining more than three rings would have led to intersection or bad connection of the struts.

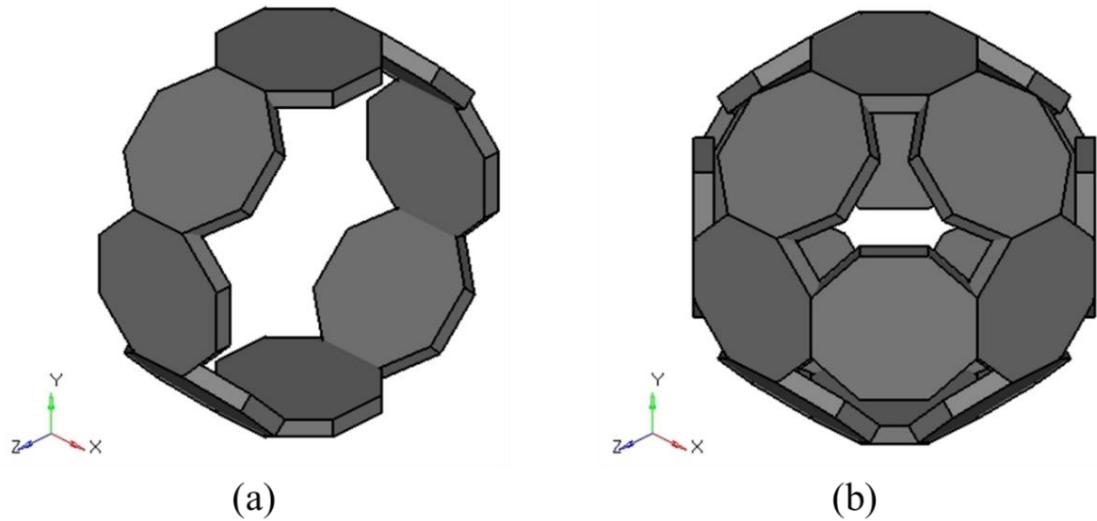


**Fig. 25** (a) ring of the new unit cell; (b) complete structure of the new unit cell

In Fig. 26 is shown the new designed cell, namely Triply Periodic Arranged (TAOR) cell.

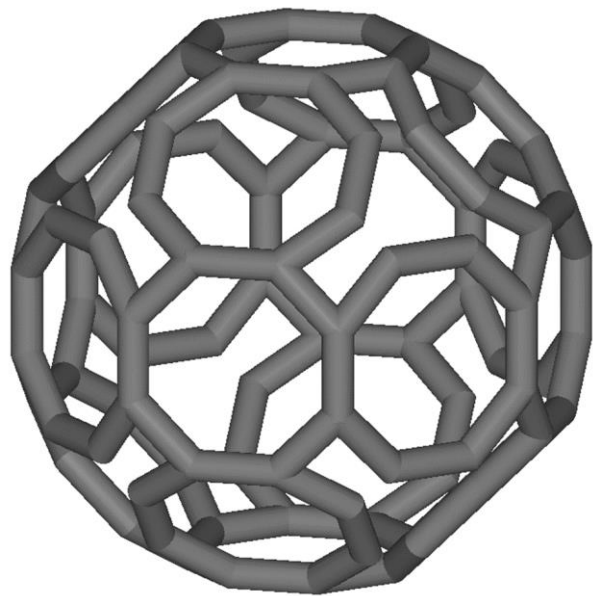


**Fig. 26** TAOR cell

Three design variables determine the properties of a lattice structure, these factors are [14]:

- the relative density, defined by the cell edge length and the strut thickness

- the topology and shape of the cell edges and faces; evaluated by means of the Maxwell criterion, which predict the deformation behaviour of the lattice material as bending dominated or stretch dominated
- the material of which the structure is made, which influence the mechanical, thermal and electrical properties of the lattice material

The relative density was defined in their study by Gibson-Ashby as: the density of the cellular material, divided by that of the solid from which the cell struts/walls are made [6].

Nowadays, in literature two methods are applied to calculate the relative density. Zadpoor *et al.* defined the method to evaluate the relative density: The volume occupied by a single-unit cell is first calculated; only a part of that entire volume is occupied by the struts constituting the unit cell, which is then calculated by summing up the volume of all struts of the unit cell. The total volume of the struts is then divided by the total volume of the unit cell to calculate the relative density of the porous structure [74]. It is important consider that the beams are not one dimensional lines and occupy space in reality. At the intersection of struts, the volumes of different intersecting struts overlap, meaning that intersecting struts share part of their volume; thus, multiple counting of these shared volume overestimates the relative density. This issue was not considered until Hedayati *et al.* showed that multiple counting could result in significant deviation of analytical solutions from numerical results and experimental observations; those deviations were minimized when multiple counting was corrected [106]. With the first method, the relative density is thus calculated as the ratio between the volume occupied by the strut  $V_{\text{strut}}$  and the volume of the geometry  $V_{\text{geom}}$  as shown in Fig. 27.

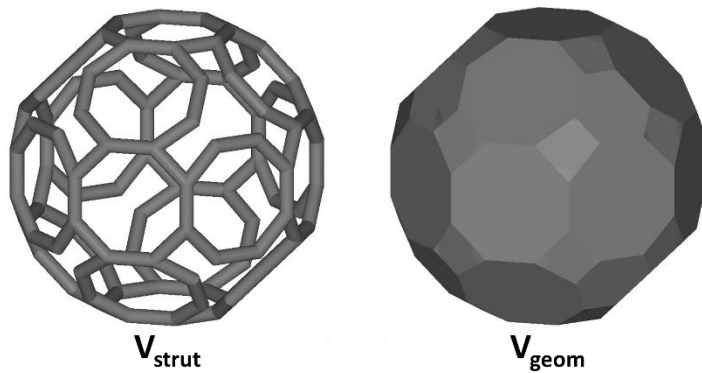


**Fig. 27** Volume considered in the first method for the evaluation of the relative density

In other research [52], the relative density was calculated as the ratio between the volume occupied by the strut  $V_{\text{strut}}$  and the volume of a cube  $V_{\text{cube}}$  with the edge of the same length of the unit cell size. This method is also applied in software for the generation a lattice structure, for instance: ASLI [107] and MS Lattice [108]. In Fig. 28 are reported the volumes considered for the calculation of the relative density with the second method.

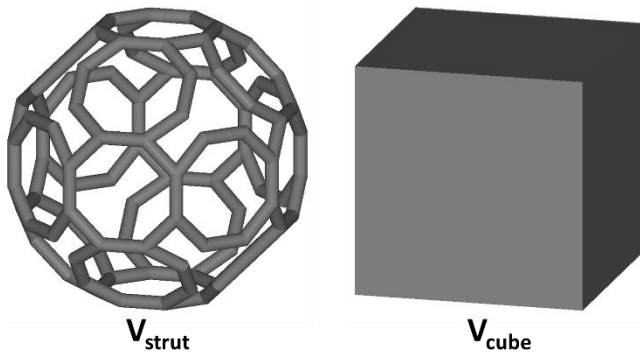


**Fig. 28** Volume considered in the second method for the evaluation of the relative density

Both methods have been applied for the calculation of the relative density of the TAOR cell. To avoid the issue of the multiple counting of the shared volume at the intersection of the strut, the volume occupied by the strut was calculated in CAD environment, where only the actual volume is considered without overlapping [109].

In CAD software, the volume of TAOR geometry  $V_{\text{geom}}$  for cell sizes from 1 mm up to 60 mm, with steps of 1mm, was calculated; then using MATLAB R2021a (MathWorks, MA) software, a curve fitting of the data, evaluated the volume formula of the TAOR as a function of the edge length, with a coefficient of determination  $R^2 = 1$ .

$$V_{\text{geom}} = 120.91 * L^3 \quad (13)$$

The same method was applied to evaluate  $V_{\text{strut}}$ . For the cell sizes above mentioned, strut diameter in a range between 0.2 mm and 3 mm, with steps of 0.2 mm, were considered. Moreover, un upper limit of 0.5 for the calculated relative density was imposed. As seen in section 1.2.1., most of the lattice structures only cover relative densities values from 0.1 up to 0.5. Thus, the relative density, in terms of volume fraction, was evaluated by using MATLAB with both methods as a function of  $d/D$  and  $d/L$ . Where  $d$  is the strut diameter,  $D$  the cell size and  $L$  the edge length.

$$\frac{V_{strut}}{V_{geom}} = -63.1 \left(\frac{d}{D}\right)^3 + 28.1 \left(\frac{d}{D}\right)^2 - 4.8 \cdot 10^{-2} \left(\frac{d}{D}\right) \quad (14)$$

$$\frac{V_{strut}}{V_{cube}} = -38.5 \left(\frac{d}{D}\right)^3 + 17.2 \left(\frac{d}{D}\right)^2 - 2.9 \cdot 10^{-2} \left(\frac{d}{D}\right) \quad (15)$$

$$\frac{V_{strut}}{V_{geom}} = -3.1 \cdot 10^{-1} \left(\frac{d}{L}\right)^3 + 6.9 \cdot 10^{-1} \left(\frac{d}{L}\right)^2 + 9.5 \cdot 10^{-3} \left(\frac{d}{L}\right) \quad (16)$$

$$\frac{V_{strut}}{V_{cube}} = -1.9 \cdot 10^{-1} \left(\frac{d}{L}\right)^3 + 5.1 \cdot 10^{-1} \left(\frac{d}{L}\right)^2 - 5 \cdot 10^{-3} \left(\frac{d}{L}\right) \quad (17)$$

For all the equations evaluated, the coefficient of determination is  $R^2 = 1$ . In Fig. 29 is reported a comparison of the relative densities evaluated with the two methods

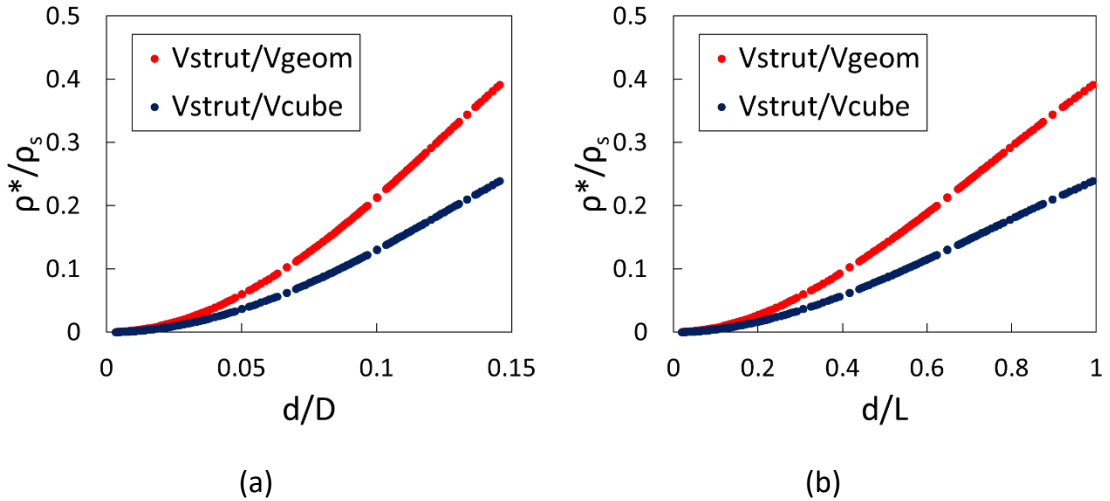


**Fig. 29** Comparison of the relative densities evaluated with the two methods, as a function of: (a)  $d/D$ ; (b)  $d/L$

Concerning the evaluation of cell topology and shape, the Maxwell criterion was applied to predict the compressive behaviour of the lattice structure. By applying the equation 8 reported in section 2.1.2., the TAOR cell consists of 120 struts E and 48 vertices V. The calculated Maxwell number M is -18, thus the predicted compressive behaviour of the TAOR cell is bending dominated.

## **Chapter 3**

# **MECHANICAL ANALYSIS OF LATTICE STRUCTURES**

### **3.1. EXPERIMENTAL ANALYSIS**

The aim of the experimental analysis was the mechanical and morphological characterization of the new proposed TAOR cell for applications in biomechanical devices used as bone substitutes. A comparison between TAOR cell and other lattice structures with similar geometric features that are currently used in the biomechanical field was performed, the selected unit cells were the truncated octahedron cell (Kelvin cell) and the rhombic dodecahedron (RD) cell. The RD lattice was previously tested in the laboratory of the Department of Engineering at the University of Messina [105]. In this section, since the methodology and the experiments applied were the same, the results of another work conducted during the PhD on Body Centered Cubic (BCC) derived structures were also presented [110]. These structures are the strut-based G7 cell and the TPMS sheet-based IWP cell.

#### **3.1.1. Specimens production**

Compression tests were performed to investigate the mechanical properties of TAOR, Kelvin and G7 cells. The lattice structures were produced via EBM technology, by an Arcam Q10 printer, using Ti6Al4V ELI (Grade 23) fine powder. The used titanium alloy contains reduced levels of oxygen, nitrogen, carbon and iron and its particle size distribution is between 45 and 100  $\mu\text{m}$ . The powder layer thickness was set to 50  $\mu\text{m}$ . A preheating was applied to the building plate up to a temperature of 730 °C. During the printing, a controlled vacuum of  $10^{-3}$  mbar was maintained in the chamber.

Three different levels of relative density were analysed: 5%, 10% and 20%. The three configurations were obtained by varying the size D of the cell while maintaining constant the diameter d of the strut at 0.2 mm (Fig. 30).

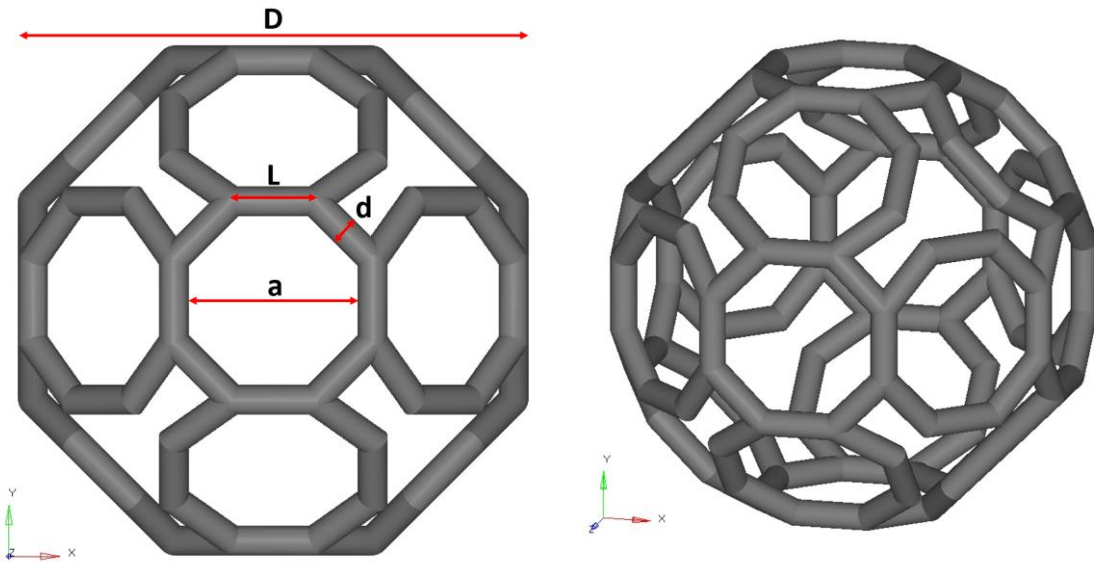


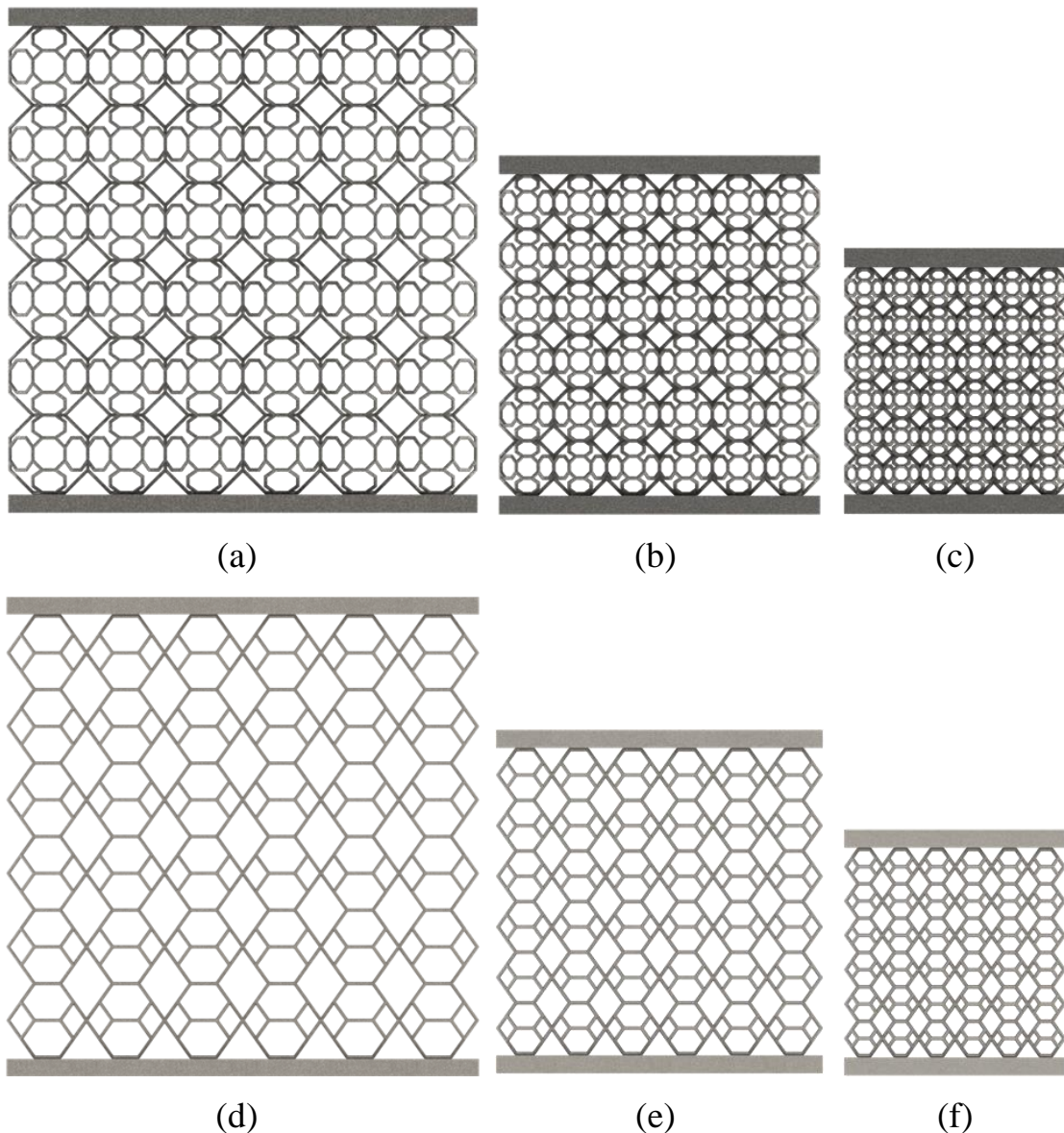
**Fig. 30** Geometric parameters of the TAOR cell

By applying the equation 14 seen in section 2.2., the dimensions of the TAOR cell were evaluated. The same approach described in section 2.2. was applied to evaluate  $V_{\text{strut}}$ ,  $V_{\text{geom}}$  and thus the dimensions of Kelvin and G7 cells. Moreover, the dimensions of the Kelvin cell were verified from equation of the relative density present in literature [74]. Thus, the geometric parameters of the single unit cells adopted to produce the lattice structures are shown in Table 4.

**Table 4** As designed geometric parameters of the TAOR, Kelvin and G7 unit cells

$\rho^*/\rho_s [\%]$	TAOR cell			Kelvin cell			G7 cell		
	5	10	20	5	10	20	5	10	20
D [mm]	4.4	3	2.1	4.4	3	2.1	2.9	2.1	1.4
d [mm]	0.2	0.2	0.2	0.2	0.2	0.2	0.2	0.2	0.2
L [mm]	0.72	0.48	0.33	1.55	1.06	0.74	2.28	1.59	0.98
a [mm]	1.61	1.03	0.66	2.48	1.63	1.08	1.70	1.14	0.65
d/D	0.045	0.067	0.095	0.045	0.067	0.095	0.07	0.10	0.14
d/L	0.28	0.42	0.61	0.13	0.19	0.27	0.088	0.133	0.204

All the configurations analysed guaranteed six-unit cells for each edge of the lattice structure in order to avoid edge effect; thus, each specimen is made of 6x6x6 unit cells as shown in Fig. 31. A superior and an inferior plate with 1 mm thickness are considered for the application of the loads during experimental tests. It was experimentally verified that the presence of face-sheets does not influence failure mechanisms and compressive response of the lattice specimens [71], [105], [111], [112]. Geometrical characteristics of the specimens are summarised in Table 5. Where 5%, 10% and 20% represent the relative densities of the lattice structures.



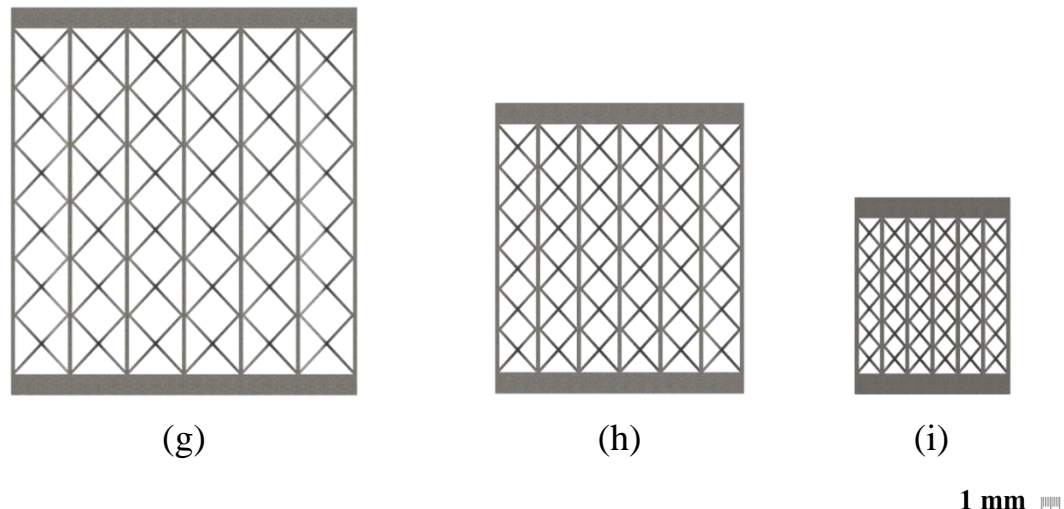


**Fig. 31** Specimens: (a) TAOR\_5%; (b) TAOR\_10%; (c) TAOR\_20%; (d) Kelvin\_5%;  
 (e) Kelvin\_10%; (f) Kelvin\_20%; (g) G7\_5%; (h) G7\_10%; (i) G7\_20%

**Table 5** As designed geometric parameters of the TAOR, Kelvin and G7 specimens

	TAOR	TAOR	TAOR	Kelvin	Kelvin	Kelvin	G7	G7	G7
	5%	10%	20%	5%	10%	20%	5%	10%	20%
Height [mm]	27.4	19	13.6	25.9	18	12.9	18.4	13.2	9.4
Length [mm]	25.4	17	11.6	25.4	17	11.6	16.4	11.2	7.4
Width [mm]	25.4	17	11.6	25.4	17	11.6	16.4	11.2	7.4

### 3.1.2. Morphological analysis

The morphological analysis was focused on the comparison between as produced and as designed structures, to evaluate the matching of their geometric parameters. All the analysis were performed before carrying out the compressive tests. A comparison between designed and actual specimens dimensions is reported in Table 6.

**Table 6** Specimens dimensions comparison between designed and actual values

	TAOR 5%	TAOR 10%	TAOR 20%	Kelvin 5%	Kelvin 10%	Kelvin 20%	G7 5%	G7 10%	G7 20%
mass <sub>d</sub> [g]	7.75	3.87	2.04	7.07	3.45	1.78	3.26	1.76	0.82
mass <sub>a</sub> [g]	10.99	4.43	4.03	9.14	4.02	3.11	7.40	3.68	1.65
mass <sub>v</sub> [%]	41.8	14.47	97.55	29.28	16.52	74.72	126.99	109.09	101.22
height <sub>d</sub> [mm]	27.4	19	13.6	25.9	18	12.9	18.4	13.6	9.4
height <sub>a</sub> [mm]	28.11	18.73	14.28	25.31	18.34	13.88	19.43	14.41	10.42
height <sub>v</sub> [%]	2.59	-1.42	5.00	-2.28	1.89	7.59	5.59	5.96	10.85
width <sub>d</sub> [mm]	25.4	17	11.6	25.4	17	11.6	16.4	11.6	7.4
width <sub>a</sub> [mm]	25.24	17.29	12.25	25.77	17.38	11.88	17.59	12.42	8.41
width <sub>v</sub> [%]	-0.63	1.71	5.60	1.46	2.24	2.41	7.26	7.07	13.65
length <sub>d</sub> [mm]	25.4	17	11.6	25.4	17	11.6	16.4	11.6	7.4
length <sub>a</sub> [mm]	25.72	16.89	12.24	25.83	16.59	11.93	17.57	12.40	8.41
length <sub>v</sub> [%]	1.26	-0.65	5.52	1.69	-2.41	2.84	7.13	6.89	13.65

Where the subscripts stand for: d, designed; a, actual; v, variation.

Actual mass and overall dimensions values are higher than the designed ones. For all the lattice structures, specimens with relative density 20% present higher overall dimensions variations.

The microstructure of the specimens was observed by means of a scanning electron microscope (SEM), as shown in Fig. 32.

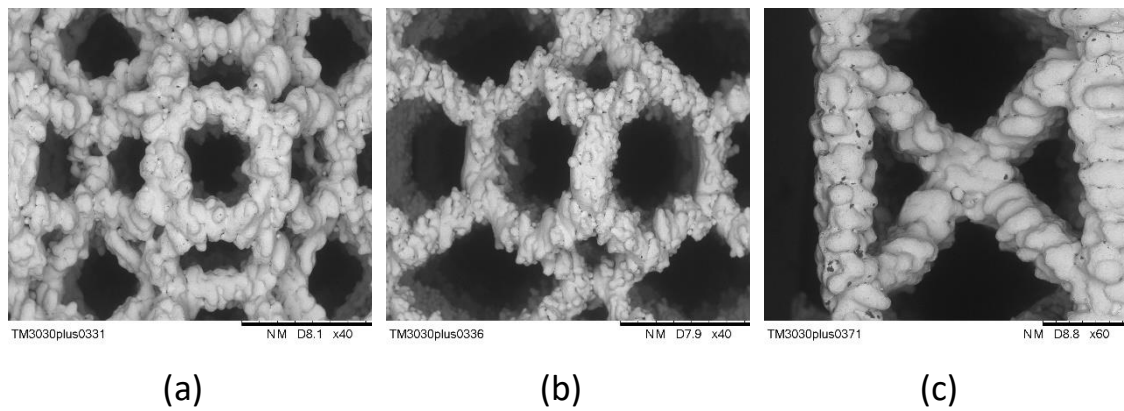


**Fig. 32** SEM images of lattices with 10% relative density: (a) TAOR; (b) Kelvin; (c) G7

The matching between actual and designed values of cell size, strut diameter and pore size was evaluated. The results of the comparison are summarised in Table 7.

**Table 7** Cells dimensions comparison between designed and actual values

	TAOR 5%	TAOR 10%	TAOR 20%	Kelvin 5%	Kelvin 10%	Kelvin 20%	G7 5%	G7 10%	G7 20%
D <sub>d</sub> [mm]	4.4	3	2.1	4.4	3	2.1	2.9	2.1	1.4
D <sub>a</sub> [mm]	4.21	2.78	1.90	4.50	2.92	1.96	2.89	2.06	1.42
D <sub>v</sub> [%]	-4.5	-6.7	-9.5	2.3	-3.3	-4.8	-0.4	-1.9	1.4
d <sub>d</sub> [mm]	0.2	0.2	0.2	0.2	0.2	0.2	0.2	0.2	0.2
d <sub>a</sub> [mm]	0.37	0.47	0.50	0.42	0.42	0.38	0.50	0.40	0.39
d <sub>v</sub> [%]	85	135	150	110	110	90	150	100	95
a <sub>d</sub> [mm]	1.61	1.03	0.66	2.48	1.63	1.08	1.70	1.14	0.65
a <sub>a</sub> [mm]	1.24	0.78	0.45	1.8	1.2	0.75	1.17	0.83	0.48
a <sub>v</sub> [%]	-23.0	-24.3	-31.8	-27.4	-26.4	-30.6	-31.18	-27.19	-26.15

Designed cell size and pore size values are higher than actual ones in all the configurations except for the cell size of Kelvin\_5%. Regarding the cell size, for TAOR and Kelvin structures, discrepancies between actual and designed values increase while increasing the relative density; higher percentage variations have been observed in the TAOR cell compared to the other structures for each relative density. However, the cell size increase detected in the actual TAOR lattice is constant, around 0.2 mm, for all the configurations. The cell size increase of the actual Kelvin lattice is around 0.1 mm, while in the G7 lattice is 0.02 mm. For the G7 lattice, negligible percentage variations, lower than 2%, were detected for all the relative densities.

Pore size percentage variation of TAOR lattice increase while increasing the relative density, while it decreases in the G7 lattice. For the Kelvin structure, the pore size variation decreases from 5% to 10% relative densities, while highest value is observed for relative density 20%. The discrepancies between designed and actual pore sizes can be explained by considering the strut diameter values. Indeed, for all the configurations, higher discrepancies are detected; it can be observed that actual strut diameters are double of the designed ones.

High discrepancies in the strut diameter values also influence the actual mass of the specimens. In Table 6 can be observed that, despite specimens actual overall dimensions are higher than designed ones, low differences are detected; while higher percentage variation are observed in mass values. This can also be explained considering that evaluating the relative density of the unit cell with equation 14 of section 2.2 leads to an overestimation of the specimen relative density. Indeed, for a cubic specimen with 6x6x6 unit cells, considering the volume occupied by the strut in the cube and the volume of the cube, the designed relative density of the specimen will be lower than the designed relative density of the unit cell. In Table 8 is summarised the comparison of the relative densities for the TAOR and the Kelvin structures.

**Table 8** Designed relative density comparison between single unit cells and specimens

	TAOR 5%	TAOR 10%	TAOR 20%	Kelvin 5%	Kelvin 10%	Kelvin 20%
$\rho^*/\rho_s$ cell [%]	5	10	20	5	10	20
$\rho^*/\rho_s$ specimen [%]	3	6	13	2	4	9
$\rho^*/\rho_s$ variation [%]	-60	-60	-65	-40	-40	-45

TAOR structure presents higher percentage differences compared to the Kelvin structure. For both lattice materials, the specimens with relative density 20% present higher percentage differences than the other relative densities. In general, an increase of the unit cells number in the specimen, lead to an increase of the variation of the relative density. For the G7 lattice, the volume of the geometry considered for the evaluation of the relative density is the cube, thus no differences in the expected relative density of the specimens were detected, compared to the ones of the single unit cells.

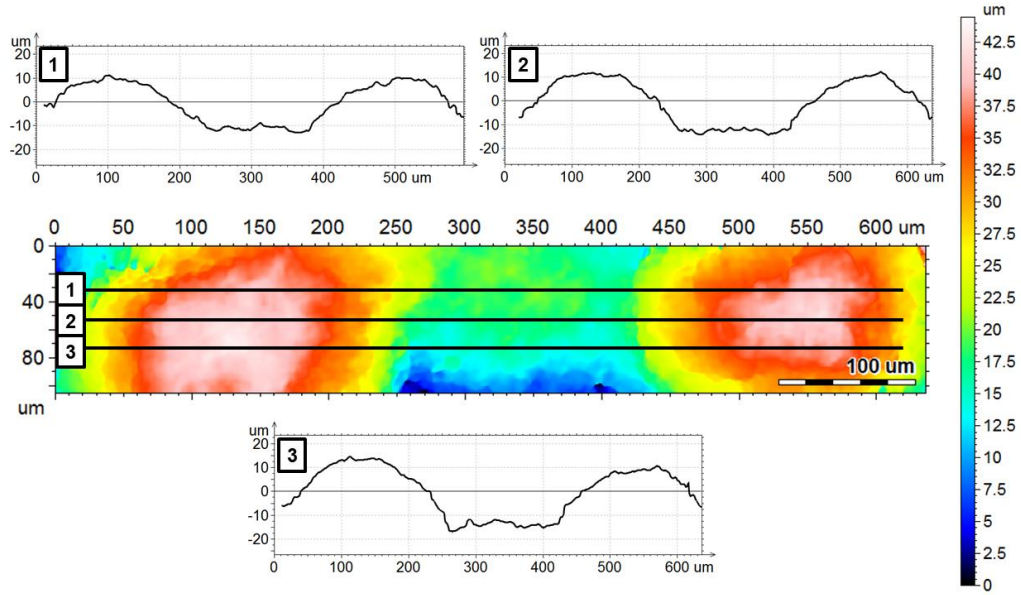
Considering the actual specimens dimensions (Table 6), the actual relative density was evaluated, as shown in Table 9.

**Table 9** Actual specimen relative density

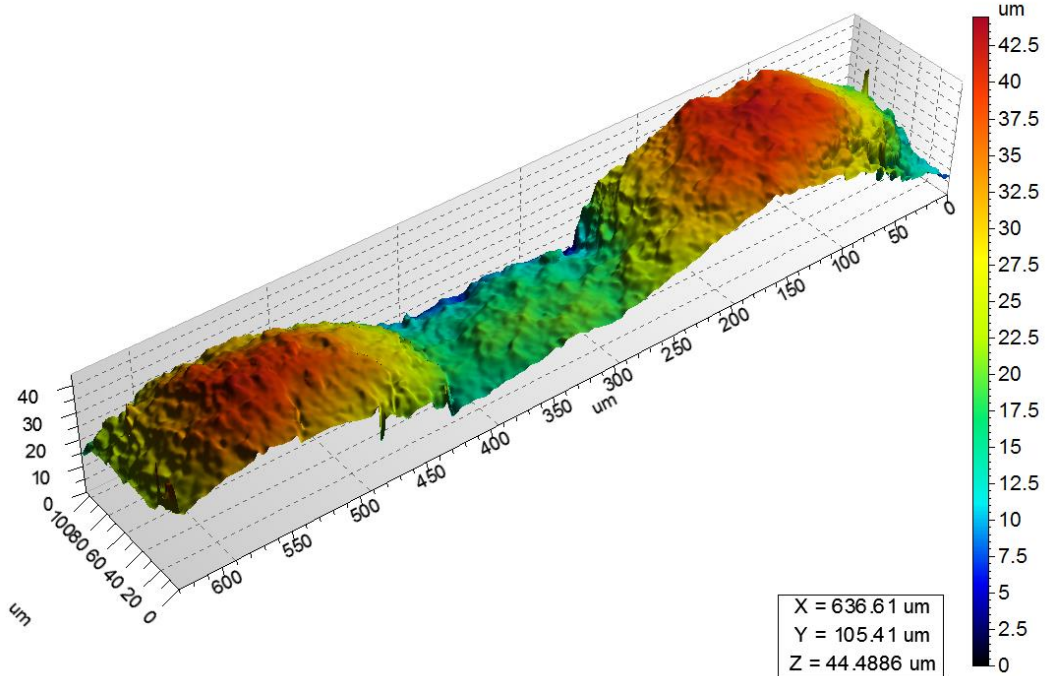
	TAOR 5%	TAOR 10%	TAOR 20%	Kelvin 5%	Kelvin 10%	Kelvin 20%	G7 5%	G7 10%	G7 20%
$\rho^*/\rho_s$ actual [%]	7	9	41	5	7	30	20	27	38

Surface analyses were carried out to measure roughness, which is an important requirement to fulfilled in the design of bone substitutes. The range of 0.5–8.5  $\mu\text{m}$  is suggested for bone scaffolds [59], [113]. The average roughness ( $S_a$ ) of the strut was measured on the whole surface and was 8.35  $\mu\text{m}$ . The results in Fig. 33 highlights a certain waviness of the surface, that is due to the EBM process (layer-by-layer building of the struts). It worth mentioning that to remove the un-melted titanium particles, the specimens

were subjected to sandblasting after their production. Moreover, to prevent contamination of the struts with undesirable materials (i.e. Silicon), the sandblasting was performed with the same powder used to build the specimens. After this process, the powder is recovered and reused.



(a)



(b)

**Fig. 33** Topography of the strut surface: (a) roughness profiles; (b) 3D reconstruction of the surface.

### 3.1.3. Compressive tests

Compressive tests of the TAOR and the Kelvin specimens were performed on a Zwick-Roell Z250 testing machine equipped with a 250 kN load cell, while an INSTRON 8854 servo-hydraulic testing machine, equipped with a 250 kN load cell, was used to perform the tests of the G7 specimens. In all the cases, the tests were carried out at a constant crosshead speed of 1 mm/min and a preload of 5 N was applied during the tests. Due to the repeatability of the tests, two repetitions were carried out for each specimen configuration.

Compression tests results are reported in Fig. 34 in terms of stress-strain curves. Stress was obtained as the ratio between the axial load and the cross section of lattice specimens, whereas strain was evaluated from the crosshead displacement divided by the initial height of the specimen.

The curves show the typical trend of lattice materials presented in section 2.1.2., the results are consistent with previous published papers [3].

The first stage represents the initial linear elastic region, followed by a slight slope variation up to a maximum stress value, which was evaluated as the compressive strength  $\sigma_m$  of the lattice structure. The second stage represents the plateau region: the structure continues to collapse, and a sudden load fall appears, followed by a region with a nearly constant mean stress (the plateau stress  $\sigma_{pl}$ ). In this zone, the curve trend differs from the ideal one showed in section 2.1.2., due to the failure of some unit cells within the lattice, that cause significant stress fluctuations. In the third stage, the lattice densification caused by the contact of completely collapsed cells leads to a stress increase.

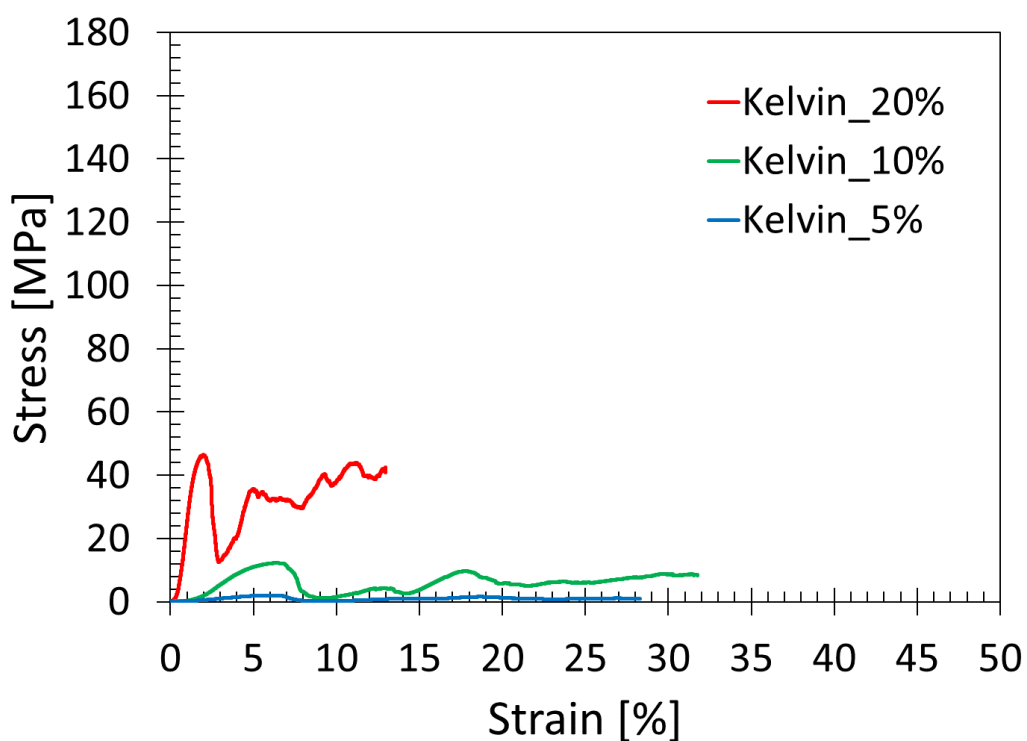
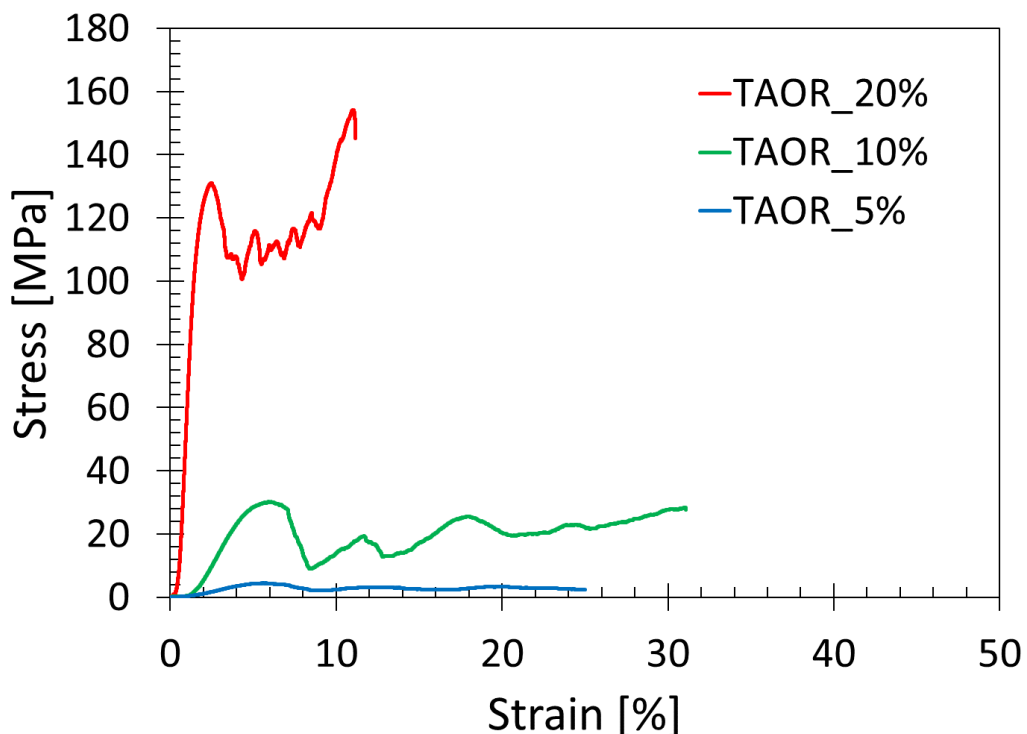
In Table 10 are reported the parameters obtained from compression tests: Young's Modulus E, compressive strength  $\sigma_m$ , plateau stress  $\sigma_{pl}$ , Total Energy absorbed (TEA), Specific Energy Absorption (SEA) and peak force  $F_{MAX}$ . Plateau stress was evaluated as the mean stress value in the zone where stress fluctuations appear. TEA was evaluated as the area under the load-displacement curve obtained during compression tests; to ensure results comparability, the TEA was calculated, for all specimens, up to a strain equal to 12%. SEA was calculated as the ratio between the TEA and the actual lattice structure density.

The TAOR cell presents mechanical properties greater than the ones of the Kelvin cell for each level of relative density considered. TAOR cell has elastic modulus, TEA and peak force higher than the G7 cell ones for the relative density 20%, while they are lower for the other relative densities. Both compressive strength and plateau stress of the TAOR

are lower than the G7 values. SEA values of the TAOR are higher than the G7 ones for relative densities 10% and 20%, while it is lower for relative density 5%. From the comparison with the RD cell, the elastic modulus and the compressive strength of the TAOR are greater for the density of 10% and 20% while are lower for the density 5%. The TAOR cell presents plateau stress values higher than the RD cell ones for all the relative densities considered. The TAOR cell present SEA values higher than RD cell for the relative density 20%, while it is lower for the relative densities 5% and 10%. The mechanical properties of TAOR and Kelvin lattice structures increase while relative density increase according with data present in literature [10] and with the prediction of the Gibson-Ashby model [14]. In the G7 structure: TEA and SEA decrease while increasing the relative density; the max force reaches the maximum value in the structure with relative density 5%. In the RD structure,  $F_{MAX}$ , TEA and SEA present their maximum values in the structure with relative density 10%. However, for both structures the evaluated stresses follow the expected path.

**Table 10** Compressive tests results

	E [MPa]	$\sigma_m$ [MPa]	$\sigma_{pl}$ [MPa]	TEA [J]	SEA [Jm <sup>3</sup> /kg]	$F_{MAX}$ [kN]
<b>TAOR_5%</b>	109	4.5	2.8	5.5	0.017	2.87
<b>TAOR_10%</b>	743	30.2	22.0	10.5	0.028	8.63
<b>TAOR_20%</b>	10560	131.1	114.8	81.6	0.045	20.74
<b>Kelvin_5%</b>	46	2.0	1.0	2.0	0.009	1.43
<b>Kelvin_10%</b>	325	12.3	6.3	3.8	0.012	3.98
<b>Kelvin_20%</b>	3898	46.4	37.3	28.5	0.022	7.02
<b>G7_5%</b>	2127	58.8	21.9	22.2	0.025	18.2
<b>G7_10%</b>	3261	90.5	54.2	14.9	0.012	13.9
<b>G7_20%</b>	4192	163.7	133.5	10.7	0.006	14.6
<b>RD_5% [105]</b>	131	5.8	2.1	9.0	0.023	3.34
<b>RD_10% [105]</b>	224	11.1	4.0	16.8	0.030	6.39
<b>RD_20% [105]</b>	1104	39.9	29.4	9.7	0.010	5.66



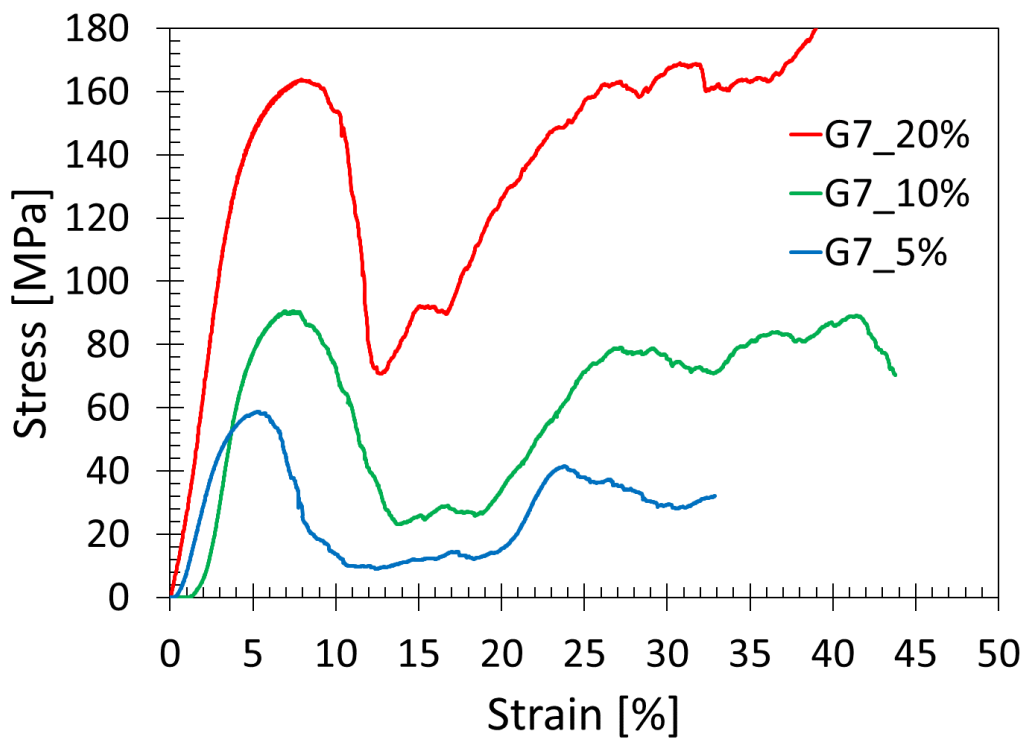


**Fig. 34** Stress-strain curves

### 3.1.4. Gibson-Ashby diagram

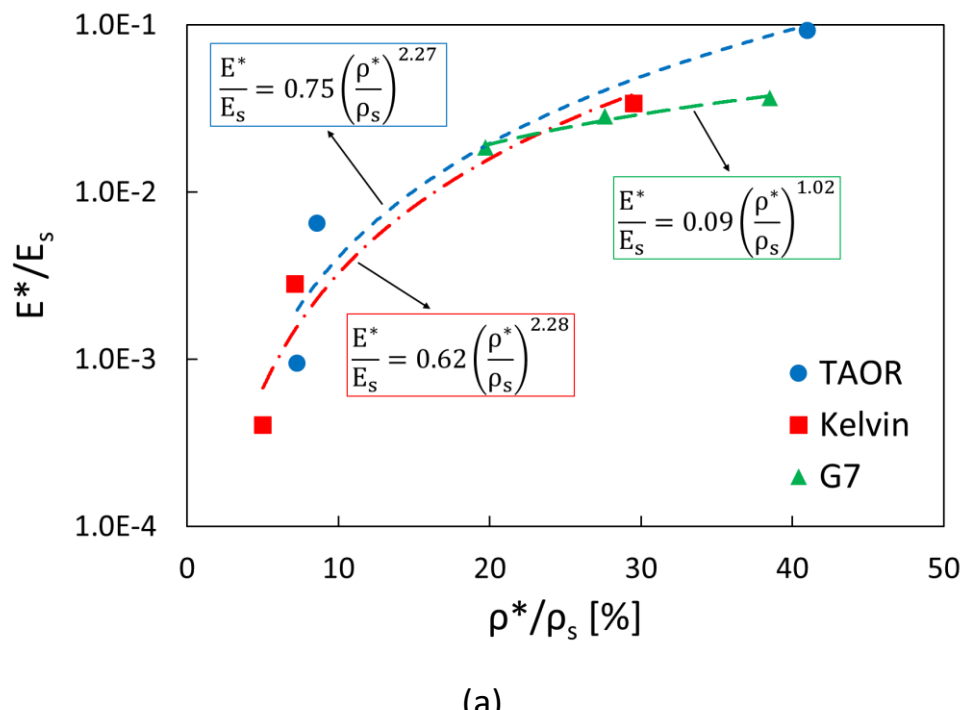
The comparison of the results of the compressive tests (section 3.1.3.) was conducted based on the designed relative density; however, in section 3.1.2. it was shown that the actual relative density differs from the designed one. A useful tool that allows the comparison of the lattice structures mechanical properties is the Gibson-Ashby model, described in section 2.1.2.

The model was applied for the mechanical characterization of the tested lattice structures and the power law relationships between mechanical properties and relative density evaluated. Relative modulus and relative strength evaluated from the compressive tests are reported, together with the actual relative density, in Table 11. The elastic modulus and the compressive strength of the Ti6Al4V ELI alloy were evaluated in a previous work conducted at the University of Messina [105].

**Table 11** Relative modulus, relative strength and actual relative density of the tested lattice structures

	TAOR 5%	TAOR 10%	TAOR 20%	Kelvin 5%	Kelvin 10%	Kelvin 20%	G7 5%	G7 10%	G7 20%
$E^*/E_s$	0.0009	0.0065	0.0918	0.0004	0.0028	0.0339	0.0185	0.0284	0.0365
$\sigma^*/\sigma_s$	0.0044	0.0300	0.1303	0.0020	0.0122	0.0461	0.0584	0.0900	0.1628
$\rho^*/\rho_s$ actual [%]	7	9	41	5	7	30	20	27	38

Relative modulus and relative strength plotted against relative density are shown in Fig. 35. The Gibson-Ashby constants of the power law relationship obtained by the data interpolation are reported, together with the coefficient of determination, in Table 12.



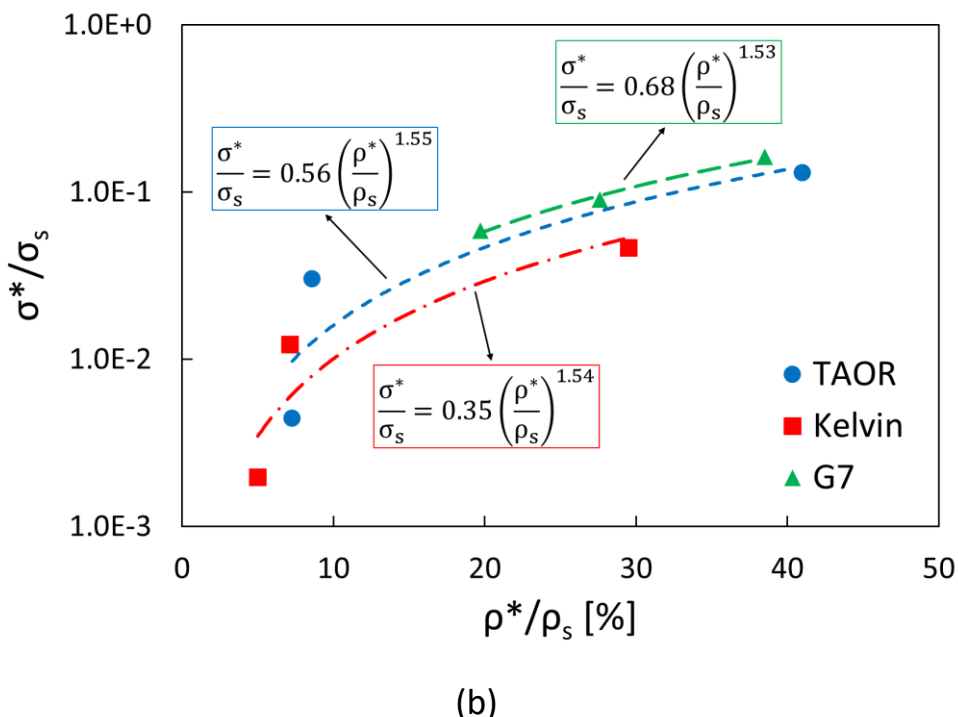


**Fig. 35** Gibson-Ashby diagrams: (a) relative modulus; (b) relative strength

**Table 12** Gibson-Ashby constants evaluated for the tested lattice structures

	Relative modulus			Relative strength		
	C	n	R <sup>2</sup>	C	n	R <sup>2</sup>
<b>TAOR</b>	0.75	2.27	0.99	0.56	1.55	0.97
<b>Kelvin</b>	0.62	2.28	0.99	0.35	1.54	0.97
<b>G7</b>	0.09	1.02	0.97	0.68	1.53	0.99

The data obtained for the TAOR cell have also been plotted in a Gibson-Ashby diagram obtained from literature, for the comparison with other lattice structures, as shown in Fig. 36.

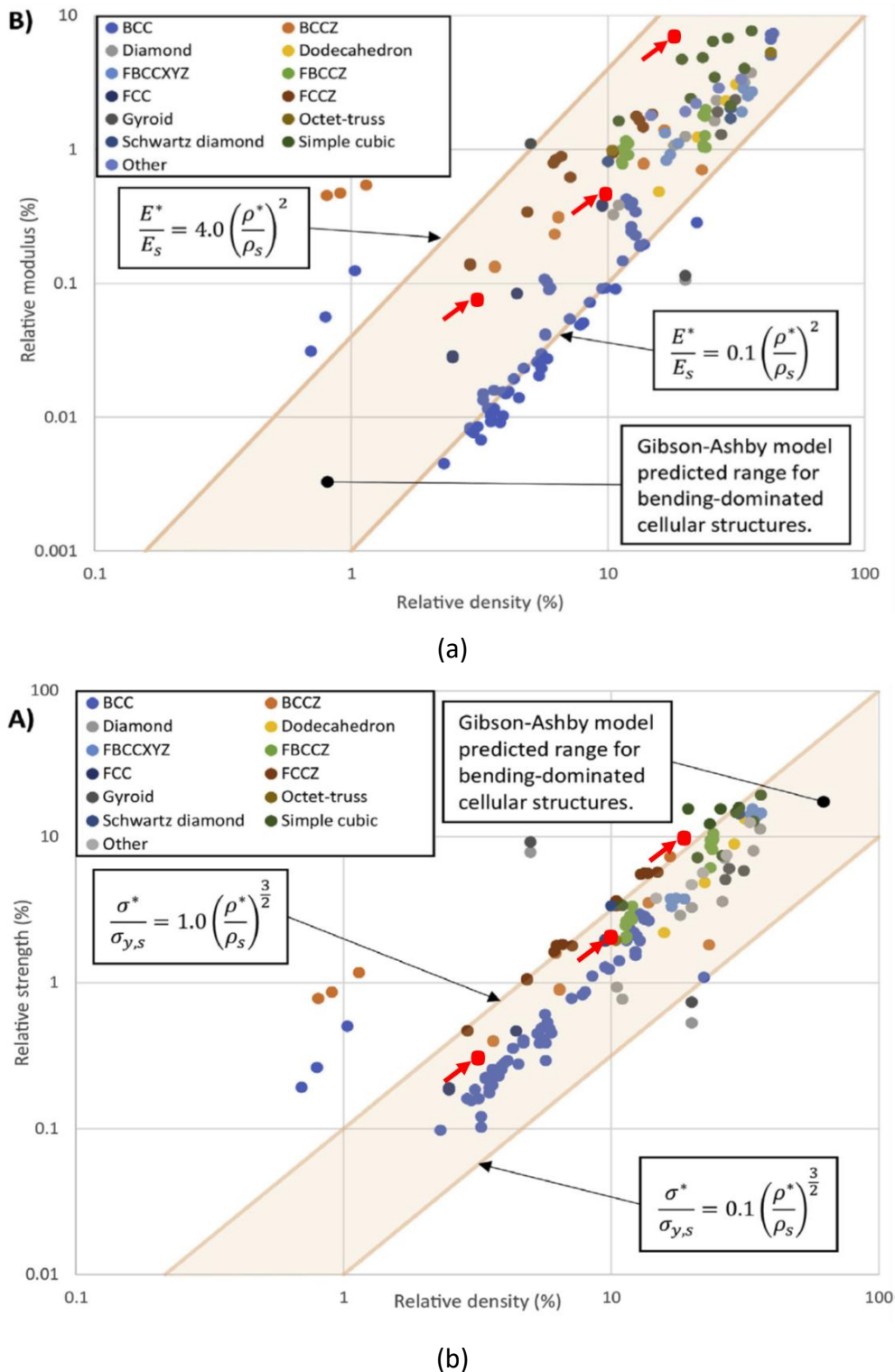


**Fig. 36** Gibson-Ashby model for the comparison of the TAOR with other unit cells: (a) relative modulus against relative density; (b) relative strength against relative density [10].

Red dots indicated with red arrows represent the results of the TAOR cell. The dots are in the predicted range for bending-dominated structures, as evaluated in section 2.2. with the Maxwell criterion.

Gibson-Ashby model allows the comparison of the mechanical properties of lattice structures for a given relative density. Considering the power law relationships obtained from the compressive tests, in Table 13 are reported the elastic modulus and the compressive strength of the tested lattice structures for the designed relative densities.

**Table 13** Mechanical properties of the tested lattice structures from Gibson-Ashby model

	TAOR 5%	TAOR 10%	TAOR 20%	Kelvin 5%	Kelvin 10%	Kelvin 20%	G7 5%	G7 10%	G7 20%
E [MPa]	96.9	466.3	2243.5	76.6	373.2	1817.6	543.3	1097.9	2218.6
$\sigma_m$ [MPa]	5.48	16.03	46.90	3.48	10.11	29.38	7.00	20.21	58.38

From the comparison of the tested lattice structures, G7 presents the highest mechanical properties while Kelvin presents the lowest. According to the Maxwell criterion (section 2.1.2.), all the tested structures exhibit bending dominated behaviour, since their Maxwell numbers are: -18 for the TAOR, -30 for the Kelvin, -5 for the G7. The results show that, while increasing the Maxwell number, the mechanical properties increase. It is worthy to mention that, as described in section 2.1.2., stretch dominated structures ( $M \geq 0$ ) exhibits higher elastic modulus and compressive strength compared to bending dominated structures ( $M < 0$ ) [114].

### 3.1.5. Failure mode analysis

Visual testing and SEM observations were performed to analyse the failure modes induced by the compression tests. All configurations analysed present a macroscopic failure in the form of a shear plane inclined with an angle of about  $45^\circ$ , as shown in Fig. 37. This behaviour is in accordance with data reported in literature for similar lattice structures [115].

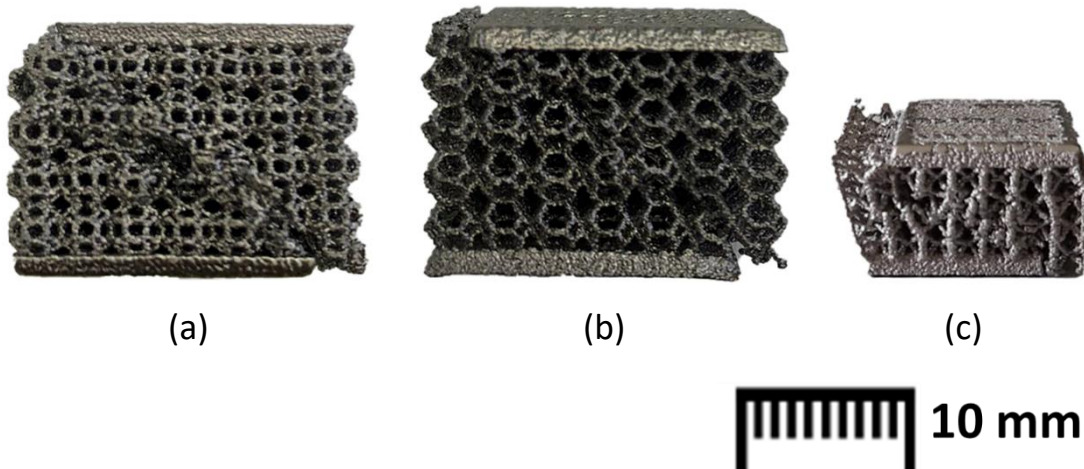


**Fig. 37** Failure mode for lattices of relative density 10%: (a) TAOR; (b) Kelvin; (c) G7

SEM analysis results are reported in Fig. 38 and Fig. 39 for the lattice structures with relative density 10%. The same behaviour can be observed for the other relative densities tested.

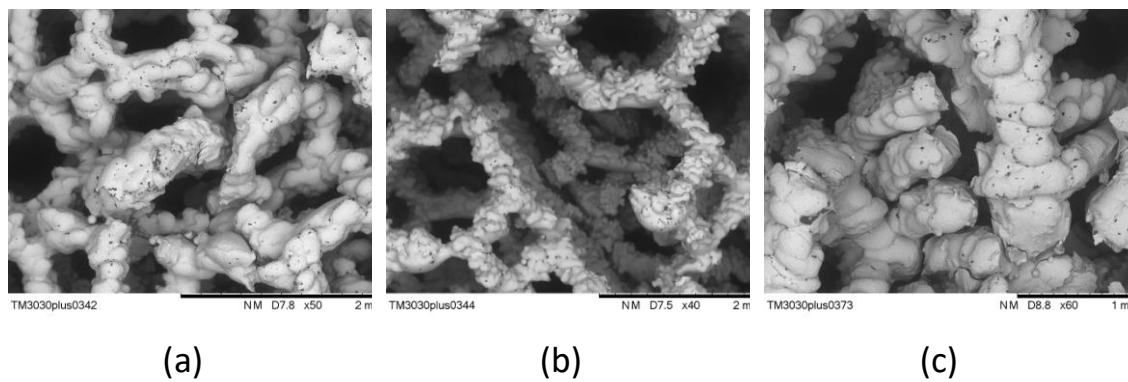


**Fig. 38** SEM images, unit cells fracture: (a) TAOR; (b) Kelvin; (c) G7

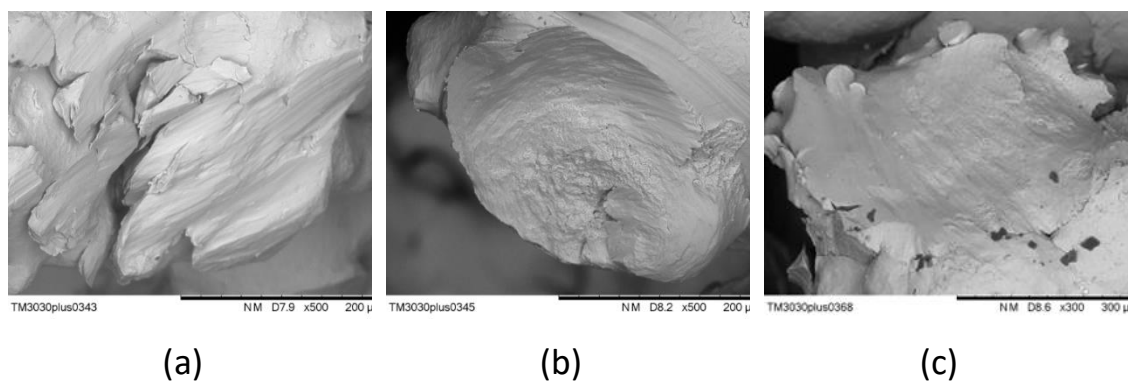


**Fig. 39** SEM images, particular of the surface fracture: (a) TAOR cell; (b) Kelvin cell

In Fig. 38 is reported the failure mode of the entire unit cells. For all cases the fractures were observed at the cross nodes of the structures, which are critical points due to stress intensification. In Fig. 39 a particular of the surface fracture, can be observed for all the lattice structures, that show different failure modes. In the TAOR cell the fracture occurs by sliding, while in the Kelvin and G7 cells a combined ductile and brittle fracture can be observed; moreover, notch effect is present in the Kelvin structure.

## 3.2. FINITE ELEMENT ANALYSIS

### 3.2.1. Linear static finite element analysis

A preliminary linear static FE analysis was conducted to estimate the elastic modulus of the new TAOR cell and the stress distribution within the lattice structure. Moreover, the unit cell size effect on mechanical response was evaluated.

Several works investigated the cell size effect on mechanical properties and found that an increase in the unit cell size leads to a reduction of elastic modulus and compressive yield strength [116], [117].

Six levels of relative densities were analysed, ranging from 5% up to 30%, with steps of 5%. Cubic specimens with 30 mm edge length were considered and four unit cell sizes evaluated: 5 mm, 6 mm, 7.5 mm and 10 mm. By this way, the specimens have respectively: 6, 5, 4 and 3 unit cells on each edge. No overlapping of adjacent struts of multiple cells was considered [118]. Relative density was calculated by applying the second method proposed in section 2.2.; therefore, by applying the equation 15, the dimensions of the TAOR cell were evaluated. In Table 14, Table 15, Table 16 and Table 17 are summarised the geometric parameters of the TAOR cells, referring to Fig. 30.

The FE models were meshed with first order tetrahedral elements. Different element sizes were adopted, based on the strut diameters. Thus, for each configuration, the element size is equal to 1/3 of the strut diameter  $d$ .

**Table 14** Geometric parameters of TAOR cell with 5 mm cell size

TAOR 5 mm						
$\rho^*/\rho_s$ [%]	5	10	15	20	25	30
D [mm]	5	5	5	5	5	5
d [mm]	0.29	0.43	0.54	0.65	0.75	0.85
L [mm]	0.85	0.85	0.85	0.85	0.85	0.85
a [mm]	1.65	1.46	1.30	1.16	1.01	0.87
d/D	0.06	0.09	0.11	0.13	0.15	0.17
d/L	0.34	0.51	0.64	0.76	0.88	1

**Table 15** Geometric parameters of TAOR cell with 6 mm cell size

TAOR 6 mm						
$\rho^*/\rho_s$ [%]	5	10	15	20	25	30
D [mm]	6	6	6	6	6	6
d [mm]	0.35	0.52	0.65	0.78	0.89	1.02
L [mm]	1.02	1.02	1.02	1.02	1.02	1.02
a [mm]	1.98	1.76	1.56	1.39	1.22	1.05
d/D	0.06	0.09	0.11	0.13	0.15	0.17
d/L	0.34	0.51	0.64	0.76	0.88	1

**Table 16** Geometric parameters of TAOR cell with 7.5 mm cell size

	<b>TAOR 7.5 mm</b>					
$\rho^*/\rho_s [\%]$	5	10	15	20	25	30
D [mm]	7.5	7.5	7.5	7.5	7.5	7.5
d [mm]	0.44	0.65	0.81	0.97	1.12	1.28
L [mm]	1.28	1.28	1.28	1.28	1.28	1.28
a [mm]	2.48	2.19	1.95	1.73	1.52	1.31
d/D	0.06	0.09	0.11	0.13	0.15	0.17
d/L	0.34	0.51	0.64	0.76	0.88	1

**Table 17** Geometric parameters of TAOR cell with 10 mm cell size

	<b>TAOR 10 mm</b>					
$\rho^*/\rho_s [\%]$	5	10	15	20	25	30
D [mm]	10	10	10	10	10	10
d [mm]	0.58	0.86	1.08	1.30	1.50	1.70
L [mm]	1.70	1.70	1.70	1.70	1.70	1.70
a [mm]	3.30	2.92	2.60	2.32	2.02	1.74
d/D	0.06	0.09	0.11	0.13	0.15	0.17
d/L	0.34	0.51	0.64	0.76	0.88	1

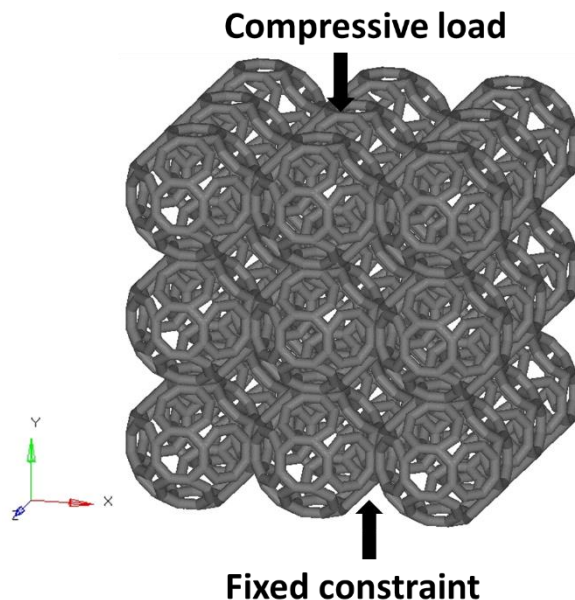
The FE models were meshed with first order tetrahedral elements. Different element sizes were adopted, based on the strut diameters. Thus, for each configuration, the element size is equal to 1/3 of the strut diameter d.

The selected material for the analysis is the titanium alloy Ti6Al4V ELI, the main mechanical properties are reported in Table 2. Only the elastic region of the titanium alloy was modelled, since it is not expected to reach the yield strength of the material with the applied loads.

**Table 18** Ti6Al4V ELI alloy mechanical properties [105]

	<b>E [GPa]</b>	<b>v</b>	<b><math>\rho</math> [kg/m<sup>3</sup>]</b>
<b>Ti6Al4V ELI</b>	115	0.34	4430

Boundary conditions were applied as reported in Fig. 40.

**Fig. 40** Linear static FE model boundary conditions

A compressive load of 1 kN along y axis has been applied directly to the specimen, while a fixed constraint was applied to the inferior end of the lattice structure.

The results of the FE analysis are reported in Fig. 41, Fig. 42, Fig. 43, Fig. 44, Fig. 45 and Fig. 46.

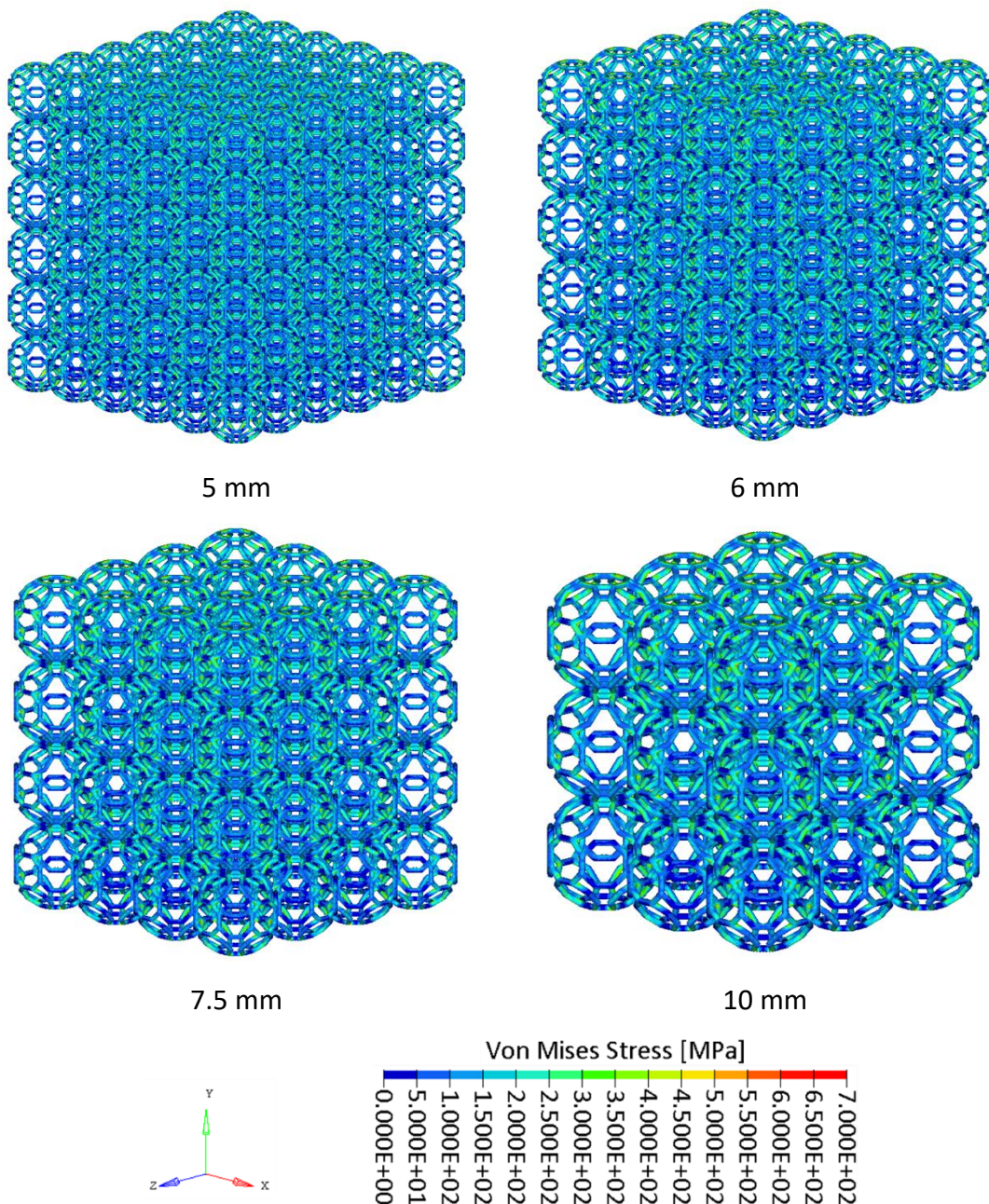


**Fig. 41** Linear static FE analysis results of TAOR with relative density 5%

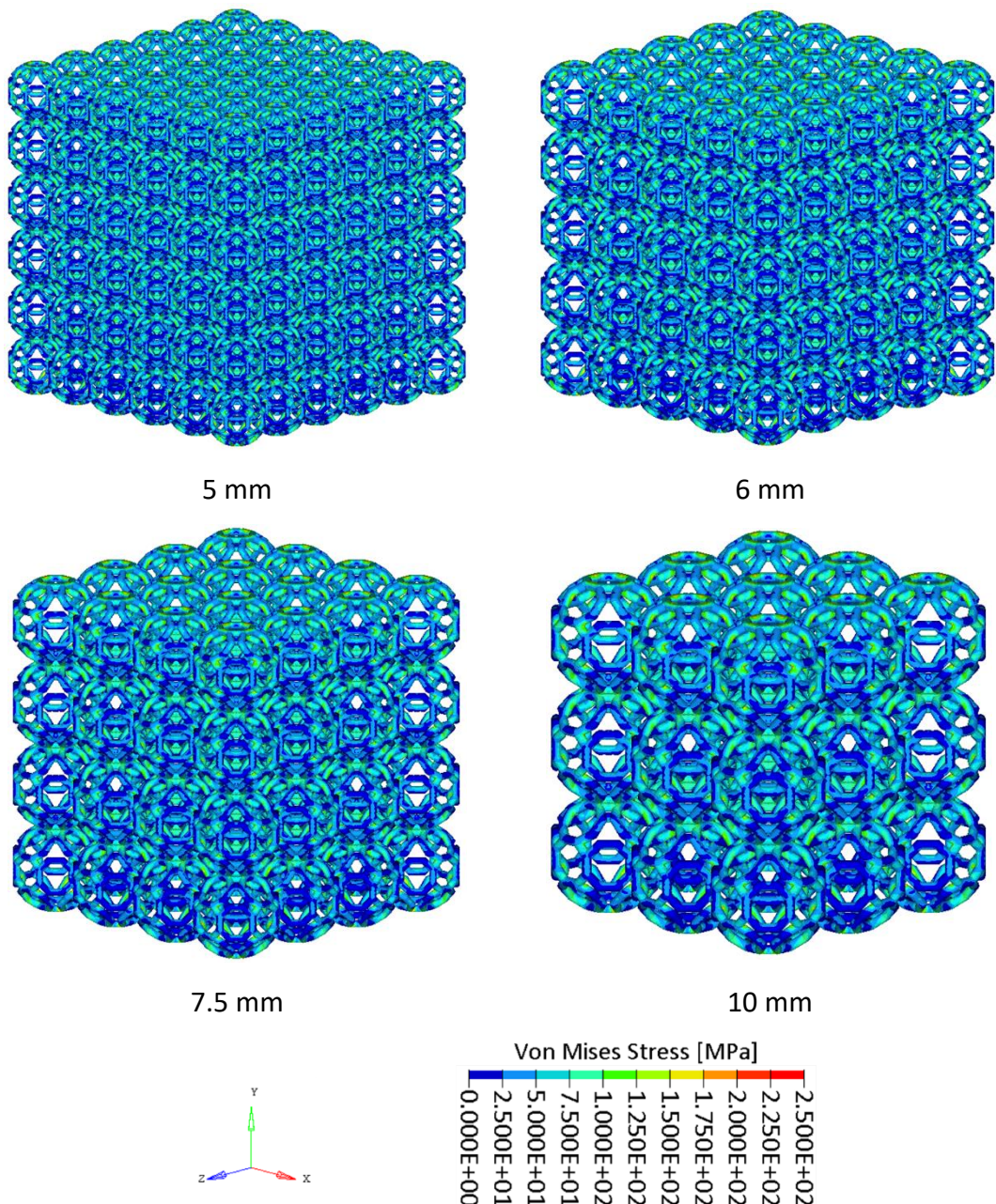


**Fig. 42** Linear static FE analysis results of TAOR with relative density 10%

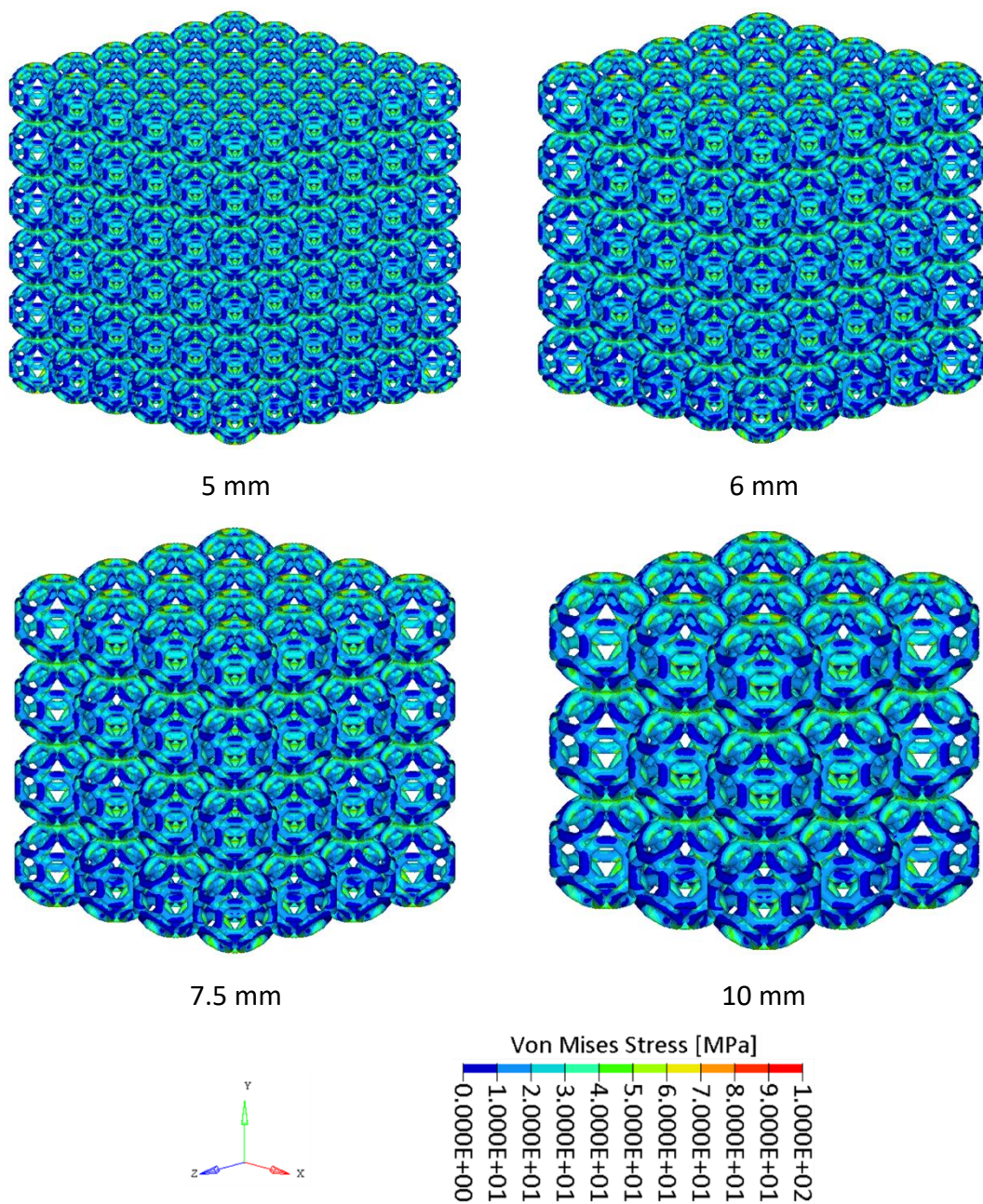


**Fig. 43** Linear static FE analysis results of TAOR with relative density 15%

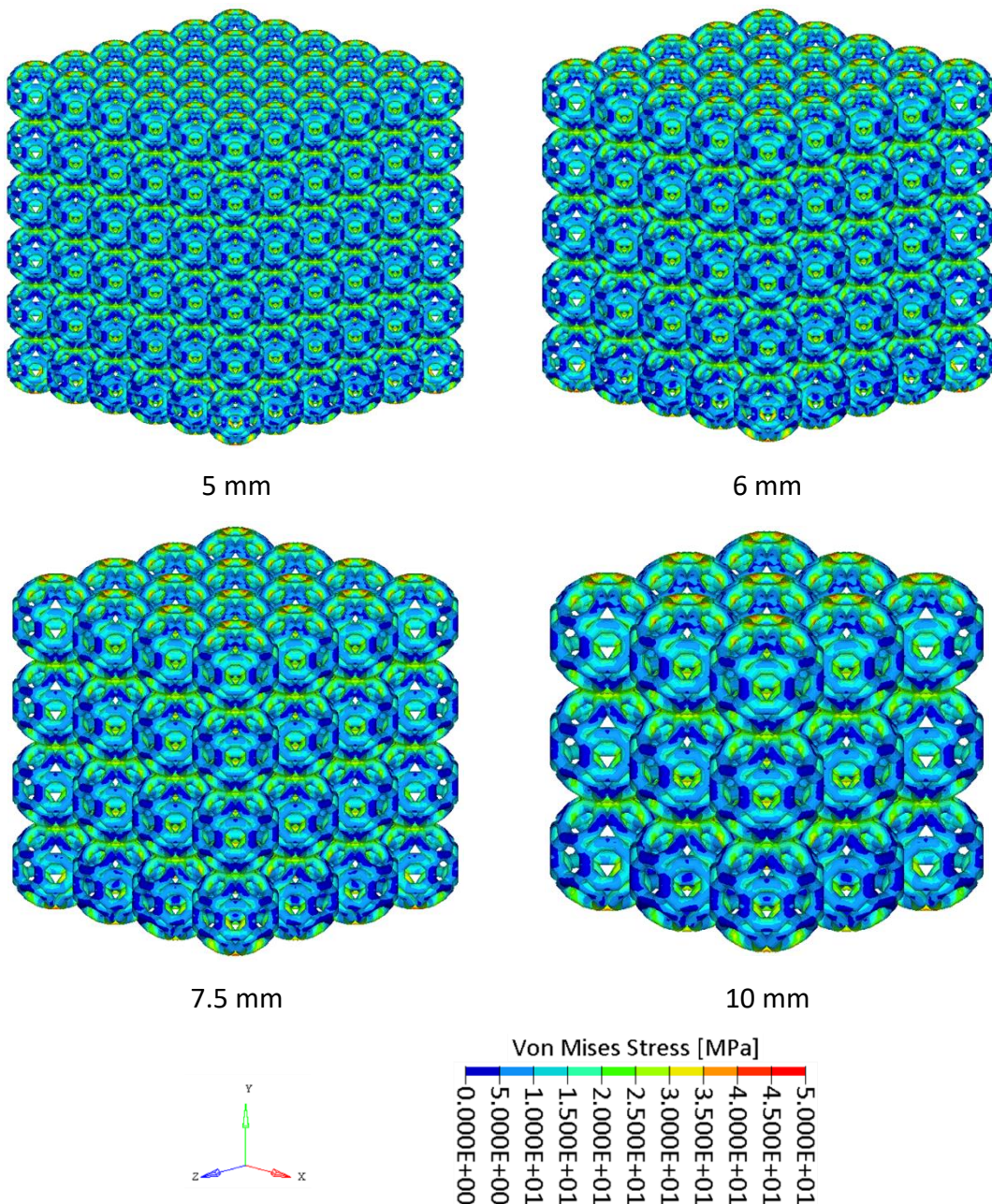


**Fig. 44** Linear static FE analysis results of TAOR with relative density 20%

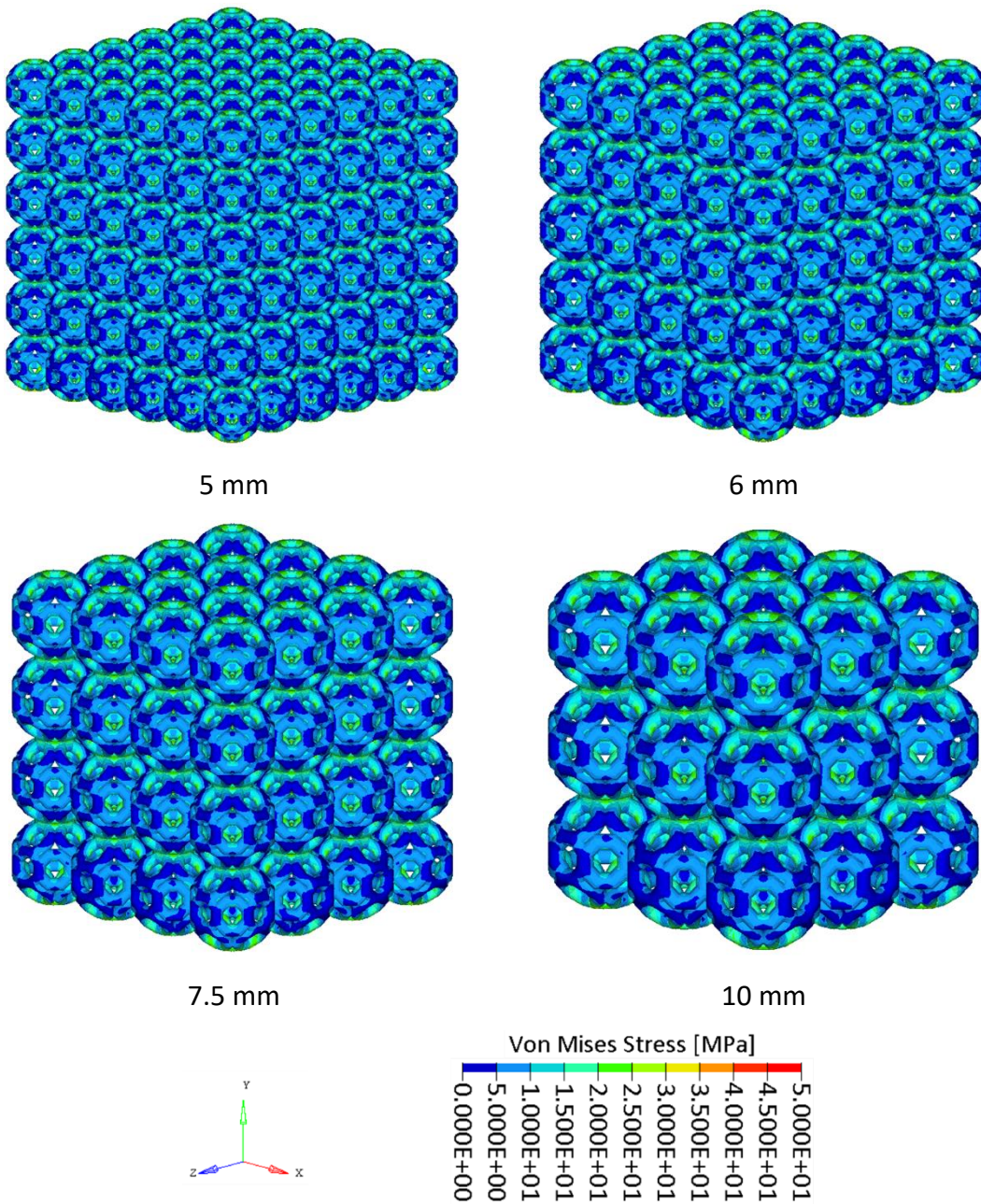


**Fig. 45** Linear static FE analysis results of TAOR with relative density 25%

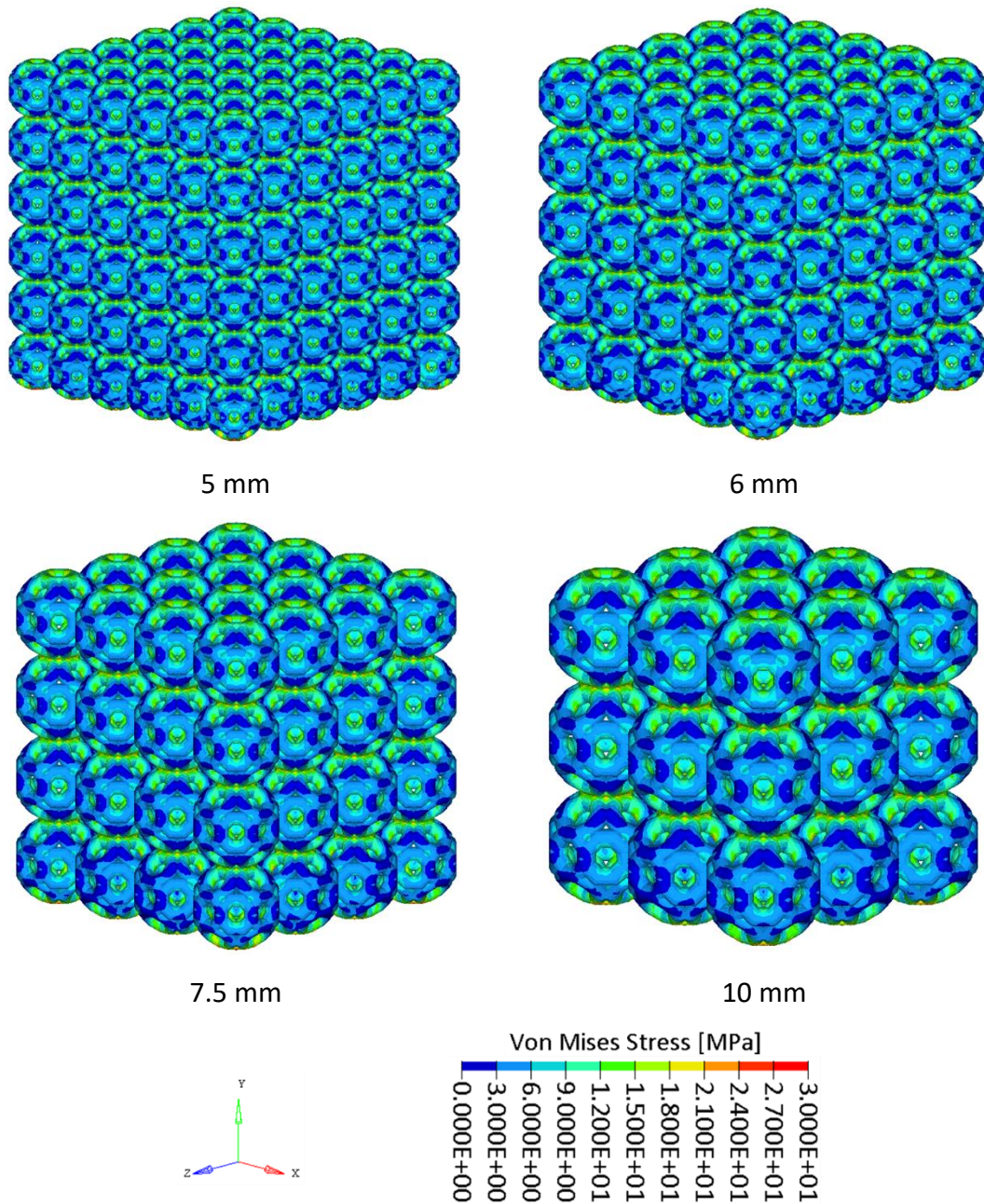


**Fig. 46** Linear static FE analysis results of TAOR with relative density 30%

The stress distribution is not affected by the cell size, the pore size and the porosity. For all the configurations, higher stresses are depicted on the struts at the contact between two adjacent cells. These struts are located on the faces of the TAOR cells inclined at 45° respect to the loading direction. Peak stresses are located at the nodes of the structures, local stress values increase at the decrease of the relative density. Also cell size affects the local stress values; indeed, for a given relative density, they increase while cell size decrease. The effect off the cell size is more pronounced in the lower relative densities,

as shown in Fig. 47. The results are summarised in Table 19, Table 20, Table 21 and Table 22, where is also reported the equivalent elastic modulus of the lattice materials. The elastic modulus was evaluated with the same method applied during compressive tests (section 3.1.3.); first, stress and strain were evaluated from the load-displacement data. Stress was obtained as the ratio between the load and the cross section of lattice specimens, whereas strain was evaluated from the displacement divided by the initial height of the specimen; after that, elastic modulus was evaluated as the ratio between stress and strain.

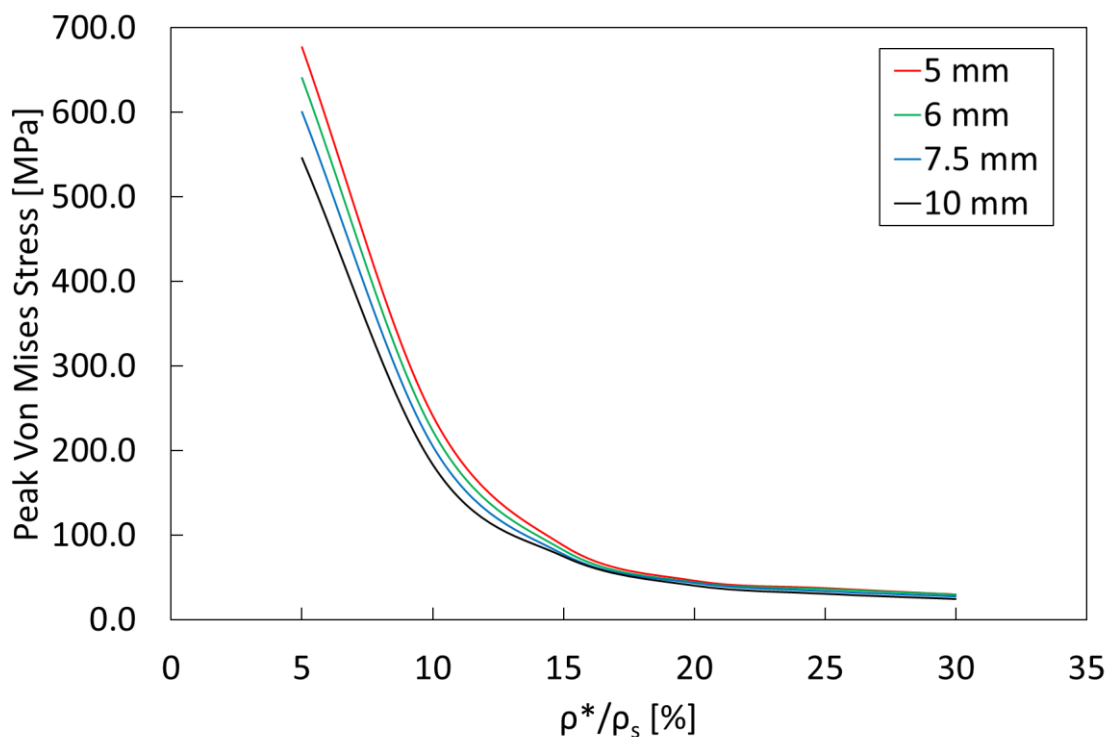


**Fig. 47** Peak Von Mises stresses for different cell sizes and relative densities

**Table 19** Linear static FE analysis results of TAOR with 5 mm cell size

TAOR 5 mm						
$\rho^*/\rho_s [\%]$	5	10	15	20	25	30
Peak stress [MPa]	676.9	241.4	87.9	46.3	37.5	30.0
E [MPa]	131.9	571.2	1892.9	3803.9	5153.6	7404.1

**Table 20** Linear static FE analysis results of TAOR with 6 mm cell size

<b>TAOR 6 mm</b>						
<b><math>\rho^*/\rho_s [\%]</math></b>	5	10	15	20	25	30
<b>Peak stress [MPa]</b>	640.4	223.4	82.2	44.2	36.2	29.7
<b>E [MPa]</b>	131.1	567.0	1884.3	3772.4	5133.7	7369.7

**Table 21** Linear static FE analysis results of TAOR with 7.5 mm cell size

<b>TAOR 7.5 mm</b>						
<b><math>\rho^*/\rho_s [\%]</math></b>	5	10	15	20	25	30
<b>Peak stress [MPa]</b>	600.4	205.2	77.2	43.2	33.5	27.2
<b>E [MPa]</b>	129.1	560.3	1864.3	3703.3	5119.5	7254.3

**Table 22** Linear static FE analysis results of TAOR with 10 mm cell size

<b>TAOR 10 mm</b>						
<b><math>\rho^*/\rho_s [\%]</math></b>	5	10	15	20	25	30
<b>Peak stress [MPa]</b>	545.8	183.6	75.0	40.6	30.8	24.7
<b>E [MPa]</b>	126.7	551.3	1843.7	3640.2	5035.2	7251.1

Elastic modulus significantly increases at the increase of the relative density, while it slightly decreases at the increase of the cell size. The effect of cell size is more pronounced in the greater relative density, that is observable in the Gibson-Ashby diagram reported in Fig. 48.

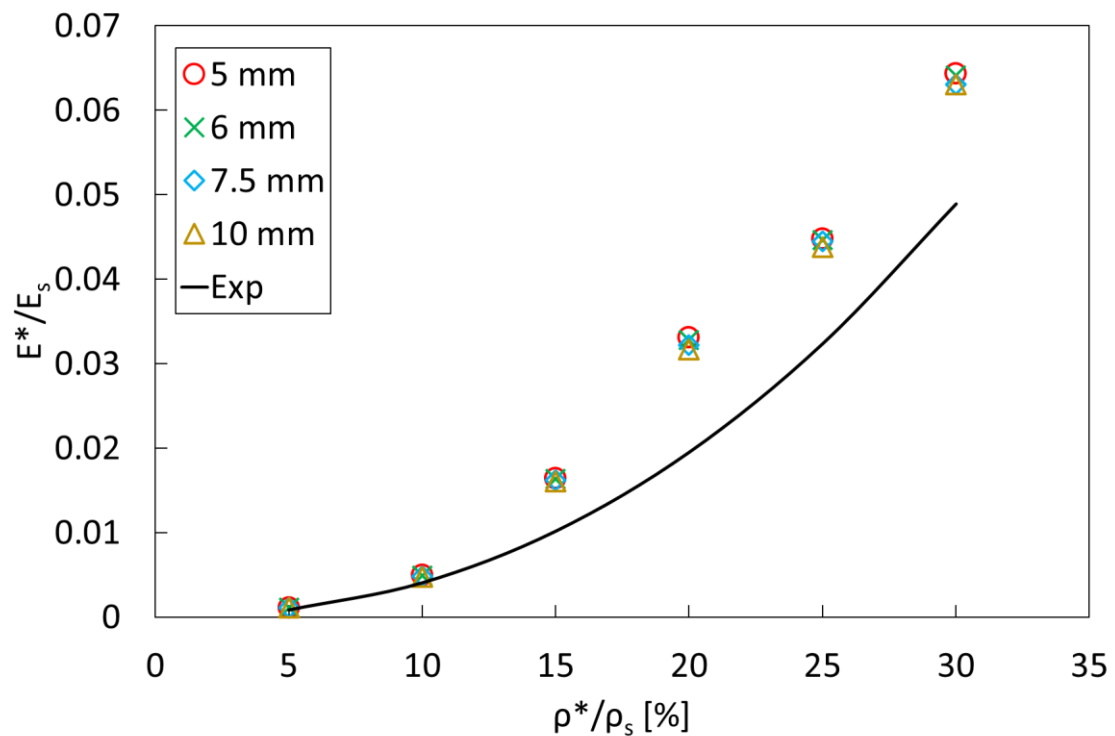


**Fig. 48** Gibson-Ashby diagram of the linear static FE analysis results

In Fig. 48 is also reported a comparison between the results of the FE analysis and the results of the Gibson-Ashby model obtained from compressive tests (section 3.1.4.). As it can be seen, the numerical model overestimates the elastic modulus of the lattice material, the differences between numerical and experimental results increase at the increase of the relative density. In Table 23 are reported the Gibson-Ashby constants of the power law relationship between relative modulus and relative density and the respective coefficients of determination.

**Table 23** Gibson-Ashby constant of the linear static FE analysis

	<b>5 mm</b>	<b>6 mm</b>	<b>7.5 mm</b>	<b>10 mm</b>	<b>Exp</b>
<b>C</b>	1.16	1.15	1.14	1.14	0.75
<b>n</b>	2.31	2.31	2.31	2.32	2.27
<b>R<sup>2</sup></b>	0.98	0.98	0.98	0.99	0.99

### 3.2.2. Johnson-Cook constitutive material model

Johnson-Cook (JC) material model is considered as one of the most used phenomenological constitutive model [119], [120]. When materials are subjected to dynamic load conditions such as high velocity impact or metal forming operations, a wide range of strains, strain rates, temperatures and pressures may be experienced. To distinguish dynamic material properties from static ones, it is important that the effect of each variable is properly assessed [121]. Constitutive modelling has been successfully applied in FE models to predict the dynamic deformation behaviour of various materials. Constitutive equation which represents the flow behaviour of materials is used as input in the FE model for simulating the material response under the specified loading conditions. The accuracy of prediction of the constitutive equation determines the reliability of numerical results solved by FE simulation results [122].

The constitutive material model proposed by Johnson-Cook consists of two parts: a strength model and a fracture model. The strength model is necessary to perform computation to evaluate the fracture model. The strength model for the Von Mises tensile stress  $\sigma$  is expressed as [121]:

$$\sigma = [A + B\varepsilon^n][1 + C \ln \dot{\varepsilon}^*][1 - T^{*m}] \quad (18)$$

Where  $\varepsilon$  is the equivalent plastic strain,  $\dot{\varepsilon}^*$  is the plastic strain rate for  $\dot{\varepsilon}_0 = 1.0 \text{ s}^{-1}$ ,  $T^*$  is the homologous temperature, defined as the ratio between the temperature of the material and the temperature at the melting point.  $A$ ,  $B$ ,  $n$ ,  $C$  and  $m$  are material constants and represent:  $A$  the yield strength of the material at the reference strain rate and room temperature,  $B$  the strain hardening constant,  $n$  the strain hardening coefficient,  $C$  the strain rate strengthening coefficient and  $m$  the thermal softening coefficient [119]. The expression in the first set of brackets gives the stress as function of strain for  $\dot{\varepsilon}^* = 1$  and  $T^* = 0$ . The expressions in the second and third sets of brackets represent the effect of strain rate and temperature [121].

The fracture model is a cumulative-damage model which attempts to isolate the effects of strain rate, temperature and pressure on the strain to fracture. It also attempts to account for path dependency by accumulating damage as the deformation proceeds [121]. The damage to an element is defined as:

$$D = \sum \frac{\Delta \varepsilon}{\varepsilon^f} \quad (19)$$

Where  $\Delta \varepsilon$  is the increment of equivalent plastic strain which occurs during an integration cycle,  $\varepsilon^f$  is the equivalent strain to fracture, under the current condition of strain rate, temperature, pressure and equivalent stress. Fracture is reached when  $D = 1$ .

The equation of the strain rate at fracture is expressed as:

$$\varepsilon^f = [D_1 + D_2 e^{D_3 \sigma^*}] [1 + D_4 \ln \dot{\varepsilon}^*] [1 + D_5 T^*] \quad (20)$$

Where  $\sigma^*$  is defined as the ratio between the hydrostatic stress and the Von Mises equivalent stress.  $D_1$ ,  $D_2$ ,  $D_3$ ,  $D_4$  and  $D_5$  represent material constant. The expression in the first set of brackets assess that the strain to fracture decreases as the hydrostatic stress increases. The expressions in the second and third sets of brackets represent the effect of strain rate and temperature.

The JC constitutive model was applied in the development of a non-linear FE model. The selected material was the titanium alloy Ti6Al4V ELI, already used for the compressive tests presented in section 3.1.3.. Several works evaluated the JC strength model material constant, as reported in Table 24.

**Table 24** Material constants of JC model suggested for Ti6Al4V alloy

References	A [MPa]	B [MPa]	C	n	m	$\dot{\varepsilon}_0$ [ $s^{-1}$ ]
Kotkunde <i>et al.</i> [123]	869.4	649.5	0.0093	0.3867	0.7579	$10^{-2}$
Yan <i>et al.</i> [124]	862	331	0.012	0.34	1.1	1
Cakircali <i>et al.</i> [125]	928	1062	0.0167	0.62	0.75	$10^{-3}$
Lee and Lin [126]	724.7	683.1	0.035	0.47	1	$10^{-5}$
Meyer and Kleponis [127]	896	656	0.0128	0.5	0.8	1

As shown in Table 24 the JC parameters are quite different, due to different identification conditions. All this availability present in literature, is a sort of weakness, as it is difficult

to choose the set that will provide the most accurate results. Ducobu *et al.* [128] highlighted the importance of the choice of the parameters of JC constitutive model and their influence on the results of a FE simulation.

Altair HyperWorks 14.0 (Altair Engineering, MI) software package and RADIOSS as explicit solver were used to develop the FE model of the present PhD thesis. The RADIOSS solver allows the application of a simplified Johnson-Cook model by applying the following equations:

$$A = \sigma_y \quad (21)$$

$$B = \frac{\sigma_u}{n \varepsilon_u^{(n-1)}} \quad (22)$$

$$n = \frac{\sigma_u \varepsilon_u}{\sigma_u - \sigma_y} \quad (23)$$

Where  $\sigma_y$  represents the yield strength, while  $\sigma_u$  and  $\varepsilon_u$  are respectively the true ultimate stress and the true strain at the ultimate stress.

Due to the difficulty in the choice of the most suitable JC parameters, the material constants were calculated from results of previous tensile tests carried out in the laboratory of the Department of Engineering at the University of Messina [105]. The tests were performed on specimens of the dimensions reported in Table 25 referring to Fig. 49.

**Table 25** Tensile specimen dimensions

A [mm]	B [mm]	L [mm]	C [mm]	W [mm]	T [mm]
25	43,5	186	22,8	15	7,15

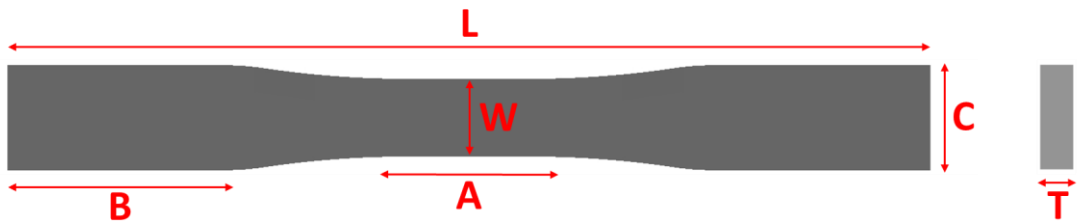


**Fig. 49** Tensile specimen

Table 26 reports the mechanical properties of the Ti6Al4V ELI alloy evaluated in the tensile tests.

**Table 26** Mechanical properties of the Ti6Al4V ELI alloy

	E [GPa]	v	$\sigma_y$ [MPa]	$\sigma_m$ [MPa]	$\epsilon_m$ [%]	$\epsilon_b$ [%]	$\epsilon_0$ [s <sup>-1</sup> ]
Ti6Al4V ELI	115	0.34	905	1006	9.4	17.3	$10^{-3}$

Where E and v represent the Young's modulus and the Poisson's ratio,  $\sigma_m$  and  $\epsilon_m$  are the engineering tensile strength and the engineering strain at the tensile strength,  $\epsilon_b$  is the elongation at break and  $\epsilon_0$  the strain rate.

The JC strength model parameters of Ti6Al4V ELI alloy are reported in Table 27.

**Table 27** JC strength model parameters of Ti6Al4V ELI alloy

	A [MPa]	B [MPa]	n	C	m	$\sigma_{MAX}$ [MPa]	$\epsilon_{MAX}$ [%]
Ti6Al4V ELI	908.8	631.7	0.497	0.0093	0.7579	1110.4	16.5

Where  $\sigma_{MAX}$  and  $\varepsilon_{MAX}$  are respectively the true maximum stress and the true failure plastic strain. The parameters C and m were selected from [123] due to similar test conditions. The JC fracture model was also implemented: data were obtained from [129]. The parameters are reported in Table 28.

**Table 28** JC fracture model parameters of Ti6Al4V ELI alloy

	<b>D<sub>1</sub></b>	<b>D<sub>2</sub></b>	<b>D<sub>3</sub></b>	<b>D<sub>4</sub></b>	<b>D<sub>5</sub></b>
<b>Ti6Al4V ELI</b>	-0.09	0.27	-0.48	0.014	3.87

The material model validation was performed on the tensile specimen shown in Fig. 49. The specimen was meshed with first order hexahedral elements of 2 mm. Boundary conditions were applied to replicate the experimental tests: an imposed velocity of 1 mm/min along y axis was applied, while the other end was fixed constrained, as shown in Fig. 50.

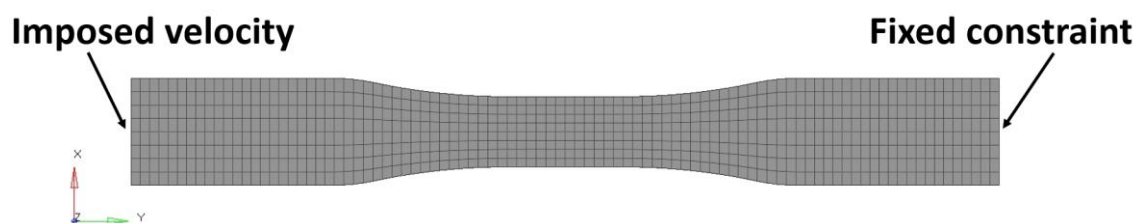


**Fig. 50** Boundary conditions FE model tensile test

A comparison between the results obtained during experimental tests and FE analysis is reported in Fig. 51 and in Table 29.

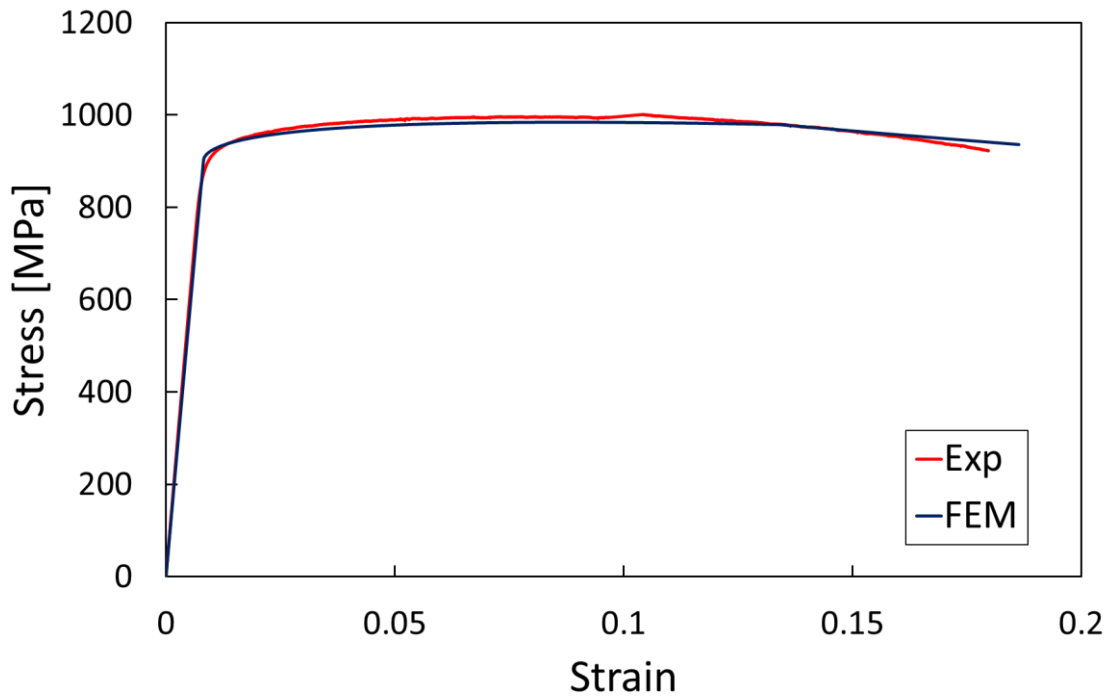


**Fig. 51** Comparison between the results of the experimental test and the FE analysis for the validation of the material model

**Table 29** Evaluation of the percentage error of the results of the tensile tests

	$\sigma_m$ [MPa]	$\epsilon_m$	$\sigma_b$ [MPa]	$\epsilon_b$
<b>Experimental</b>	1006	0.094	921	0.173
<b>FEM</b>	984.9	0.089	936	0.178
<b>Error [%]</b>	-2.09	-5.31	1.63	2.89

Where  $\sigma_b$  is the engineering strength at the fracture point. The percentage errors are evaluated regard to the experimental results.

The JC material model was thus validated, and it was verified that it well simulates the plastic behaviour of the Ti6Al4V ELI alloy. In addition, it was verified if the proposed material model is suitable for the simulation of the plastic behaviour of a lattice material.

Therefore, a further validation was performed with a FE analysis of a G7 lattice specimen with relative density 10% and the same dimensions of the one used for the experimental tests and reported in Table 5 seen in section 3.1.1.. The specimen was meshed with first order hexahedral elements of 0.06 mm. Boundary conditions were applied to replicate the compressive test: an imposed velocity of 1 mm/min along y axis was applied, while the other end was fixed constrained, as shown in Fig. 52.

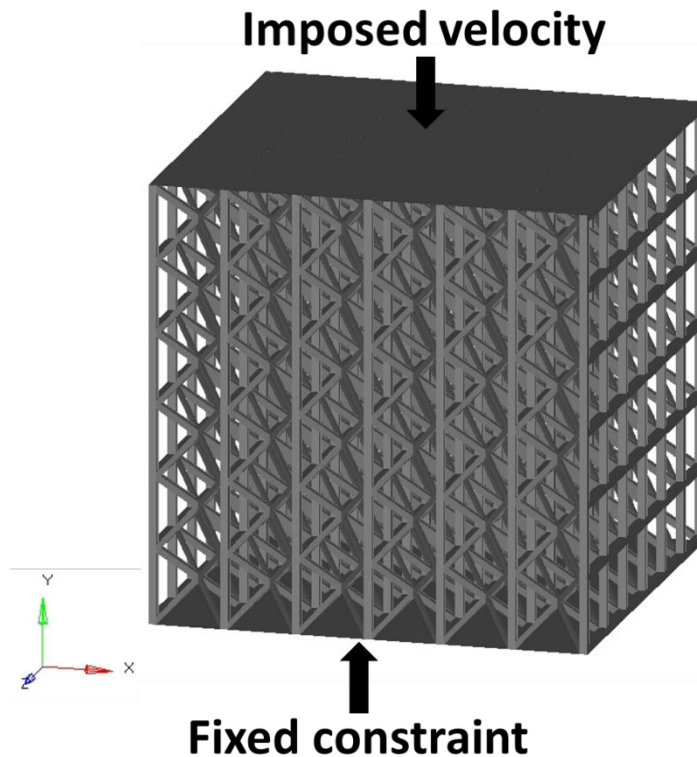


**Fig. 52** Boundary conditions for FE model validation

As seen in section 3.1.2., the actual specimen relative density differs from the designed one, thus a direct comparison with the results of the compressive tests (section 3.1.3.) was not possible. To perform a reliable FE model validation, is necessary comparing lattice structures with the same relative density. The results of the Gibson-Ashby model, presented in section 3.1.4. were taken into account for this purpose. By considering a lattice structure with relative density 10% and by applying the power law relationship between relative strength and relative density evaluated for the G7 lattice, the compressive strength is 20.21 MPa. The stress-strain curve of the FE analysis was obtained from the load-displacement FE results, with the same method adopted during compressive tests, seen in section 3.1.3.. The results are shown in Fig. 53.

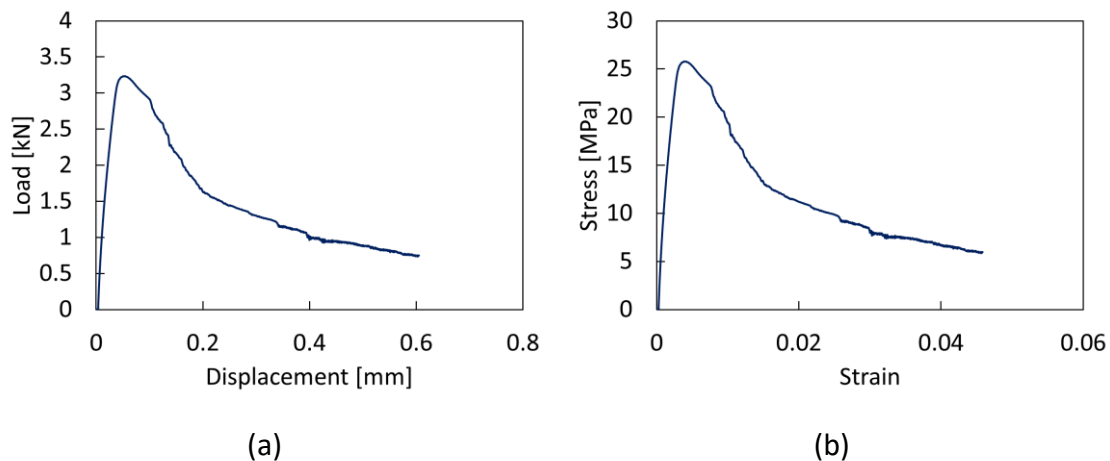


**Fig. 53** (a) load-displacement and (b) stress-strain curve of the FE validation analysis

The FE model compressive strength is 25.78 MPa, which it was considered an acceptable result, since the FE model specimen does not incorporate the defects of the actual specimen, due to the manufacturing process, that affects the mechanical properties of the lattice material [130].

The failure mode of the G7 specimen FE model, showed in Fig. 54, was compared with that obtained from compressive test and presented in section 3.1.5.

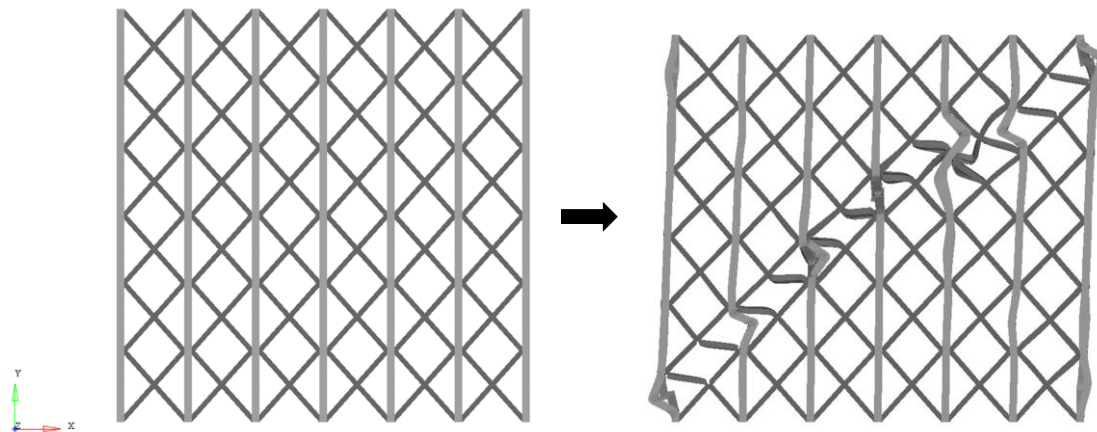


**Fig. 54** Failure mode of the G7 specimen FE analysis for the validation of the JC material model to simulate the plastic behaviour of lattice materials

The FE analysis result presents a macroscopic failure in the form of a shear plane inclined with an angle of about  $45^\circ$ , as that shown in Fig. 37 seen in section 3.1.5. for the compressive specimens.

### 3.2.3. Finite element analysis of the single unit cell

The JC material model described in section 3.2.2. was employed to develop a FE model of the single unit cell. Peng et al. [15] evaluated the differences between the behaviours of a single unit cell and that of a lattice with multiple unit cells. They developed a FE model to compare lattice structures with 1, 8 and 27 unit cells. They showed that the number of unit cells has a limited effect on the behaviour of the structure within the elastic region, while the stress-strain curves diverge after yielding point. Indeed, in the plastic region, depending on the cell shape, the mechanical properties of the single unit cell can be overestimated or underestimated. However, the differences in the compressive strength are in the order of 10%, thus the mechanical properties of a lattice material can be estimated by carrying out analyses on the single unit cell. Moreover, they showed that the stress distribution change between the single unit cell and the lattices where cells are connected to each other.

The aim of the present FE analysis is to evaluate the compressive behaviour and the failure mode of the single unit cell, without the presence of adjacent cells that affect the deformation process [131]. The model does not aim to evaluate the mechanical properties of the lattice structure.

The selected unit cells are TAOR cell, Kelvin cell and G7 cell already analysed by means of compressive tests described in section 3.1.3. moreover, a TPMS structure, the IWP unit cell was introduced. As described in section 2.1.1., TPMS structures show higher fatigue strength and higher structural performance than the strut-based lattice structures. IWP was chosen because, as well as the G7 unit cell, it is a BCC derived unit cell, allowing a direct comparison between cell with similar concepts. As all the TPMS structure, the IWP is defined as a combination of trigonometric functions in an implicit form [132].

$$\begin{aligned}\Phi_{IWP} \equiv & 2(\cos x \cos y + \cos y \cos z + \cos z \cos x) \\ & - (\cos 2x + \cos 2y + \cos 2z) = c\end{aligned}\tag{24}$$

Unit cells geometric parameters are the same described in section 3.1.1; furthermore, for the G7 cell, two cell sizes were analysed for each relative density. Thus, a strut size of 0.5 mm was imposed and cell sizes evaluated as mentioned in section 3.1.1.. MATLAB R2021a (MathWorks, MA) MS Lattice [108] toolbox was used to obtain IWP cell

configurations. IWP cell sizes were imposed equal to the G7 ones, while cell thicknesses were changed to obtain the selected relative densities. Unit cells geometric parameters are summarised in Table 30, Table 31 and Table 32. The geometric parameters refer to Fig. 30, Fig. 17 and Fig. 18.

**Table 30** Geometric parameters of TAOR cell and Kelvin cell for FE analysis

	TAOR cell			Kelvin cell		
$\rho^*/\rho_s$ [%]	5	10	20	5	10	20
D [mm]	4.4	3	2.1	4.4	3	2.1
d [mm]	0.2	0.2	0.2	0.2	0.2	0.2
L [mm]	0.72	0.48	0.33	1.55	1.06	0.74
a [mm]	1.61	1.03	0.66	2.48	1.63	1.08
d/D	0.045	0.067	0.095	0.045	0.067	0.095
d/L	0.28	0.42	0.61	0.13	0.19	0.27

**Table 31** Geometric parameters of G7 cell for FE analysis

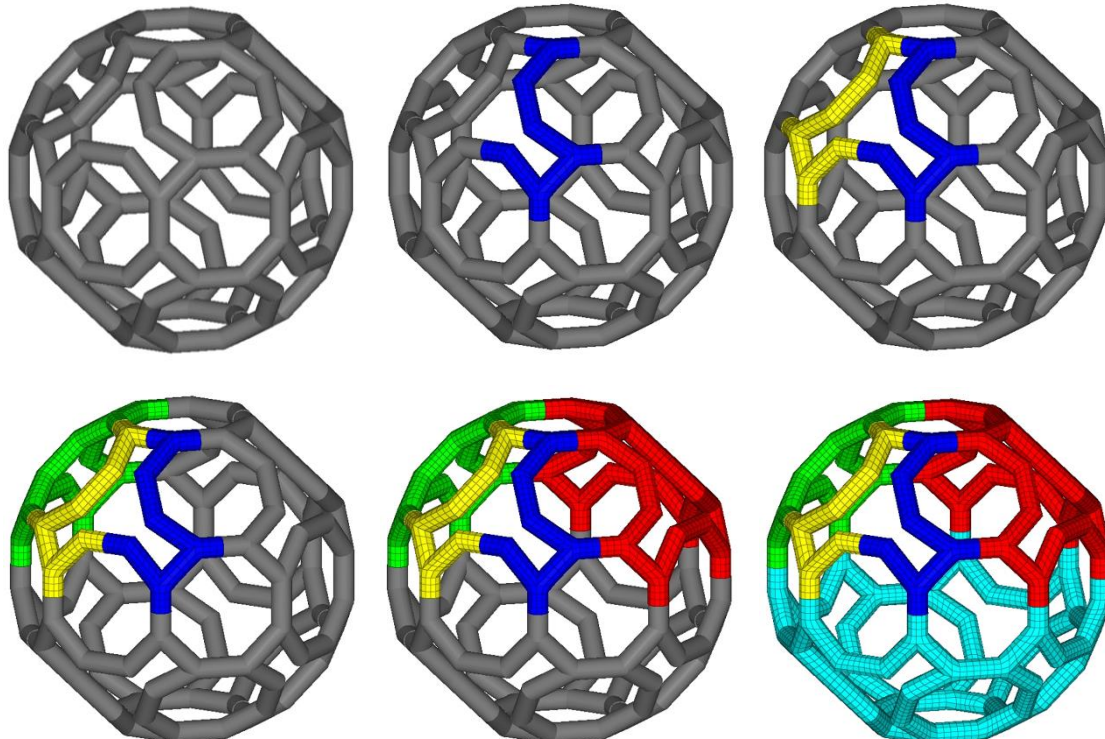
	G7 cell					
$\rho^*/\rho_s$ [%]	5	10	20	5	10	20
D [mm]	2.9	2.1	1.4	7.3	5	3.5
d [mm]	0.2	0.2	0.2	0.5	0.5	0.5
L [mm]	2.28	1.59	0.98	5.75	3.76	2.46
a [mm]	1.70	1.14	0.65	4.29	2.68	1.63
d/D	0.07	0.10	0.14	0.07	0.10	0.14
d/L	0.088	0.133	0.204	0.088	0.133	0.204

**Table 32** Geometric parameters of IWP cell for FE analysis

	IWP cell					
$\rho^*/\rho_s [\%]$	5	10	20	5	10	20
D [mm]	2.9	2.1	1.4	7.3	5	3.5
t [mm]	0.04	0.06	0.08	0.11	0.15	0.21
a [mm]	1.15	0.81	0.51	2.90	1.94	1.29
t/D	0.02	0.03	0.06	0.02	0.03	0.06

Mapped meshing was adopted to get good quality first order hexahedral elements. With regards to the strut-based unit cells, according to the strut diameter, the mesh size used was 0.06 mm for cells with strut diameter of 0.2 mm, and 0.16 mm for cells with strut diameter 0.5 mm, in order to have three elements along the strut cross section.

For the TAOR cell, considering the symmetries of the structure, only one sixteenth of the cell was meshed. The other portions were obtained by reflecting the mesh along the symmetry planes, as shown in Fig. 55.

**Fig. 55** Steps for the meshing of the TAOR cell

In Fig. 56 is reported a section of the TAOR cell mesh.

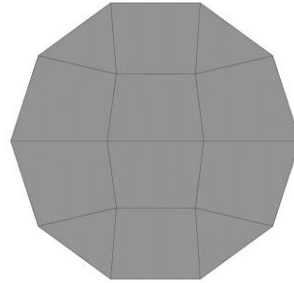


**Fig. 56** Section of the TAOR cell mapped mesh

With regard to the IWP cell, also in this case the symmetries of the structure were considered; thus, only one eighth of the cell was meshed and then reflected along symmetry planes. For all the configurations, the surface was meshed with elements of 0.15 mm size, then an element offset was applied by imposing three elements along cell thickness, as shown in Fig. 57.

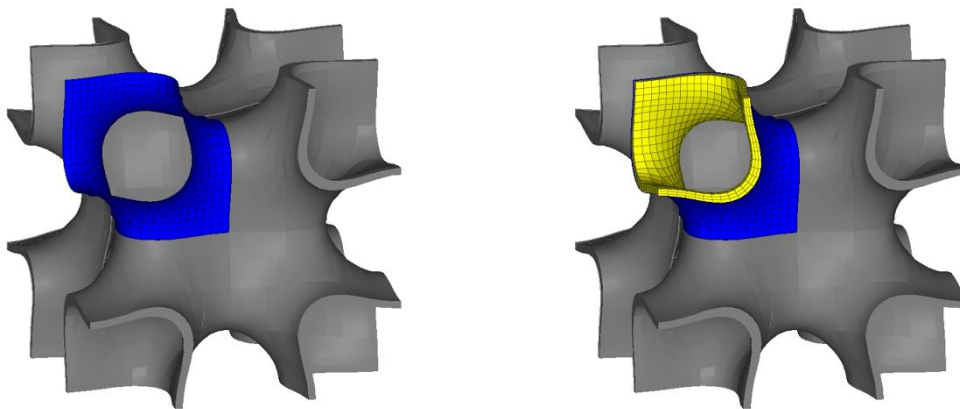


**Fig. 57** Steps for the meshing of the IWP cell

A top and a bottom plates were considered for the application of the boundary conditions. They were meshed with first order quad elements of the same dimensions of the corresponding unit cell configuration, to obtain the equivalence at the nodes, guaranteeing mesh continuity.

Boundary conditions were applied to replicate the compression tests. An imposed velocity of 1 mm/min along y axis was imposed on the superior plate and the inferior plate was

constrained in all degrees of freedom as shown in Fig. 58. In addition, on the superior plate was applied a further constraint to avoid translation in x and z directions, and rotation in all directions.

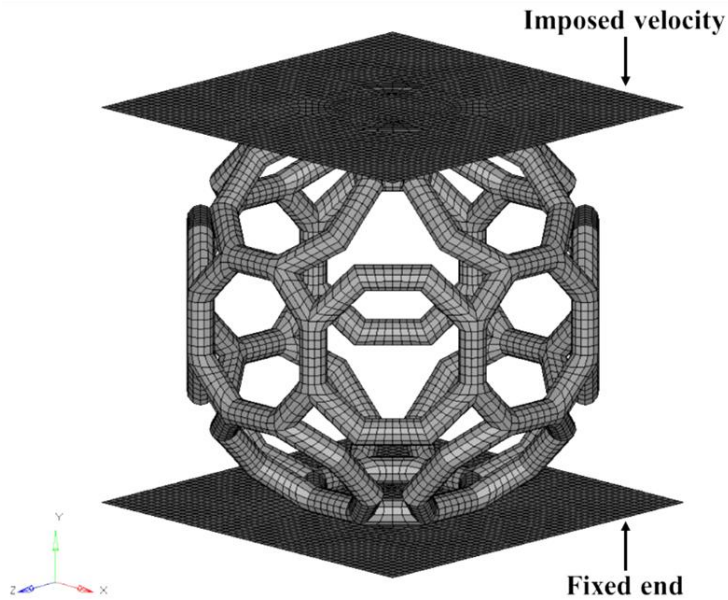


**Fig. 58** FE model boundary conditions of the non-linear analysis of the single unit cells

The results of the FE analysis are shown in Fig. 59, Fig. 60 and Fig. 61. For an easier understanding, in the ID of the TAOR and the Kelvin cells is included the relative density, while for the G7 and IWP cells, the strut diameter values. For a comparison of the compressive behaviour and the failure modes of different cell types and sizes, the results are reported for different levels of displacement considered as percentage value of the cell diameters. The FE model results are expressed in terms of true stress, thus the real ultimate stress value of the Ti6Al4V alloy equal to 1107 MPa was considered for the representation of the Von Mises stresses.

The deformation modes of the unit cells are consistent with the experimental results; thus, the reliability of the FE model is verified, and it can be applied to lattice structures.

For the strut-based unit cells, the failure mode appears at the nodes of the structure, where stresses intensification occurs.

In the TAOR cell it can be observed that the first and last layer are deformed before the central part since their deformation mechanisms is dominated by nodes failure. The failure of vertical struts is dominated by buckling, which causes the final collapse of the cell. Such failure mode allows to design a programmed adsorbing energy system. In the Kelvin and in G7 cells, the absence of the vertical strut does not allow this behaviour.

TAOR\_5% shows a different behaviour respect to other configuration at a displacement of 25%, since the upper part is deformed before the lower end; furthermore, rotation along z axis and buckling due to the lower aspect ratio can be observed. When the displacement is 50%, a symmetric deformation for all the configurations can be observed. At a displacement of 75%, the central part of the unit cells collapses and the TAOR\_20% shows lower stress values than other configurations.

For the Kelvin cell with relative densities 5% and 20%, symmetric deformation for a displacement of 25% appears, while at a displacement of 50% the lower part collapse before the top end due to the fracture of the nodes at the contact with the bottom plate where the fixed constraint is applied. Kelvin\_10% shows different behaviour, since the upper part collapse before the lower end at a displacement of 25%, while at displacement of 50% the deformation is symmetric. For a displacement of 75% the deformation behaviour is symmetric for all the configurations with stress intensifications at the nodes of the structures.

In the G7 unit cell, for all the configurations, the collapse mode of the vertical struts is dominated by buckling. For the G7 cells with relative density 20%, at a displacement of 25% a symmetric deformation appears. For a displacement of 50%, the inferior part collapses before the superior one. For the G7 cells with relative density 10%, at a displacement of 25%, a symmetric deformation appears in the G7\_2.1mm cell, while a collapse mode dominated by buckling of the inclined struts appears in the G7\_5mm cell. At a displacement of 50%, the G7\_2.1mm cell presents a symmetric deformation, while the collapse of the structure occurs in the G7\_5mm cell. For relative densities of 10% and 20%, all the analysed configurations do not reach a displacement of 75%, due to the collapse of the structures. The G7 cells with relative density 5%, because of the aspect ratio low value, present buckling dominated collapse mode also in the inclined struts; this behaviour is observable at displacements of 25% and 50%, with symmetric deformation. At a displacement of 75%, the failure of the vertical struts occurs, and the stress values decrease. G7\_2.9mm cell presents peak stress values at the cross nodes, while G7\_7.3mm cell, with the same 20% relative density, presents evenly distributed stress values in the whole structure.

In the IWP unit cell, for all the configurations, the collapse mode is gradual and dominated by wall crushing. For IWP cells with relative density 5%, the central portion of the structures collapse first, and the deformation behaviour is symmetric. Both cell sizes analysed do not reach a displacement of 75% due to the collapse of the structure. For IWP

cells with relative density 10% and 20%, at displacements of 25% and 50% the deformation behaviour is asymmetric for all the configurations analysed. In the IWP\_2.1mm and IWP\_3.5mm, the superior part collapse before the inferior one, while in the IWP\_1.4mm and IWP\_5mm the inferior part collapses first. The configurations with higher size values do not reach a displacement of the 75% because of the collapse of the structure, while the IWP\_1.4 and IWP\_2.1 cells reach a displacement of 75% following the same deformation behaviour described for displacements of 25% and 50%.

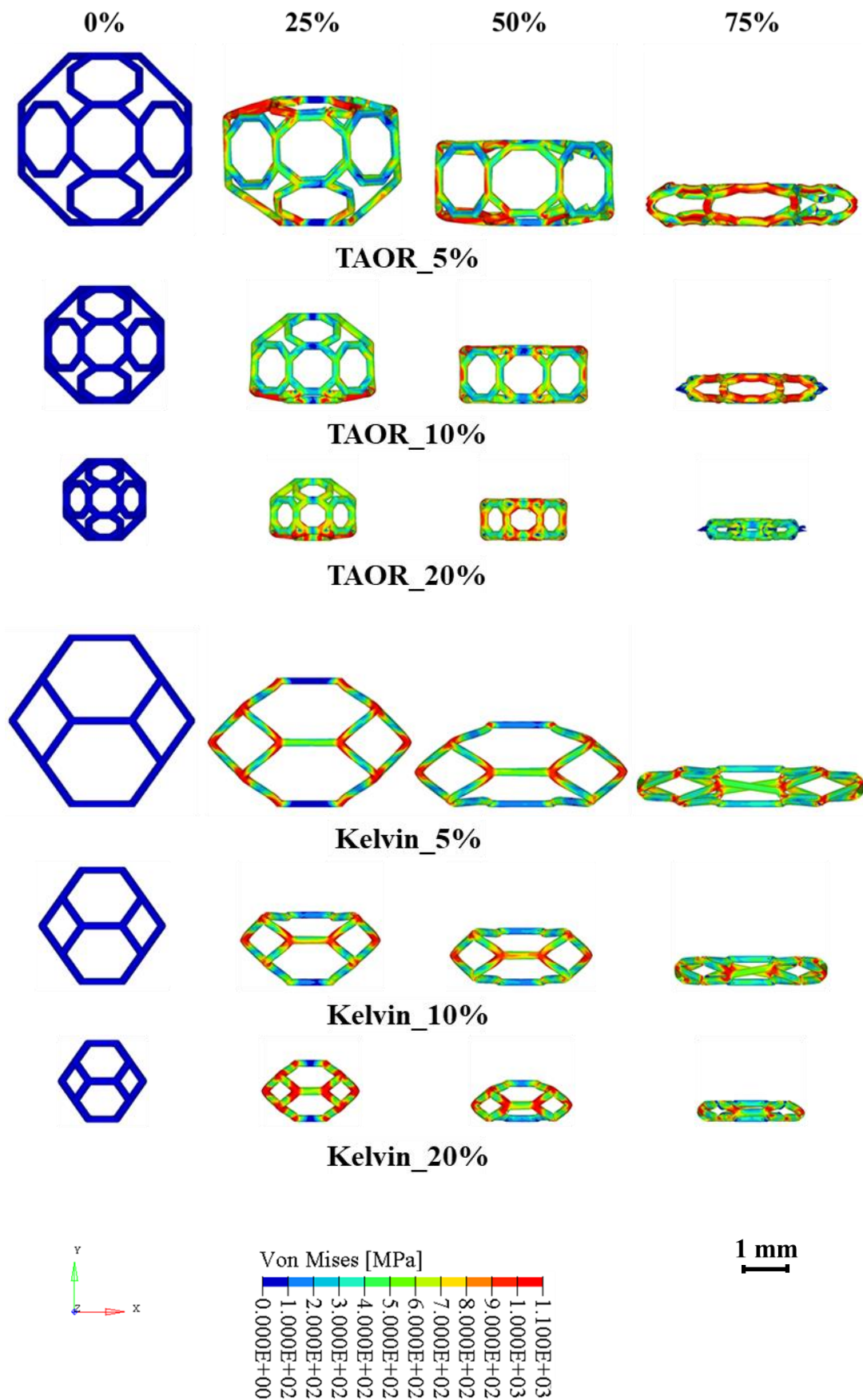


**Fig. 59** TAOR cell and Kelvin cell FEA analysis results

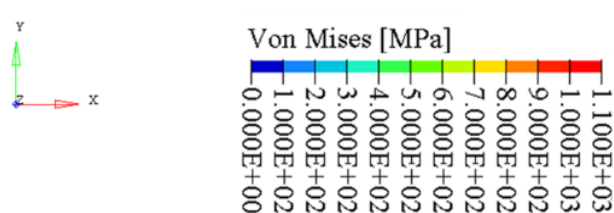
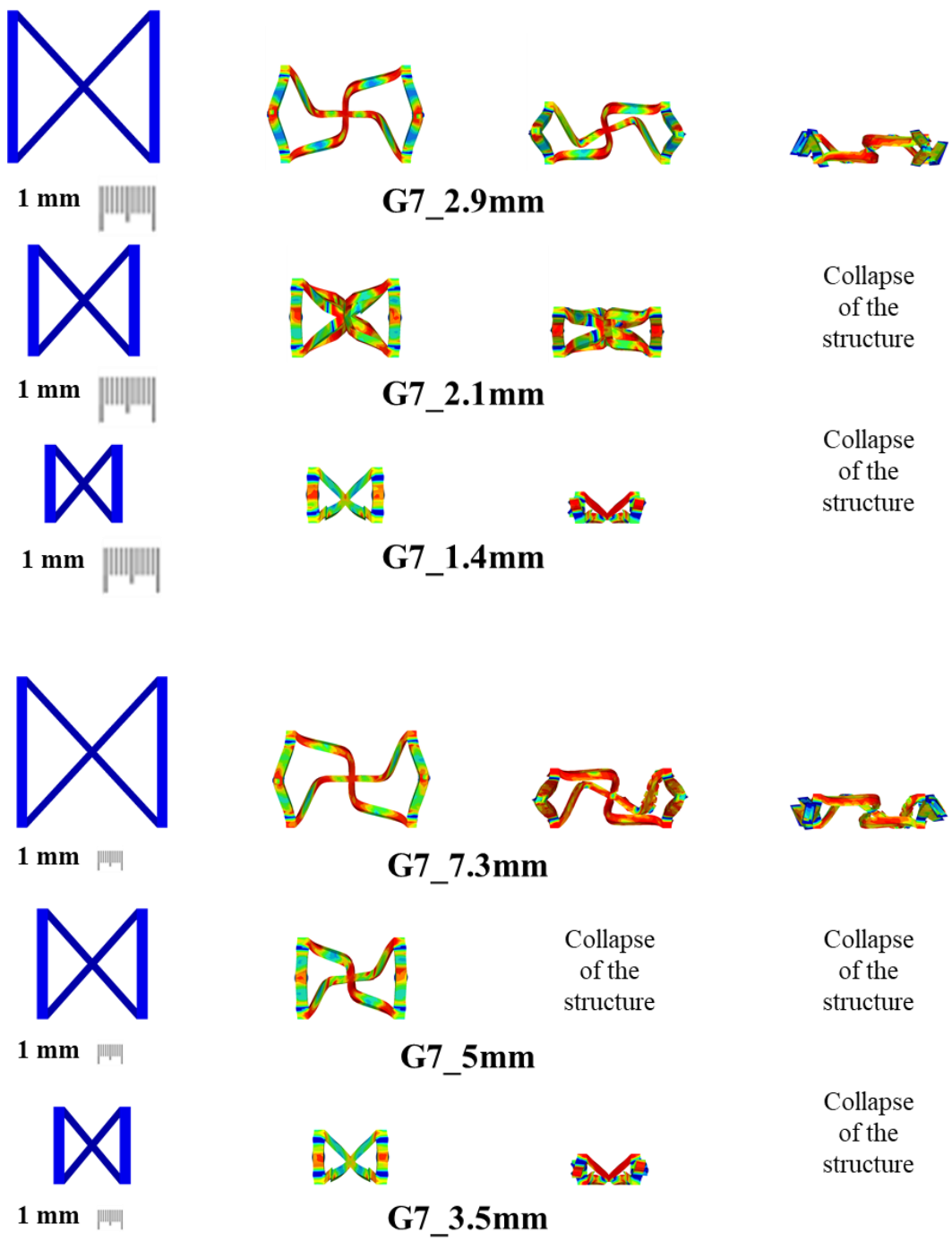
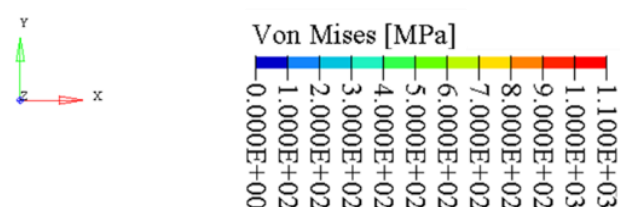
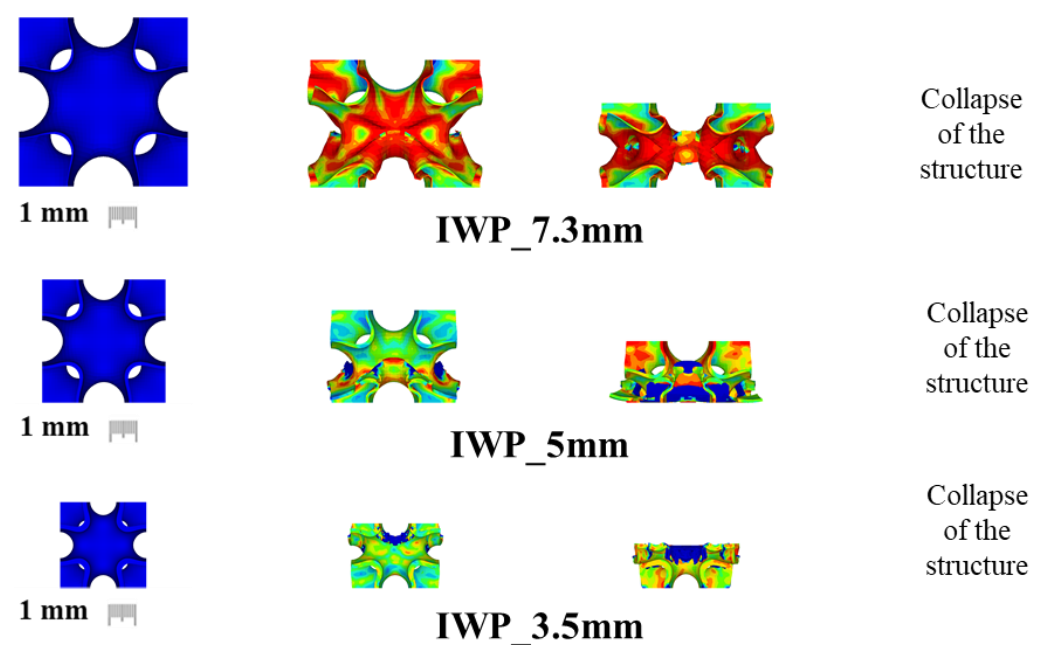
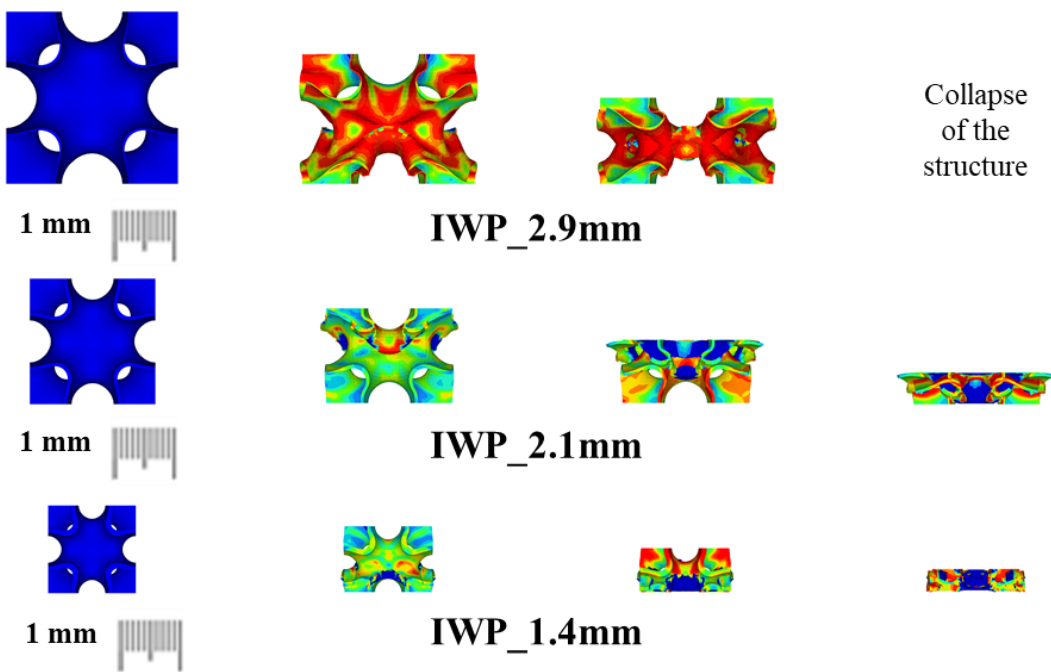


Fig. 60 G7 cell FE analysis results



**Fig. 61** IWP cell FEA analysis results

### 3.2.4. Finite element analysis of the lattice structure

The JC material model described in section 3.2.2. was also employed to develop a FE model of the lattice structure.

The aim of the present FE analysis is to evaluate the mechanical properties of the TAOR lattice and compare the results with those obtained in the experimental tests.

Four levels of relative density were considered: 5%, 10%, 15%, 20%, evaluated with the first method proposed in section 2.2.. Cubic specimens with 8 and 27 unit cells were considered, in order to have respectively 2 and 3 unit cells on each side of the specimen. Unit cells geometric parameters are summarised in Table 33. The geometric parameters refer to Fig. 30.

**Table 33** Geometric parameters of the TAOR cell for the FE analysis

	<b>TAOR cell</b>			
$\rho^*/\rho_s$ [%]	5	10	15	20
D [mm]	3	3	3	3
d [mm]	0.16	0.2	0.24	0.28
L [mm]	0.48	0.48	0.48	0.48
a [mm]	1.05	1.03	0.89	0.84
d/D	0.053	0.067	0.080	0.093
d/L	0.33	0.42	0.50	0.58

Mapped meshing was adopted to get good quality first order hexahedral elements, with the same method explained in section 3.2.3.. The element size was changed based on the strut diameter d, in order to obtain the mesh depicted in Fig. 56 of section 3.2.3..

An imposed velocity of 1 mm/min along y axis was imposed on the superior plate and the inferior plate was constrained in all degrees of freedom as shown in Fig. 62.

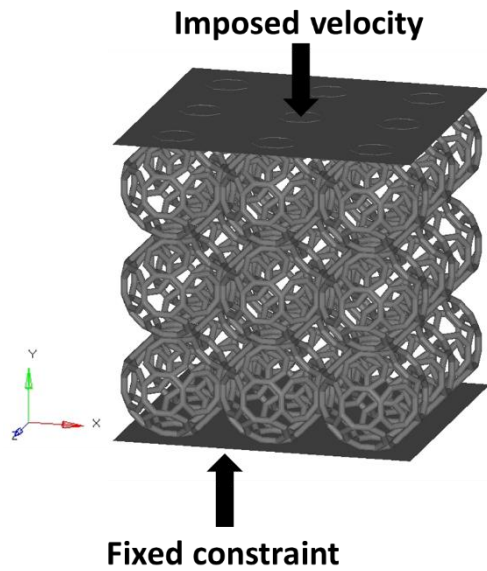


**Fig. 62** FE model boundary conditions of the non-linear analysis of the TAOR specimens

The results of the FE analysis are shown in Fig. 63. Where stress was obtained as the ratio between the load and the cross section of lattice specimens, whereas strain was evaluated from the overall displacement divided by the initial height of the specimen. In the specimen's name, the number next to the percentage relative density indicates the number of cells on each edge of the specimen.

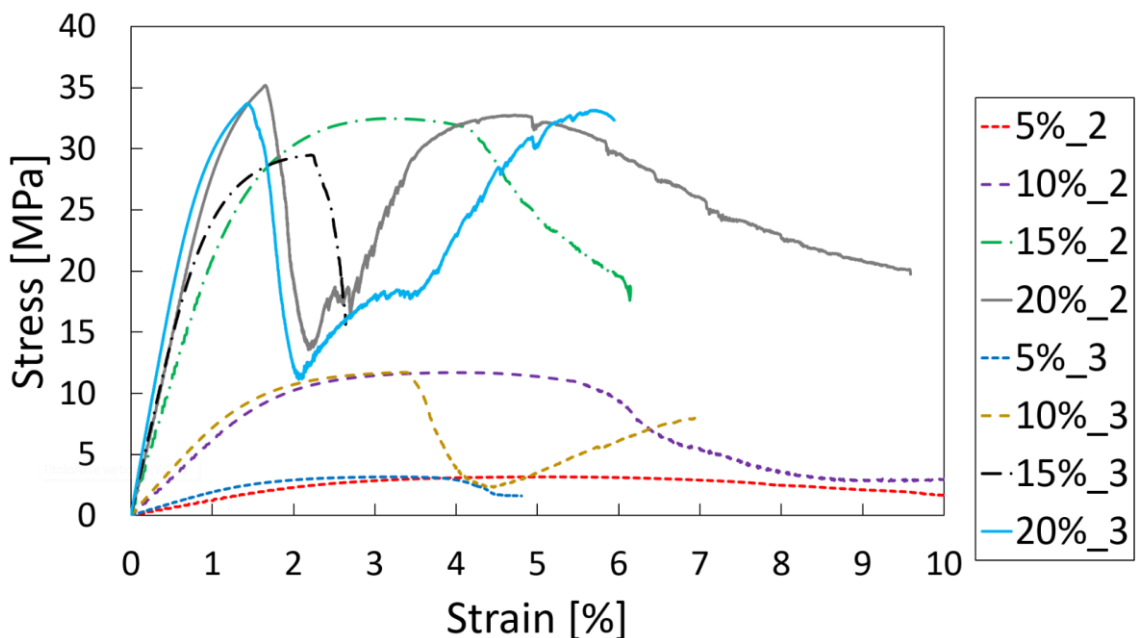


**Fig. 63** Stress-strain curves of the non-linear FE analysis of the TAOR specimens

The FE analysis results are summarised in Table 34. A direct comparison with the results of the compressive tests (section 3.1.3.) was not possible since the morphological analysis (section 3.1.2.) showed discrepancies between the designed and the actual relative densities. Gibson-Ashby model allows the comparison of the mechanical properties of lattice structures for a given relative density; thus, the comparison was performed considering the elastic modulus and the compressive strength of the TAOR lattices obtained through the application of the Gibson-Ashby model (section 3.1.4.) on the designed relative densities.

**Table 34** FE analysis results of the non-linear model of the TAOR specimens

	E [MPa]	E variation [%]	$\sigma_m$ [MPa]	$\sigma_m$ variation [%]
5%_2	102.9	6.17	3.17	-42.15
10%_2	342.5	-26.55	11.69	-27.07
15%_2	1222.9	4.63	32.48	8.12
20%_2	1635.4	-27.10	35.19	-24.97
5%_3	110.4	13.91	3.17	-42.15
10%_3	419.7	-9.99	11.72	-26.89
15%_3	1624.7	39.00	29.50	-1.80
20%_3	2034.3	-9.23	33.70	-28.14
5%_Gibson-Ashby	96.92	/	5.48	/
10%_Gibson-Ashby	466.30	/	16.03	/
15%_Gibson-Ashby	1168.84	/	30.04	/
20%_Gibson.Ashby	2243.46	/	46.90	/

As expected, the mechanical properties increase at the increase of the relative density. Both FE models with 2 or 3 unit cells per edge present comparable results for a given relative density, in terms of curves trend and mechanical properties. With regard to the elastic modulus, the models with 5% and 15% relative densities underestimate the value of the Gibson-Ashby model, while models with relative densities 10% and 20% overestimate it. With regard to the compressive strength, all the models, except for the 15%\_2 specimen, underestimate the value of the Gibson-Ashby model. The differences

observed from the comparison of the results of the FE models and the value obtained from the application of the Gibson-Ashby model can be explained considering the published literature, Mazur et al. [77] evaluated the effect of the number of cells on the mechanical properties of the lattice structure. They compared structures with 3, 5, 7 and 10 unit cells for each specimen edge, showing that the minimum cell number for the convergence of the results is 5. Due to computational costs, it was not possible in the present research, developing models with a higher number of unit cells. Specimens with 2 and 3 cells for each specimen edge were chosen considering the results of Peng et al. [15]. They developed a FE model with the use of JC material model, on specimens with 2 or 3 cells per edge, showing comparable results, as verified in the present study. Due to these reasons and taking into account the double validation performed in section 3.2.2. and the results of the FE analysis of the single unit cell presented in section 3.2.3., the developed FE model is considered a reliable support tool for the analysis of the mechanical behaviour of lattice materials. However, an extensive experimental analysis is necessary to exactly evaluate the mechanical properties of a lattice material.

## Chapter 4

# MECHANICAL ANALYSIS OF POROUS DEVICES

In this chapter, a case study regarding the application of lattice structures in intervertebral body fusion devices, made of Ti6Al4V ELI alloy and produced by EBM, is presented.

### 4.1. SUBSIDENCE OF INTERVERTEBRAL BODY FUSION DEVICES

Degenerative disc diseases are a serious health problem which may result in mechanical back pain, reduced mobility and poor quality of life. Lumbar intervertebral body fusion devices are widely used in the treatment of lumbar diseases [133]. Different surgical options for interbody fusion of the lumbar spine have been developed, as shown in Fig. 64, including: posterior lumbar interbody fusion (PLIF) [134], oblique lumbar interbody fusion/anterior to psoas (OLIF/ATP) [135], lateral lumbar interbody fusion (LLIF) [136], anterior lumbar interbody fusion (ALIF) [137], extreme lateral interbody fusion (XLIF) [137], transforaminal lumbar interbody fusion (TLIF) [138], minimally invasive transforaminal lumbar interbody fusion (MI-TLIF) [139].

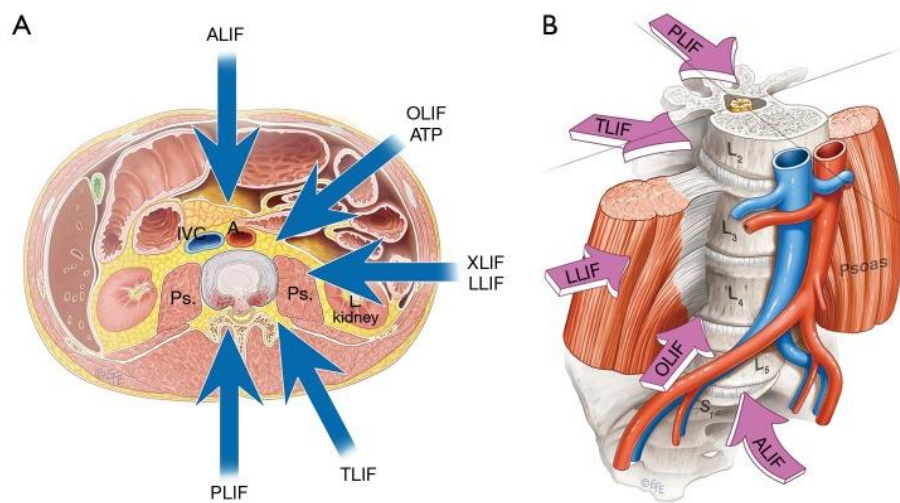


**Fig. 64** Surgical approaches to the lumbar spine for interbody fusion techniques

The advent of minimally invasive surgery (MIS) techniques provided advantages of decreased soft tissue dissection, lower blood loss, and decreased post-operative pain [140]. However, there is no clear definitive evidence for one approach being superior to another in terms of fusion or clinical outcomes [133].

In this research, the risk of subsidence was analysed for two different types of LLIF devices. The subsidence of the implant [141], [142] represents a serious clinical issue and one of the post-surgical complications of such devices during the healing process, and it can lead to the implant failure and to the collapse of the intervertebral body [143], [144]. The risk factors associated with the subsidence of a titanium cage, such as age, sex, operation level, device geometry, alignment in the intervertebral bodies and global Hounsfield Units, were analysed to facilitate an optimal management of such a condition [145]. The role of the intervertebral discs, which ensure mechanical stability and prevent the implant subsidence, was investigated by determining their influence on the vertebral mechanical properties during axial compression tests [146] or by carrying out a finite element sensitivity study [147]. Many studies aim to predict the risk of subsidence for the intervertebral body fusion devices by means of finite element (FE) analysis [148] or statistical methods based on computed tomography (CT) scans [149]. FE analyses were carried out by applying different compressive intervertebral loads corresponding to some activities for investigating their influence on the generation of endplate stresses that increase the risk of subsidence [150]. Numerical analysis was also applied to assess the risk of subsidence by evaluating the stresses at the interface between cage and vertebrae as functions of cage height and cage placement strategy: oblique asymmetric or anterior symmetric [151]. Other researchers calculated the contact area between implants and bone and evaluated the subsidence by modifying their angular mismatch [152], or by calculating the rate of subsidence on upper and lower endplates of vertebral bodies using CT scans [153]. Several studies tried to improve the subsidence behaviour of the implants by optimizing their designs. Shape optimization was performed by combining results of the experimental tests and CT scans, to identify the parts to be improved [154]. In another study, shape optimization was performed by means of FE analysis, developing a simulation based on genetic algorithm [155].

Some studies applied the ASTM F2267 standard testing method to establish a range of mechanical properties that improve the subsidence behaviour [156]. The correlation between cage size and subsidence was assessed by testing cages between two polyurethane foam blocks and the resistance achievable with larger cages was quantified.

Yuan et al. [157] compared the subsidence resistance of implants of different sizes under compression loading. In another study, Chong et al. [158] investigated three different sizes of lumbar devices under axial compression and rotation loads.

In the present study, the first implant is characterized by the presence of both porous and solid structures; the second implant has only a solid structure (not filled), with the same shape of the first case. Moreover, the first case includes a lattice core and lattice endplates at the interfaces between the implant and the intervertebral bodies. The contact pressure at the interface between implants and intervertebral bodies was calculated by means of experimental tests and FE models. Particular attention was paid to the differences in the mechanical behaviour of the two implants. In another research paper, Lim et al. [159] studied cages with porous structure instead of solid one, concluding that the risk of subsidence can be reduced by decreasing the mismatch between the elastic moduli of the implant and vertebral bodies. Zhang et al. [160] compared the biomechanical performance of porous and solid TLIF devices to verify the effects of cages with different porosities, their results indicated that cages with a porosity between 65% and 80% showed advantages in cage stress and endplate stress.

The device object of the present research is characterised by the addition of a porous part embedded within a skeletal device made of the same bulk material. The reason for such a design choice was to evaluate potential improvements in the mechanical performance of the implants. In more detail, this research aims to verify the improvement of subsidence performance resulting from the introduction of lattice structures, which ensure a smoother contact pressure at the vertebrae-cage interfaces without modifying the solid structure, which guarantees the mechanical stability of the implant.

## 4.2. DESCRIPTION OF THE DEVICES

The investigated devices were two lumbar cages made of Ti-6Al-4V ELI (Grade 23) alloy and produced via EBM process. The Arcam Q10 3D printer was used to manufacture the devices. The Ti6Al4V ELI titanium alloy contained reduced levels of oxygen, nitrogen, carbon and iron and its particle size distribution was between 45 and 100 µm. The partially porous (PP) device included an external solid shell, a porous microlattice core and an upper and a lower endplate both with microlattice structure (Fig. 65a).



**Fig. 65** Devices object of the study: (a) with porous microlattice core; (b) without porous microlattice core

The selected unit cell of all the microlattice parts was the rhombic dodecahedron (RD). The unit cell size was 3 mm for the core and 2 mm for the endplates. Parent material and RD lattice were previously tested in the laboratory of the Department of Engineering at the University of Messina [105]. The skeletal (S) device had the same external shell of the first case, but it didn't include any microlattice structure (Fig. 65b). The nominal dimensions of the implant were the same in both cases: 48 mm × 21 mm × 9 mm, where the height was obtained as the mean value between the anterior height (11 mm) and the posterior one (7 mm), while the thickness of the external shell had a constant value of 2 mm. The average value of surface roughness ( $S_a$ ) was 20.7  $\mu\text{m}$  and was measured by a confocal microscope (Leica DCM 3D, Leica Microsystems, Germany), as shown in Fig. 66. Statistical analyses were made on an area of  $0.64 \times 1.54 \text{ mm}^2$  belonging to the cage, by means of LeicaMap 6.2 software. Such a scan was obtained by an extended topography with an EPI 20X-L objective in LeicaScan DCM 3D software. The z-scan covered a height of 600  $\mu\text{m}$  with a z-step of 10  $\mu\text{m}$ .

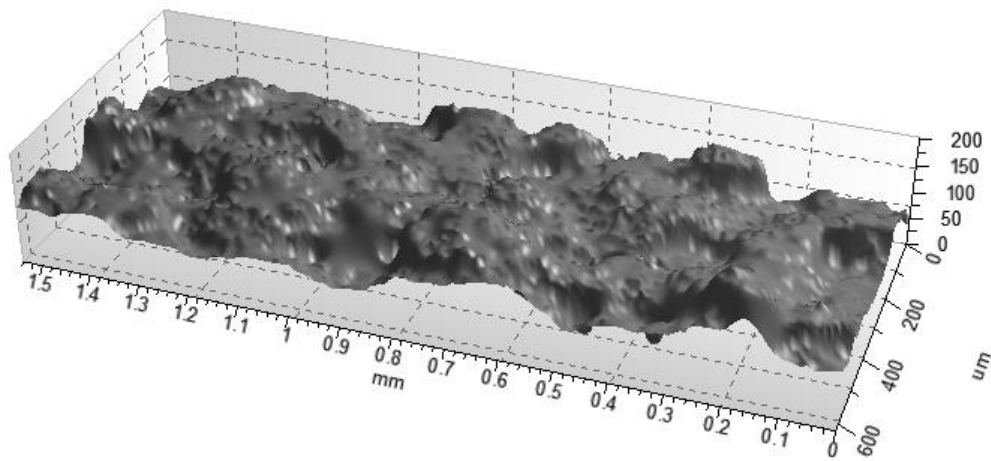


**Fig. 66** Surface analysis of the device

The data extracted from the surface, according to ISO25178 are reported in Table 35:

**Table 35** Surface analysis results

Name	Value	Unit
$S_q$	25.91	μm
$S_{sk}$	0.22	
$S_{ku}$	3.72	
$S_p$	104.5	μm
$S_v$	103.7	μm
$S_z$	208.2	μm
$S_a$	20.72	μm

where:  $S_q$  is the root mean square height of the surface,  $S_{sk}$  is the skewness of height distribution,  $S_{ku}$  is the kurtosis of height distribution,  $S_p$  is the maximum height of peaks,  $S_v$  is the maximum height of valleys,  $S_z$  is the maximum height of the surface and  $S_a$  is the arithmetical mean height of the surface. The implants with high surface roughness improve osseointegration [161]. Thus, no additional treatment was performed after the EBM process. The devices were designed to be inserted by LLIF approach. Lateral hollows allow the device fixation to the vertebral bodies during the implantation.

### 4.3. EXPERIMENTAL INVESTIGATIONS

#### 4.3.1. Experimental set-up

Static compression tests were performed according to ASTM F2267 standard to analyse the subsidence of the implants. The test standard specifies the materials and methods for the axial compressive testing of the intervertebral body fusion devices. The tests aim to characterize the mechanical behaviour of a device during the subsidence into the intervertebral bodies.

The compression tests were carried out on an Italsigma FPF 25 universal testing machine equipped with a HBM U10M 12.5 kN load cell, at a constant speed of 0.1 mm/s and by applying a preload of 0.45 kN. The experimental tests were performed on both PP and S devices, with the aim of verifying the different behaviour of the implanted cage with and without microlattice structure. For evaluating the subsidence behaviour, the devices were positioned between two polyurethane grade 15 test blocks, having dimensions 60 mm × 60 mm × 40 mm. The use of polyurethane foam was in conformity to ASTM F1839 standard, and it was intended to provide a consistent and uniform material having mechanical properties similar to human bone. The surface of the foam was machined with the same shape of the implant for a perfect matching at the interface between polyurethane and device, as shown in Fig. 67.

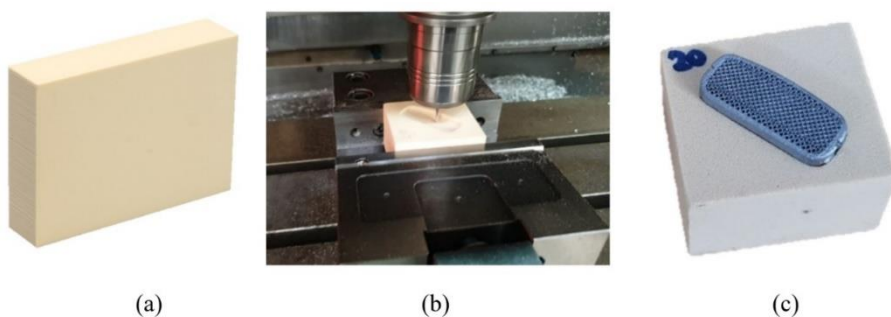


**Fig. 67** Tooling of Polyurethane foam blocks: (a) raw blocks; (b) CNC machining; (c) final result with a perfect fit of the device into the block

As shown in Fig. 68, the average height between the blocks including the cage was 4 mm. Therefore, this value was considered as the maximum crosshead displacement during the tests, which corresponded to the maximum subsidence.

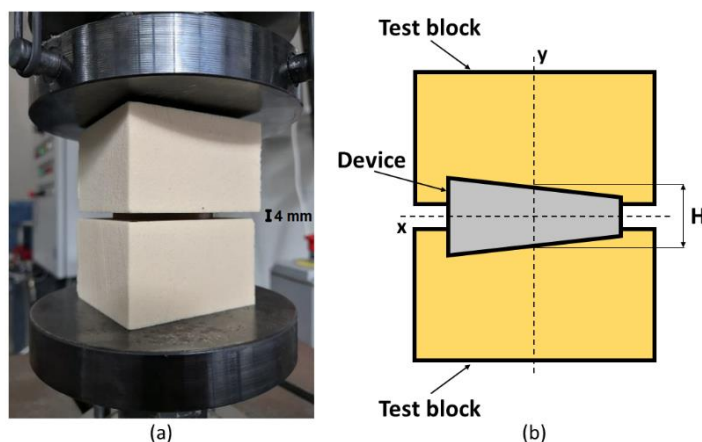


**Fig. 68** Polyurethane foam blocks with the cage implanted: (a) compression tests, (b) intradiscal height

The standard test procedure suggested a 10 mm intradiscal height  $H$  for lumbar implants at the centre of the device, along the  $y$ -axis (Fig. 68b). For the investigated cases, the footprints of the devices in the polyurethane blocks were deepened to make the assembly more stable and prevent sharing motion of the fixtures. Therefore, 4 mm height was the maximum value obtainable for the implants object of the study.

Visual inspection was carried out to evaluate the damage occurred during the compression tests and the deformation behaviour of the polyurethane foam at the interface with both devices.

Moreover, CT analysis was performed with a Y.CT Vario (YXLON International GmbH, Hamburg, Germany) to validate the FE models by comparing the displacement of the polyurethane foam obtained from the experimental tests and FE analyses. CT scans were obtained with a focal spot size of 250  $\mu\text{m}$  (smallest available), 190 kV voltage and 1.1 mA current and a 1 mm thick Cu filter between the tube and the specimen. The reconstruction was performed with a voxel resolution of  $46.4 \mu\text{m} \times 46.4 \mu\text{m} \times 46.4 \mu\text{m}$  and a tomogram pixel resolution of  $2048 \times 2048$ . The dataset was processed by VGStudio Max 2.0 (Volume Graphics GmbH, Heidelberg, Germany) and the displacement was measured by the same software.

### 4.3.2. Experimental investigations results

The compression tests were performed on both PP and S devices (with two repetitions for each type) to analyse the implant subsidence. The load-displacement curves obtained from the compression tests are reported in Fig. 69.

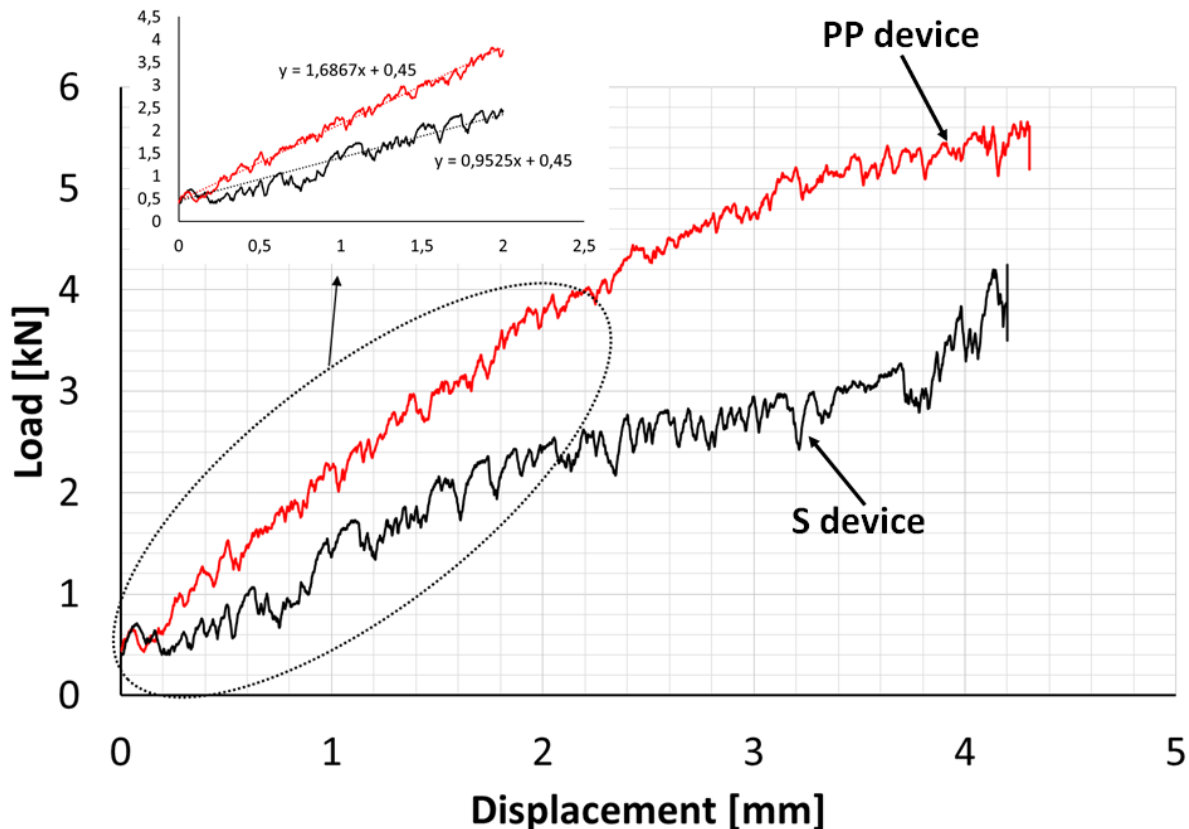


**Fig. 69** Load-displacement curves for PP device and S device

The ASTM F2267 standard test method establishes guidelines to measure test blocks deformation and to evaluate the subsidence of the intervertebral devices. It doesn't describe a method to evaluate their mechanical properties. Hence, in the standard test, the loads were small if compared to the mechanical strength of the device. The tests were stopped when the functional failure of the polyurethane foam occurred.

Since the tests on the PP device showed a good repeatability, the load-displacement curve reported in Fig. 69 is the average one. The noise that characterised the curve for PP device was likely the result of foam pores local collapse. The load trend for both devices was similar, but for the PP case the absolute load values were higher. The maximum load

achieved by the PP device was equal to 5.6 kN, corresponding to a displacement of 4.3 mm, while S device had a maximum load of 4 kN at a displacement of 4.2 mm. Thus, the microlattice structure improved the subsidence behaviour of the cage, by increasing the load achieved at a certain subsidence value. The FE models were validated by performing non-linear plastic analyses. The maximum load of 4 kN for the S device was considered as the reference value. This value was also used for the validation of the PP device model, yielding a displacement of 2.25 mm. The stiffness of the device-polyurethane foam system, and the energy absorbed during test, were calculated from the load-displacement curve. The stiffness was obtained from linear regression of the elastic curve (Fig. 69): the PP device has significantly higher stiffness compared to the S device (Table 36). Higher stiffness values reduce the risk of subsidence, according to the current literature [162]. The absorbed elastic energy, calculated for the elastic part of the curve, and the total energy absorbed up to the maximum subsidence load were also obtained: PP device showed higher values than S device; the energy ratio was similar for the elastic energy and the total energy (Table 36).

**Table 36** Device-foam stiffness and energy absorbed during experimental tests

	Stiffness [N/mm]	Total Energy [J]	Elastic energy [J]
<b>PP device</b>	1686,7	15,46	4,28
<b>S device</b>	952,5	9,07	2,72
<b>Ratio</b>	1,77	1,7	1,58

The visual testing highlighted that the device including microlattice guaranteed a better stress distribution at the interface between cage and blocks, as shown in Fig. 70.

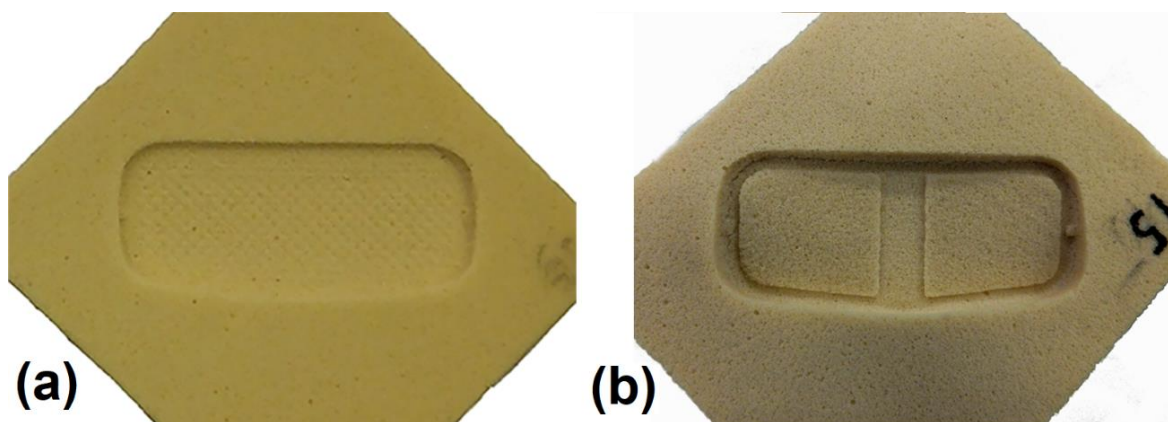


**Fig. 70** Stress distribution at the interface between polyurethane foam blocks and: (a) PP device, (b) S device

The presence of the microlattice structure in the PP device produced a smooth stress distribution over the entire contact surface. Higher stress values were observed in the front zone of the contact surface, where higher displacement occurred. Nevertheless, these values didn't result in higher load than the admissible one. For the S device, the contact at the interface was provided by the shell of the implant. A more marked print was present all over the edge of the contact surface and in the central zone, due to overload. In the central zone, the overload could lead at the implant failure because the cortical bone is less thick than in the outer part of the vertebra; thus, it is able to sustain lower loads in this part.

#### 4.4. FINITE ELEMENT ANALYSIS OF THE RISK OF SUBSIDENCE

##### 4.4.1. Finite element models

The FE analyses were performed by using Altair HyperWorks® 14.0 (Altair Engineering, MI) package software. Hypermesh® software was used for mesh generation and boundary conditions definitions while Optistruct® software was used as implicit solver. The non-linear quasi-static FE model aimed to replicate the boundary conditions of the experimental tests but with the application of physiological loads. The first step involved FE structural analyses of both devices. Since the PP device included three different components, as described in section 2.1, a tied contact was defined at the interfaces between the three different parts of the device to guarantee the actual structural continuity of the device produced via EBM. Tied contact produces rigid bond and prevents relative

movements of the components. A mesh sensitivity test was conducted and element sizes from 0.5 mm to 0.1 mm analysed. Principal stresses in tension and compression were evaluated and the prediction errors are reported in Table 37 and Table 38, where the percentage difference is calculated in relation to the cage with element size 0.2 mm:

**Table 37** Mesh sensitivity test of the device: compression stresses

Element size [mm]	Bulk material		Bulk material		Lattice 2 mm	Lattice 2 mm	Lattice 3mm	Lattice 3 mm
	stress [MPa]	variation [%]	stress [MPa]	variation [%]	stress [MPa]	variation [%]	stress [MPa]	variation [%]
	0.5	-10.94	-36.83	-0.39	-46.57	-3.05x10 <sup>-2</sup>	-24.50	
0.4	-14.74	-14.89	-0.48	-34.25	-3.30x10 <sup>-2</sup>	-18.32		
0.3	-15.06	-13.05	-0.58	-20.55	-3.72x10 <sup>-2</sup>	-7.92		
0.2	-17.32	/	-0.73	/	-4.04x10 <sup>-2</sup>	/		

**Table 38** Mesh sensitivity test of the device: tension stresses

Element size [mm]	Bulk material		Bulk material		Lattice 2 mm stress [MPa]	Lattice 2 mm variation	Lattice 3mm stress [MPa]	Lattice 3 mm variation
	stress [MPa]	variation [%]	stress [MPa]	variation [%]	stress [MPa]	variation [%]	stress [MPa]	variation [%]
	0.5	55.81	-18.68	0.78	-17.02	5.54x10 <sup>-2</sup>	-92.89	
0.4	56.25	-18.04	0.81	-13.83	0.48	-36.84		
0.3	63.56	-7.39	0.83	-11.70	0.59	-22.37		
0.2	68.63	/	0.94	/	0.76	/		

Thus, all the components were discretized using 0.2 mm first order tetrahedral elements. It was not possible use a finer mesh due the impossibility to run the analysis in the workstation. The following boundary conditions were applied: a compressive load of 1 kN, equal to twice the physiological one [163], to verify the mechanical strength of the cage, and fixed constraints in all directions. The material properties of the device were obtained from a previous study, in which experimental tests on both porous and bulk materials were carried out [105]. The microlattice structure was modelled as an equivalent isotropic material having the mechanical properties of the porous Ti-6Al-4V ELI. The stress distribution and values were similar to the ones obtained with the RD unit cell. This assumption was considered acceptable by the authors because the stress distribution in the unit cells doesn't influence the subsidence phenomenon, which depends only by the contact at the interface between device and vertebra.

In the second step, the FE analyses of the polyurethane foam blocks with the implanted devices were validated. Two different models were developed, one with the PP cage and the other with the S cage. For both cases, the same method was applied to model the blocks, with the same geometry of that used in the compression tests. A mesh sensitivity test was performed to evaluate the optimal mesh size for the polyurethane blocks at the interface with the device. Mesh transition was considered as the optimal choice. The analysis was conducted, pressure values in tension and compression evaluated and the prediction errors are reported in Table 39.

**Table 39** Mesh sensitivity test of the polyurethane blocks

Element size [mm]	Pressure tension [MPa]	Pressure tension % difference	Pressure compression [MPa]	Pressure compression % difference
0.4	34.7	-61.64	-6.73	-79.79
0.8	13.31		-1.36	

First order tetrahedral elements with higher density (0.4 mm size) were generated in the contact region between the foam and the device, while coarser mesh (4 mm element size)

was used in the further zone (Fig. 71). It was not possible use a finer mesh due the impossibility to run the analysis in the workstation. Other element sizes were not considered, since for this type of analysis it is recommended a ratio of 1:1, 1:2, 1:4 between the master and slave elements. The contact interface between the device and the polyurethane foam was modelled by applying a static Coulomb friction coefficient equal to 0.4 [164]–[166]. The polyurethane foam was modelled as an isotropic material [167]; a summary of the material properties applied for the devices and the foam is reported in Table 40.

**Table 40** FE model material properties

	Ti6Al4V ELI Bulk	Ti6Al4V ELI RD_2mm	Ti6Al4V ELI RD_3mm	Polyurethane Foam
<b>Young's Modulus [GPa]</b>	115	1.088	0.156	0.123
<b>Poisson's Ratio</b>	0.33	0.33	0.33	0.3
<b>Density [kg/m<sup>3</sup>]</b>	4430	1020	550	240.3

The boundary conditions were applied to reproduce the experimental test conditions, as shown in Fig. 71, where magenta part is a fixed constraint in all directions, while red arrows represent a compressive load of 4 kN.

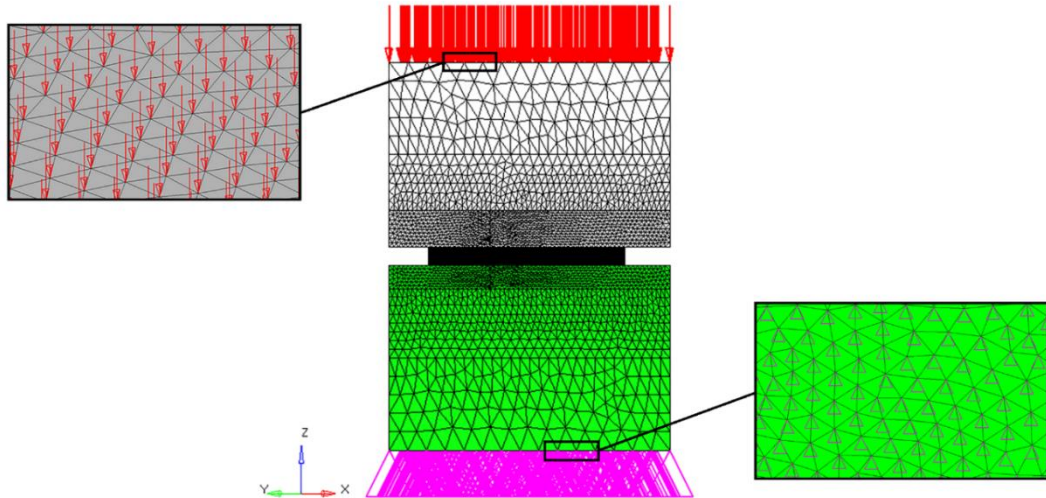


**Fig. 71** Boundary conditions of the FE subsidence analysis

The FE analyses of both devices were validated by comparing the displacement obtained from FE simulations and from compression tests at a load of 4 kN, as well as by measuring, in the CT scans, the footprint left by the device into the PU blocks.

Finally, the condition referred to a person in stance position was simulated by applying a compressive physiological load of 0.5 kN [163].

#### 4.4.2. Finite element analysis results

The structural analyses of the devices were carried out and the principal stresses for both devices subjected to a compressive load of 1 kN were evaluated. The results were compared to those obtained from a previous study for a device with similar geometry, that is designed using the same theoretical approach [86]. The stress values were smaller than the yield strength of the Ti-6Al-4V ELI alloy, both in the solid structure [168] and in the porous structure [11], [105]. Thus, no overload nor plastic behaviour of the material were detected.

The displacement values were compared to those obtained in the experimental tests under a compressive load of 4 kN for validating the FE models of the polyurethane foam blocks with the implanted devices. The highest displacement values were detected in the front contact area. This behaviour was confirmed by both the compression tests and the FE structural analyses. From CT inspection, it was observed that the deformed shape obtained from FE analyses was in good agreement with that obtained during the experimental tests as shown in Fig. 72.

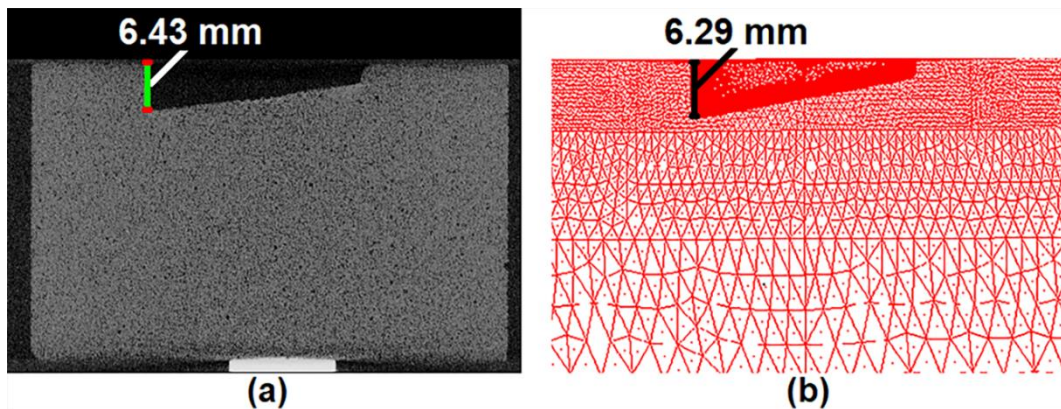


**Fig. 72** Comparison of the displacement in the front zone of the contact surface obtained with: (a) CT scan, (b) FE analysis

The footprints in the polyurethane foam blocks were compared, and the depth measured from CT scan was equal to 6.43 mm. In FE analysis it was 6.29 mm, resulting in an error percentage of 2.18%, which can be considered acceptable. From the analysis of the contact pressure at the interface between polyurethane and devices, it was useful to observe the distribution of contact pressure, as shown in Fig. 73.

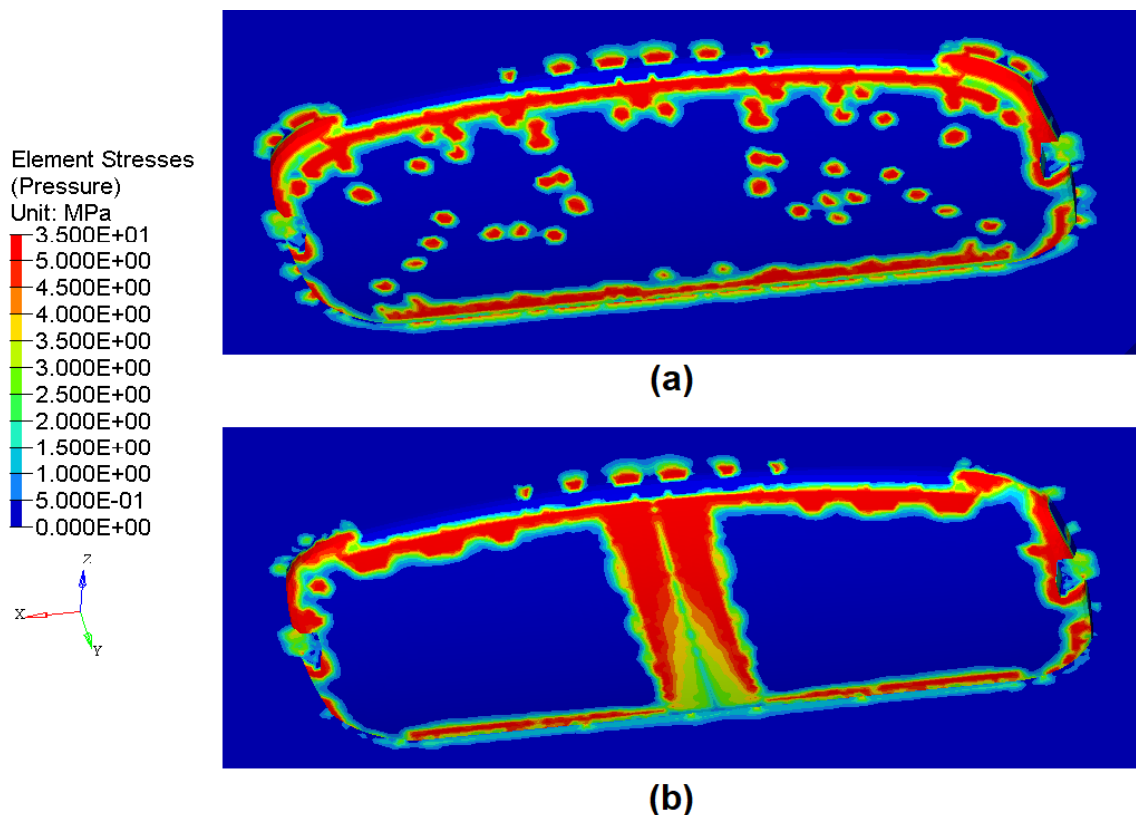


**Fig. 73** Contact pressure under a compressive load of 4 kN of the polyurethane foam blocks in the analyses with: (a) PP device, (b) S device

The contact pressure was higher than the mechanical strength of the vertebral bone found in literature (red parts in Fig. 73) [169], due to high value of the applied compressive load. The stress pattern was in accordance with the one observed in the experimental tests. As expected from the experimental tests, the microlattice structure guaranteed a smoother pressure distribution at the interface between cage and polyurethane. This behaviour can be also observed in the curves of Fig. 74, which refers to the sections marked in Fig. 75. The PP device (curves A and B) yielded some pressure peaks caused by singularity of the elements, that appeared in different parts of the contact interface for each section. The S device (curves C and D) presented for each section, pressure peaks in the central part of the contact interface, in the range between 20 and 30 mm. This trend led to overloading of the bone which constantly bears high pressure values.

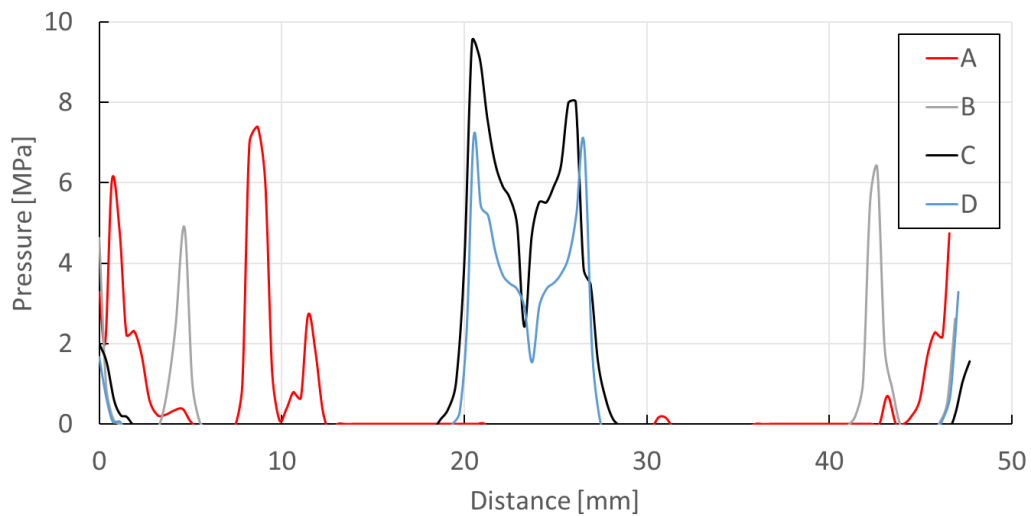


**Fig. 74** Pressure-distance curves at the interface between device and polyurethane blocks

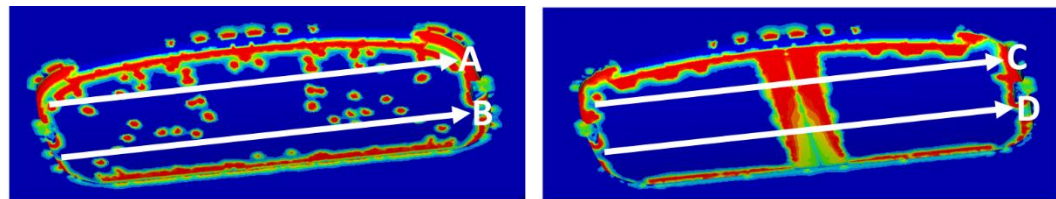


**Fig. 75** Sections considered for the pressure-distance curves

Finally, under a physiological compressive load of 0.5 kN, the distribution of contact pressure was the same of the previous cases, with lower values, as shown in Fig. 76.

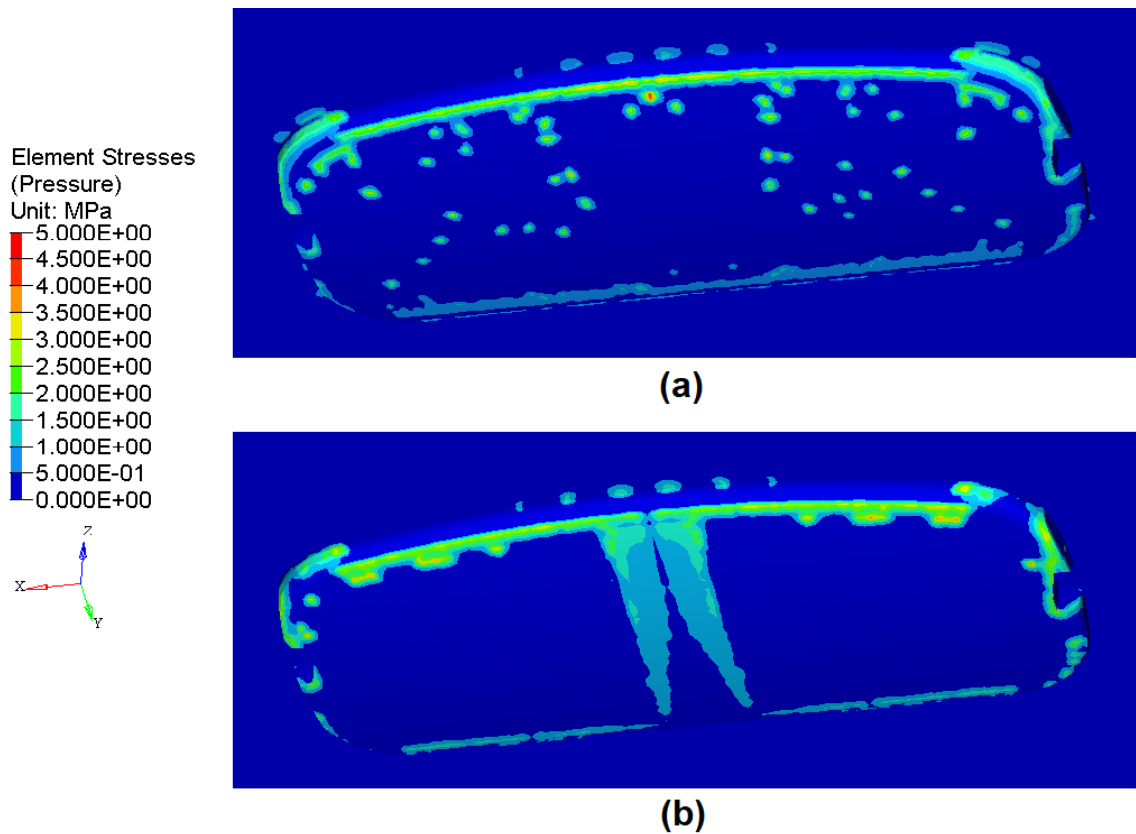


**Fig. 76** Contact pressure under a compressive load of 0.5 kN of the polyurethane foam blocks in the analyses with: (a) PP device, (b) S device

For the PP device, the contact pressure was smaller than the mechanical strength of the vertebral bone. For the S device, the values in the central zone were still smaller than the mechanical strength of the bone. Nevertheless, these values were very close to the bone compressive strength because the central part of the bone has lower mechanical properties than the external one.

## Chapter 5

# EXPERIMENTAL ANALYSIS OF TPMS GYROID SCAFFOLDS

In this chapter is presented the research activity conducted during the period in KU Leuven. The study is focused on the evaluation of the mechanical properties of the TPMS gyroid lattice material. Compressive tests and an extensive comparison of the results with models present in literature was performed to this purpose.

### 5.1. GYROID SPECIMENS PRODUCTION

Compressive tests were performed in conformity to the ISO 13314 standard [170]. Such a standard specifies a test method for compressive properties of porous and cellular metals. As recommended, cylindrical test specimens were used; all the spatial dimensions should be at least 10 times the average pore size,  $d_a$ , and no less than 10 mm, with a sample length  $H_0$  to diameter  $D_0$  ratio of between 1 and 2, as shown in Fig. 77.

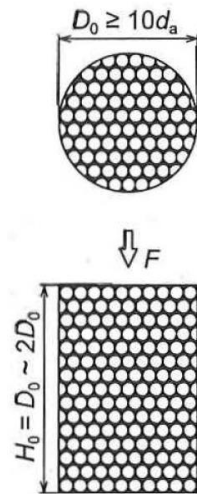
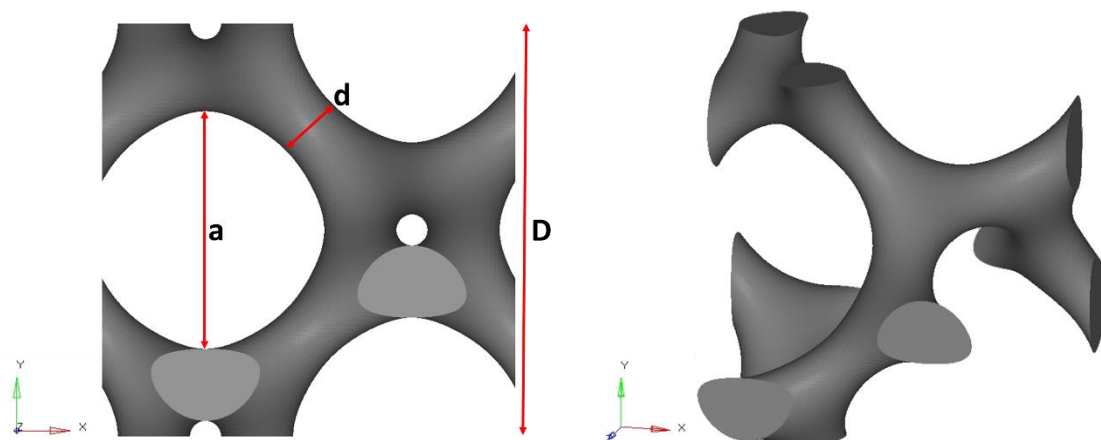


**Fig. 77** Schematic illustration of test specimen in conformity to the ISO 13314 standard [170]

The selected specimens' dimensions are  $H_0 = 25$  mm and  $D_0 = 16$  mm. Twelve levels of relative densities were analysed, ranging from 10% to 80%. Up to a relative density of 50%, increases of 5% were considered; while from 50% to 80%, steps of 10% were considered. A summary of the geometric parameters of the gyroid unit cells adopted to produce the lattice specimens are reported in Table 41, referring to Fig. 78. Where the strut diameter  $d$ , which varies along the strut, is evaluated in the thinner section.

**Table 41** Geometric parameters of the gyroid unit cells

$\rho^*/\rho_s [\%]$	D [mm]	d [mm]	a [mm]	d/D
10	1.5	0.24	0.85	0.16
15	1.5	0.29	0.79	0.20
20	1.5	0.35	0.73	0.23
25	1.5	0.40	0.67	0.27
30	1.5	0.46	0.62	0.31
35	1.5	0.51	0.56	0.34
40	1.5	0.57	0.50	0.38
45	1.5	0.62	0.44	0.41
50	1.5	0.68	0.39	0.45
60	1.5	0.79	0.27	0.52
70	1.5	0.89	0.16	0.60
80	1.5	1.00	0.04	0.67



(a) (b)

**Fig. 78** Geometric parameters of gyroid structure

The lattice structures, shown in Fig. 79, were produced via DMLS technology using Ti6Al4V ELI (Grade 23) alloy. The company did not share the manufacturing process parameters.

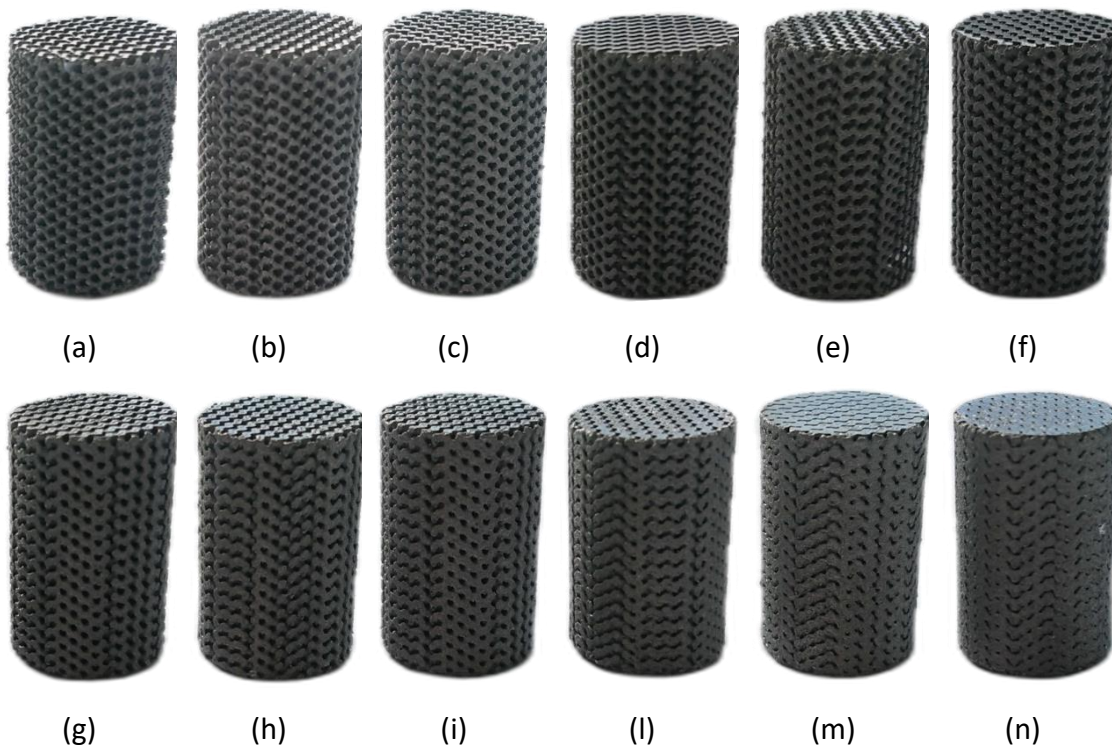


**Fig. 79** Gyroid specimens with relative densities: (a) 10%; (b) 15%; (c) 20%; (d) 25%; (e) 30%; (f) 35%; (g) 40%; (h) 45%; (i) 50%; (l) 60%; (m) 70%; (n) 80%

Three specimens were produced for each relative density, this is the minimum number of test specimens required to perform tests in conformity with the ISO 13314 standard. A comparison between designed and actual specimens' mass is provided in Table 42, Table 43, Table 44 and Table 45. Moreover, the actual specimen's relative densities, evaluated considering the actual mass, are also reported. In the ID of the specimens are indicated the relative density as percentage value and the number of the test repetition.

**Table 42** Comparison between designed and actual specimens' mass for relative densities from 10% to 20%

ID	10%_	10%_	10%_	15%_	15%_	15%_	20%_	20%_	20%_
	1	2	3	1	2	3	1	2	3
mass <sub>d</sub> [g]	2.2	2.2	2.2	3.3	3.3	3.3	4.5	4.5	4.5
mass <sub>a</sub> [g]	4.3	4.3	4.3	5.3	5.1	5.4	6.8	6.7	6.5
mass <sub>v</sub> [%]	95.5	95.5	95.5	60.6	60.6	60.6	51.1	51.1	51.1
Δmas s [g]	2.1	2.1	2.1	2.0	1.8	2.1	2.3	2.2	2.0
$\rho^*/\rho_s$									
actual [%]	19	19	19	24	23	24	31	30	29

**Table 43** Comparison between designed and actual specimens' mass for relative densities from 25% to 35%

ID	25%_1	25%_2	25%_3	30%_1	30%_2	30%_3	35%_1	35%_2	35%_3
	1	2	3	1	2	3	1	2	3
mass <sub>d</sub> [g]	5.6	5.6	5.6	6.7	6.7	6.7	7.8	7.8	7.8
mass <sub>a</sub> [g]	7.4	7.5	7.4	8.5	8.3	8.3	9.1	9.5	9.3
mass <sub>v</sub> [%]	32.1	33.9	32.1	26.9	23.9	23.9	16.7	21.8	19.2
Δmass [g]	1.8	1.9	1.8	1.8	1.6	1.6	1.3	1.7	1.5

$\rho^*/\rho_s$	actual	33	34	33	38	37	37	41	43	42
		[%]								

**Table 44** Comparison between designed and actual specimens' mass for relative densities from 40% to 50%

ID	40%_			45%_			50%_			
	1	2	3	1	2	3	1	2	3	
mass <sub>d</sub> [g]	8.9	8.9	8.9	10.0	10.0	10.0	11.1	11.1	11.1	
mass <sub>a</sub> [g]	10.1	10.2	9.9	11.0	11.1	11.0	11.7	11.7	12	
mass <sub>v</sub> [%]	13.5	14.6	11.2	10	11	10	5.4	5.4	8.1	
$\Delta m_{as}$ [g]	1.2	1.3	1.0	1.0	1.1	1.0	0.6	0.6	0.9	
$\rho^*/\rho_s$										
actual	45	46	44	49	50	49	53	53	54	
	[%]									

**Table 45** Comparison between designed and actual specimens' mass for relative densities from 60% to 80%

ID	60%_			70%_			80%_		
	1	2	3	1	2	3	1	2	3
mass <sub>d</sub> [g]	13.4	13.4	13.4	15.6	15.6	15.6	17.8	17.8	17.8
mass <sub>a</sub> [g]	13.4	13.3	13.7	15.1	15.4	15.0	16.7	17.0	16.9
mass <sub>v</sub> [%]	0	-0.7	2.2	-3.2	-1.3	-3.8	-6.2	-4.5	-5.1

$\Delta_{\text{mas}}$ s [g]	0	-0.1	0.4	-0.5	-0.2	-0.6	-1.1	-0.8	-0.9
$\rho^*/\rho_s$									
actual	60	60	62	68	69	67	75	76	76
[%]									

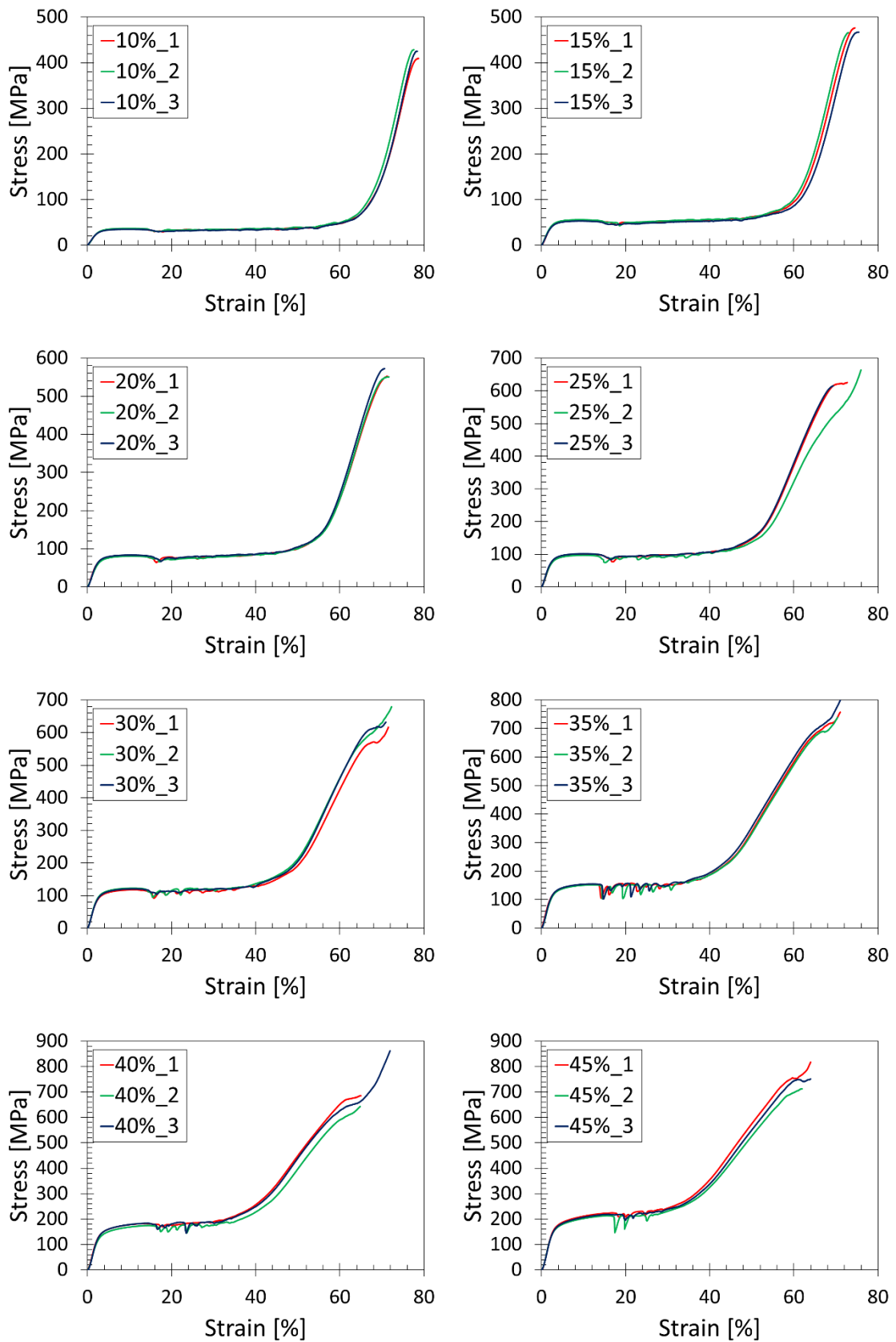
Where the subscripts stand for: d, designed; a, actual; v, variation.

Actual mass values are higher than designed ones, up to 60% relative density where the actual mass equals the designed one. For relative densities 70% and 80% the actual mass is lower than the designed one. The mass percentage variation decreases at the increase of relative density; however, the  $\Delta_{\text{mass}}$  is almost constant from 10% to 35% and is about equal to 2 mm; while, from 40 to 50% is approximately 1 mm. From 60% (where  $\Delta_{\text{mass}} \approx 0$ ) to 80%, the  $\Delta_{\text{mass}}$  increase as negative value up to -1 mm. As a consequence of the mass variation, the actual relative densities differ from the designed ones, with the same trend described for the mass.

## 5.2. COMPRESSIVE TESTS OF GYROID LATTICES

Compressive tests of the gyroid specimens were performed on an INSTRON 5985 servo-hydraulic testing machine, equipped with a 250 kN load cell. The tests were carried out at a constant crosshead speed of 1.5 mm/min and a preload of 50 N was applied during the tests. Three repetitions were carried out for each specimen configuration.

Compression tests results are reported in Fig. 80 in terms of stress-strain curves. Stress was obtained as the ratio between the axial load and the cross section of lattice specimens, whereas strain was evaluated from the crosshead displacement divided by the initial height of the specimen.



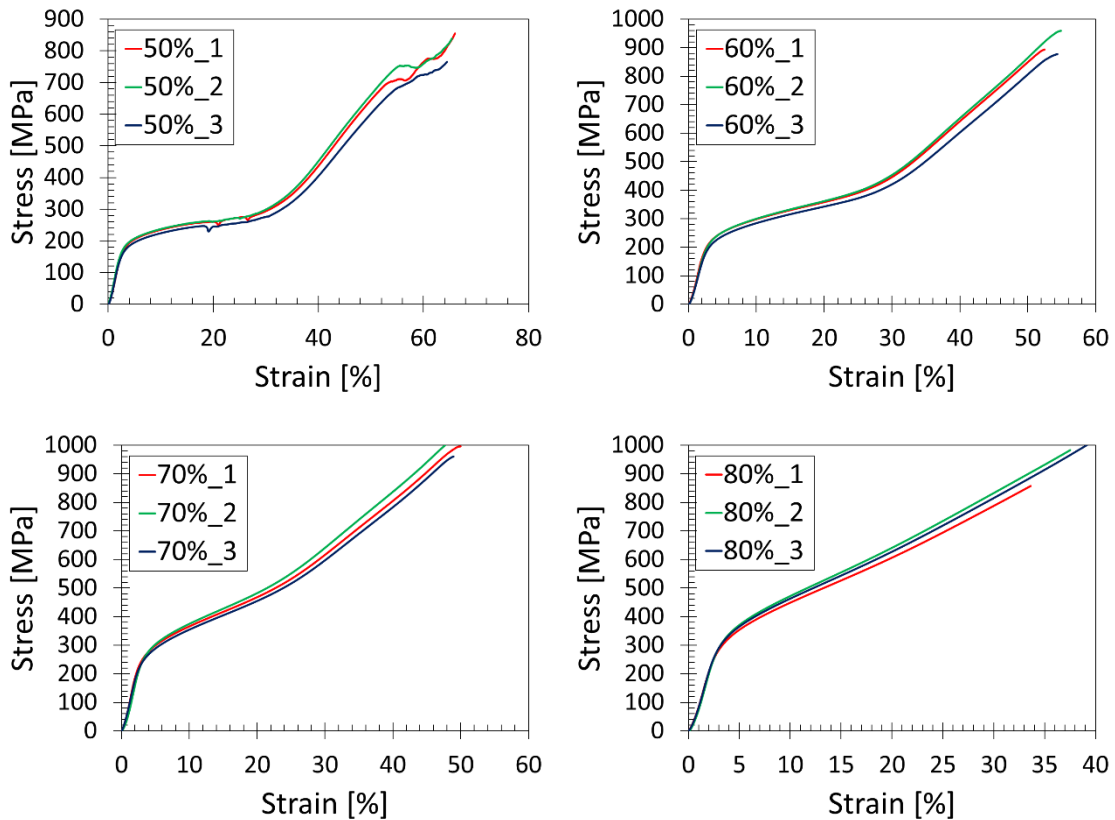


**Fig. 80** Stress-strain curves of gyroid lattices

The curves show the typical trend of bending-dominated lattice materials presented in section 2.1.2.. Elastic modulus E, yield strength  $\sigma_y$ , plateau stress  $\sigma_{pl}$ , TEA and SEA were evaluated according to the ISO 13314 standard. Elastic modulus was evaluated as the gradient of the straight line determined within the linear deformation region. Yield strength was evaluated as the stress at the plastic strain of 0.2 %. The compressive 0.2 % offset was measured from the elastic gradient used to determine the elastic modulus. Plateau stress was evaluated as the arithmetic mean stress in an interval between 20 % and 30 % of the compressive strain. This last was determined as the overall compressive displacement divided by the initial height of the test specimen, in the stress-strain curve is represented by the maximum strain that appears after the densification zone before the final collapse of the structure. From 60% relative density, a plateau region is not clearly identifiable; however, considering the compressive strain it was possible identify a pseudo-plateau region and evaluate the plateau stress for relative densities 60% and 70%. Due to safety reasons, during the tests a limit of 220 kN was imposed to the testing machine, it was not possible reaching the compressive strain of the specimen with relative

density 80%, thus the plateau stress was not evaluated in this case. As a consequence, neither TEA and SEA were evaluated for the 80% specimens; since TEA was determined as the area under the stress-strain curve up to the 130 % of the plateau stress, while SEA was determined as the ratio between TEA and the actual relative density of the test specimens. It was not possible determine the compressive strength since none of the stress-strain curves present a first local maximum after the end of the elastic region. A summary of the results is reported in Table 46, Table 47, Table 48 and Table 49

**Table 46** Compressive tests results for gyroid lattices of relative densities from 10% to 20%

	10%_ 1	10%_ 2	10%_ 3	15%_ 1	15%_ 2	15%_ 3	20%_ 1	20%_ 2	20%_ 3
E [MPa]	1343	1390.4	1322	2106.6	2139.4	2059.2	3380.7	2887.5	3409.7
$\sigma_y$ [MPa]	26.29	26.80	23.67	41.24	39.16	36.57	57.43	57.05	57.56
$\sigma_{pl}$ [MPa]	33.50	33.73	31.89	50.35	51.47	48.21	77.42	74.98	78.81
TEA [J]	96.46	98.22	92.64	138.37	140.78	130.73	198.66	188.49	198.12
SEA [Jm <sup>3</sup> /kg]	0.113	0.115	0.108	0.131	0.139	0.122	0.147	0.141	0.153
	[ ]								

**Table 47** Compressive tests results for gyroid lattices of relative densities from 25% to 35%

	25%_ 1	25%_ 2	25%_ 3	30%_ 1	30%_ 2	30%_ 3	35%_ 1	35%_ 2	35%_ 3
E [MPa]	3911	3865.1	4141.9	4754.1	5014.1	4773.5	6027.3	5780.7	5885.7
$\sigma_y$	71.85	66.85	72.42	80.58	85.75	83.62	102.92	102.64	103.88

	[MPa]								
$\sigma_{pl}$ [MPa]	94.99	90.42	95.81	112.80	118.70	116.08	149.00	145.44	147.91
TEA [J]	224.41	212.77	225.07	251.09	258.51	254.21	299.72	288.94	292.72
SEA									
[Jm <sup>3</sup> /kg]	0.152	0.143	0.153	0.148	0.157	0.154	0.166	0.153	0.158
]									

**Table 48** Compressive tests results for gyroid lattices of relative densities from 40% to 50%

	40%_ 1	40%_ 2	40%_ 3	45%_ 1	45%_ 2	45%_ 3	50%_ 1	50%_ 2	50%_ 3
E [MPa]	6478	6130.1	6713.5	7534.1	7323.7	7207.5	7878.7	8300.3	7861.5
$\sigma_y$ [MPa]	120.60	110.86	118.90	139.41	135.78	141.57	157.11	157.54	143.86
$\sigma_{pl}$ [MPa]	183.39	171.90	181.81	229.04	212.96	222.58	272.79	275.38	258.42
TEA [J]	339.61	329.65	339.50	391.50	369.66	385.54	440.62	439.07	424.56
SEA									
[Jm <sup>3</sup> /kg]	0.169	0.162	0.172	0.179	0.167	0.176	0.189	0.189	0.178
]									

**Table 49** Compressive tests results for gyroid lattices of relative densities from 60% to 80%

	60%_ 1	60%_ 2	60%_ 3	70%_ 1	70%_ 2	70%_ 3	80%_ 1	80%_ 2	80%_ 3
E [MPa]	10240	9656.8	8926.4	11858	10818	10375	12884	12764	12803
$\sigma_y$	187.80	193.83	179.90	217.06	229.69	220.41	259.22	284.01	265.66

	[MPa]								
$\sigma_{pl}$ [MPa]	395.25	400.68	375.05	534.57	553.94	515.77	/	/	/
TEA [J]	567.85	570.59	547.00	747.61	763.02	718.32	/	/	/
SEA									
[Jm <sup>3</sup> /kg]	0.213	0.216	0.201	0.249	0.249	0.241	/	/	/
]									

The mechanical properties of gyroid lattices increase at the increase of the relative density according with data present in literature [10] and with the prediction of the Gibson-Ashby model [14]. Due to the good repeatability of the tests, for an easier comparison of the results, the mean values were evaluated and the results are reported in Table 50 and Table 51. The same data are also reported in the bar graphs shown in Fig. 81. Fig. 82 depicts the stress-strain curves for the repetition with the intermediate mechanical properties of each relative density.

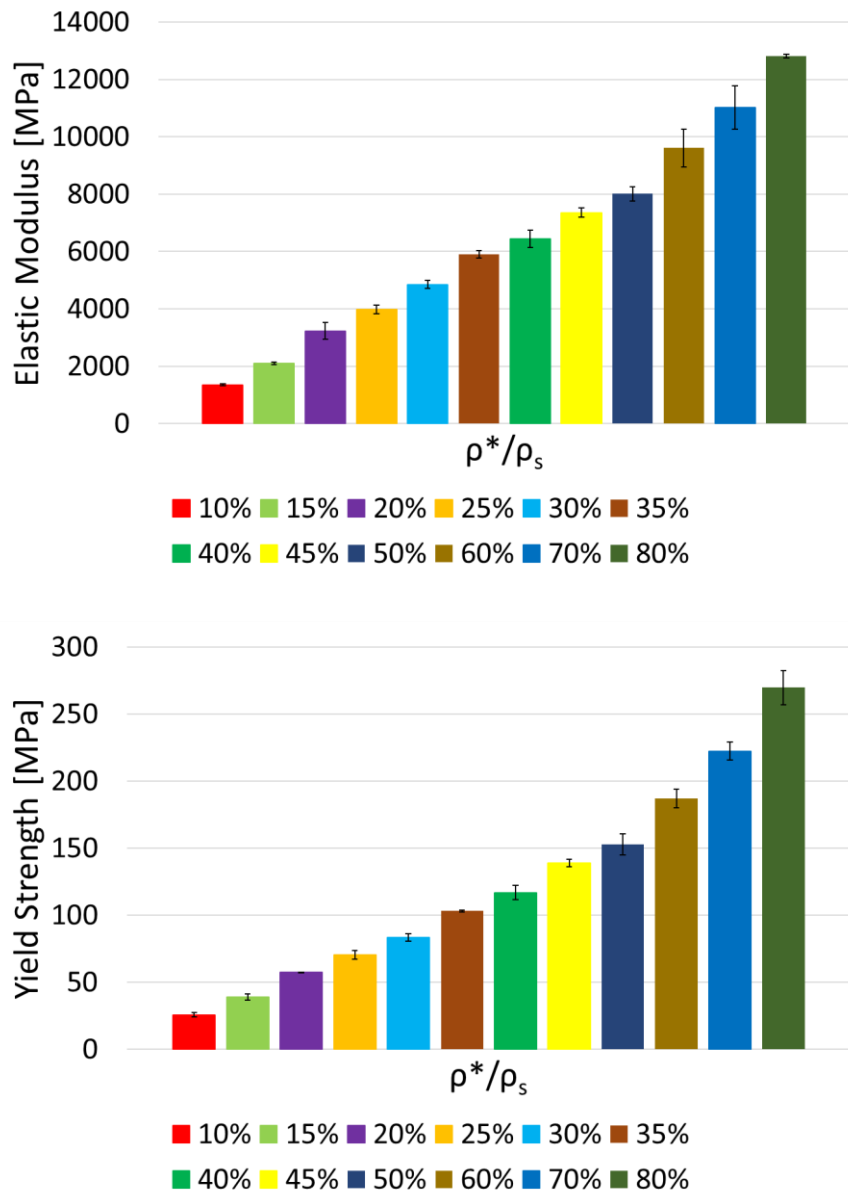
**Table 50** Mean values and standard deviation of the compressive test results for relative densities from 10% to 35%

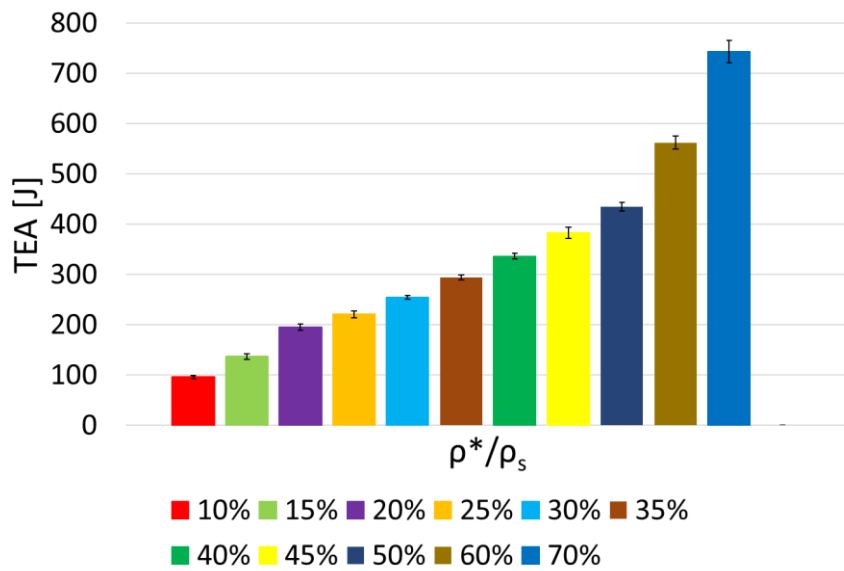
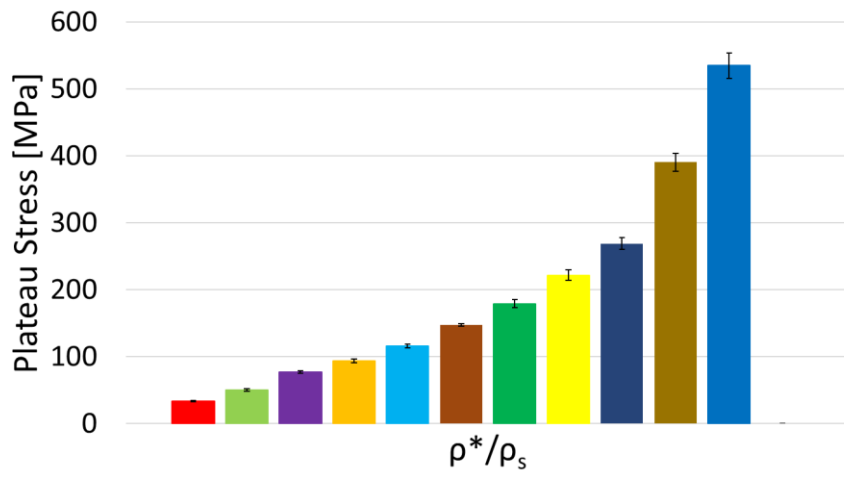
	10%	15%	20%	25%	30%	35%
E <sub>mean</sub> [MPa]	1351.8	2101.7	3226	3972.7	4847.2	5897.9
E <sub>st. dev.</sub> [MPa]	35	40.3	293.5	148.3	144.8	123.8
$\sigma_y$ mean [MPa]	25.59	38.99	57.35	70.37	83.32	103.15
$\sigma_y$ st. dev. [MPa]	1.68	2.34	0.27	3.06	2.60	0.65
$\sigma_{pl}$ mean [MPa]	33.04	50.01	77.07	93.74	115.86	147.45
$\sigma_{pl}$ st. dev. [MPa]	1.00	1.65	1.94	2.91	2.96	1.83

TEA <sub>mean</sub> [J]	95.78	136.63	195.09	220.75	254.60	293.80
TEA <sub>st. dev.</sub> [J]	2.85	5.25	5.73	6.92	3.72	5.47
SEA <sub>mean</sub> [Jm <sup>3</sup> /kg]	0.112	0.131	0.147	0.149	0.153	0.159
SEA <sub>st. dev.</sub> [Jm <sup>3</sup> /kg]	0.003	0.009	0.006	0.006	0.004	0.006

**Table 51** Mean values and standard deviation of the compressive test results for relative densities from 40% to 80%

	40%	45%	50%	60%	70%	80%
E <sub>mean</sub> [MPa]	6440.5	7355.1	8013.5	9607.7	11017	12817
E <sub>st. dev.</sub> [MPa]	293.5	165.5	248.5	658.2	761.3	61.2
σ <sub>y</sub> mean [MPa]	116.79	138.92	152.84	187.18	222.39	269.63
σ <sub>y</sub> st. dev. [MPa]	5.20	2.93	7.78	6.99	6.54	12.86
σ <sub>pl</sub> mean [MPa]	179.03	221.53	268.86	390.32	534.76	/
σ <sub>pl</sub> st. dev. [MPa]	6.23	8.09	9.14	13.50	19.08	/
TEA <sub>mean</sub> [J]	336.25	382.23	434.75	561.82	742.98	/
TEA <sub>st. dev.</sub> [J]	5.72	11.29	8.86	12.90	22.71	/
SEA <sub>mean</sub> [Jm <sup>3</sup> /kg]	0.168	0.174	0.185	0.210	0.246	/
SEA <sub>st. dev.</sub> [Jm <sup>3</sup> /kg]	0.005	0.006	0.006	0.008	0.005	/





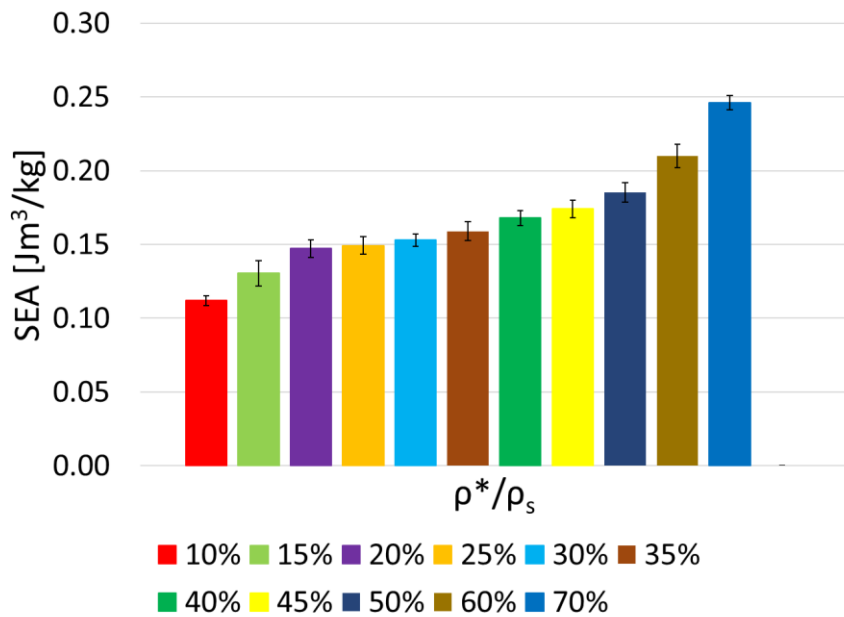


**Fig. 81** Bar graphs for the comparison of the mean values of the compressive tests results

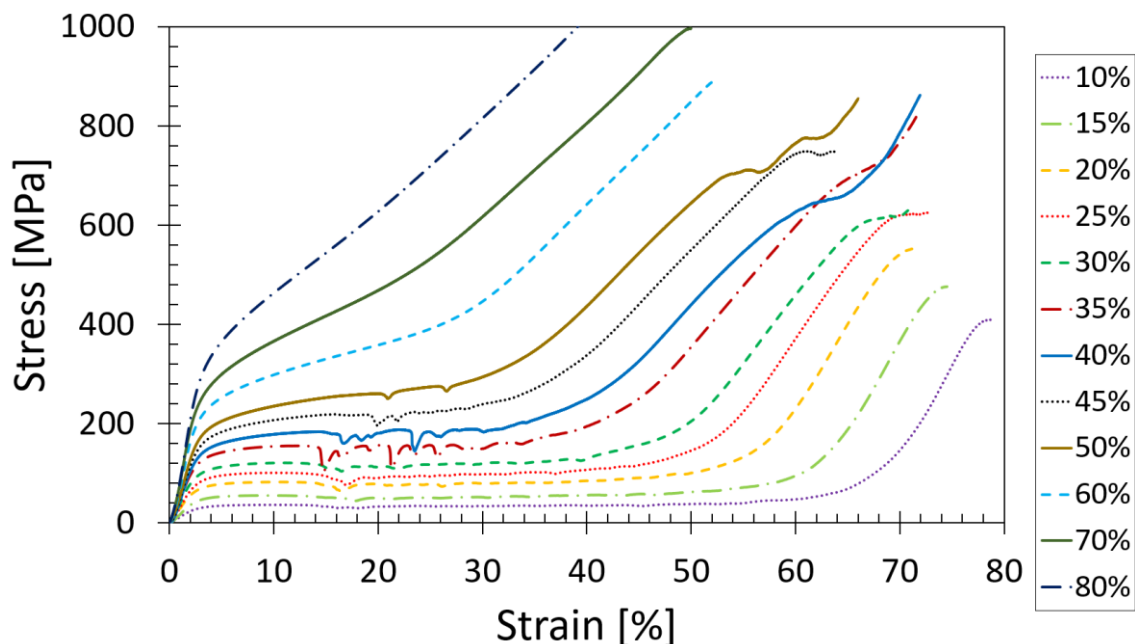


**Fig. 82** Stress-strain curves for the comparison of the results for lattices with different relative densities

Fig. 81 shows that elastic modulus and yield strength constantly increase at the increase of the relative density. Plateau stress and TEA constantly increase at the increase of relative density up to a value of 50%, while for relative densities 60% and 70% high increases are observed. Fig. 82 shows that for relative densities from 20% to 50%, in the plateau region stress fluctuations appears due to the collapse of some struts within the specimens. It can also be seen a change in the curves trend from 60% relative density. Indeed, as reported in the study of Gibson-Ashby, for some lattice topologies, a sort of limit appears at a relative density of 30% or 50% [6], [15].

Visual testing was performed to analyse the failure mode of the gyroid specimens, as shown in Fig. 83. All the tested specimens, except to 80% relative density (Fig. 83n), present a collapse due to crack propagation through the lattice along a direction parallel to the applied load. As reported in the experimental test results, the 80% specimens did not reach the final collapse of the structures under a maximum load of 220 kN.

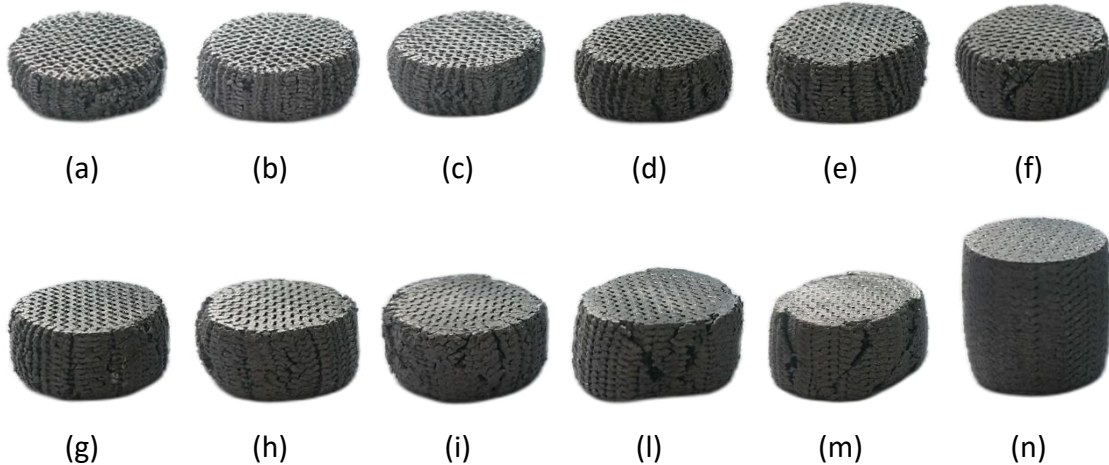


**Fig. 83** Collapse of gyroid lattices with relative densities: (a) 10%; (b) 15%; (c) 20%; (d) 25%; (e) 30%; (f) 35%; (g) 40%; (h) 45%; (i) 50%; (l) 60%; (m) 70%; (n) 80%

### 5.3. GIBSON-ASHBY MODEL OF THE GYROID LATTICE

The Gibson-Ashby model was applied to compare the results obtained during experimental tests with the published models from literature.

To perform a reliable comparison, some restrictions in the choice of the models from literature were imposed, as follows: a minimum of three relative densities evaluated, a minimum coefficient of determination of 0.95 for the interpolation of the power law relationship; the evaluation of both Gibson-Ashby constants were imposed, thus were discarded all that studies that considered the predicted  $n = 2$  value of the bending-

dominated structure. Finally, the data interpolation should be performed considering the actual specimen relative density and not the designed one. With regards of the compressive tests performed in this research, considering the designed relative density significantly affects the Gibson-Ashby model, as shown in Fig. 84.

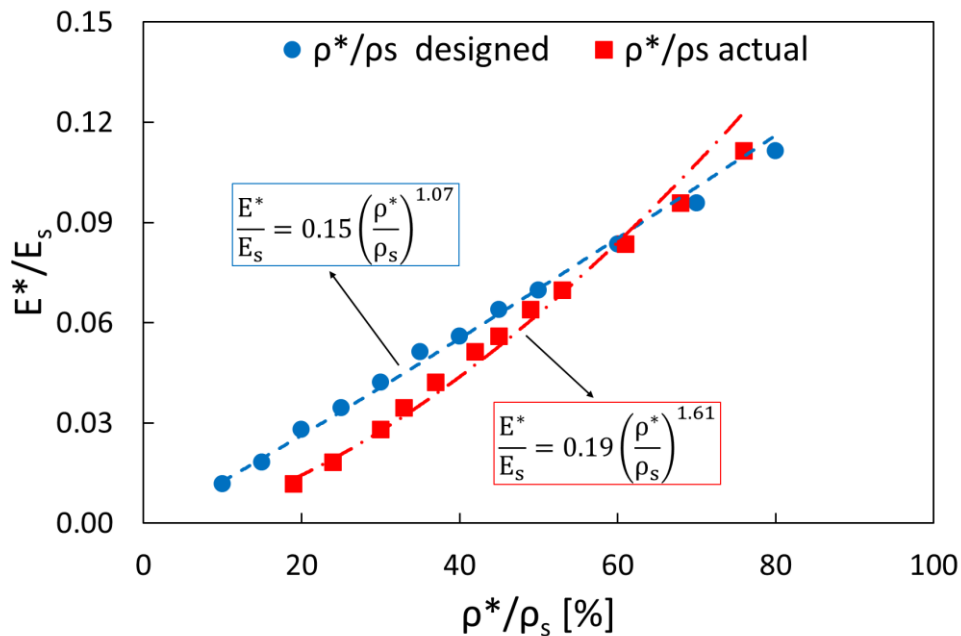


**Fig. 84** Comparison between the Gibson-Ashby model evaluated considering the designed or the actual relative density

The  $R^2$  values for the designed and the actual relative densities are respectively 0.99 and 0.98. The selected researcher papers for the comparison of the Gibson-Ashby model are: Ataei et al. [171] carried out compressive tests in conformity to the ISO 13314 standard on specimens made of pure titanium (CP-Ti) manufactured by SLM technology. Gyroid scaffolds with sizes if 5x5x5 unit cells, three relative densities in the range of 27% and 32% and three unit cell sizes of 2, 2.5 and 3 mm were evaluated. The  $R^2$  values was 0.96. Yan et al. [61] manufactured by SLM, gyroid lattices made of Ti6Al4V ELI alloy, with six levels of relative densities between 5% and 20%. The  $R^2$  values was 0.99. Al-Ketan et al. [3] considered cellular structures made of Maraging steel fine powder and 3D printed using the powder bed fusion system. Four relative densities were considered between 10% and 30%. Each sample consists of 6 unit cells in each direction, for a total of 216 unit cells. The cubical samples have a total length of 42 mm, thus the cell size is 7 mm. In this study a revised Gibson-Ashby formula was applied, thus the constant C and

n were recalculated considering the original formula [6]. The  $R^2$  value was 0.98. The comparison of the Gibson-Ashby model of the relative modulus against the relative density is shown in Fig. 85.

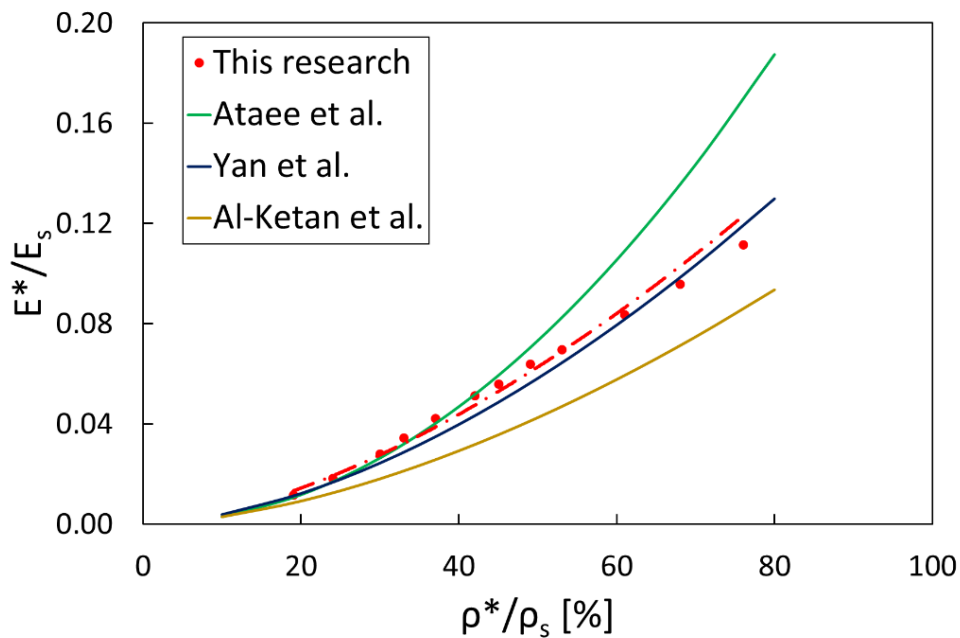


**Fig. 85** Comparison of the Gibson-Ashby model between compressive tests results and models from literature

As it can be seen, all the selected models match well for lower relative densities. The results diverge at the increase of the relative density. The results of the present research are in accordance with the model of Yan et al. since the material and the AM technique adopted were the same.

## **Chapter 6**

### **CONCLUSIONS**

The main objective of the present PhD thesis was the design of a novel lattice material. Biomimetic theory was applied for the design of the new TAOR lattice. Following the generic bio-inspiration approach, the observation of rocks, and in particular the evolution of polygonal fracture patterns in volcanic rocks, led to the design of the TAOR cell. A static FE analysis of regular polygons helped for the development of the final shape of the TAOR cell. The results confirmed the effectiveness of the biomimetic approach in the design of cellular and lattice materials, since this approach allowed to obtain a cubic symmetric and periodic structure based on the scheme of rocks.

The design and the subsequent experimental investigation of the novel TAOR lattice aimed to meet the mechanical and morphological requirements for biomedical applications. The results of the compressive tests and morphological analysis confirmed the suitability of the TAOR cell for possible biomedical applications in devices used as bone substitutes. A comparison with lattice structures currently used for applications in this field, namely truncated octahedron (Kelvin cell), rhombic dodecahedron and G7 was conducted. For all the tested lattices, the fracture appears at the cross nodes of the structures, all configurations analysed present a macroscopic failure in the form of a shear plane inclined with an angle of about 45°. According to the Gibson-Ashby model, the mechanical properties increase at the increase of the relative density. TAOR cell exhibits higher mechanical properties than Kelvin cell, lower strength and higher energy absorption properties compared to the G7 cell. From the comparison with the rhombic dodecahedron cell, it was noticed that TAOR exhibits higher or lower mechanical properties depending on the relative density considered. This can be explained by the fact that morphological analysis highlighted discrepancies between designed and actual geometric parameters produced by EBM technology. In particular, the actual strut diameter is twice the designed one for all the configurations analysed. The unmatching between designed and actual relative density was also confirmed during the activity performed at KU Leuven for specimens produced via DMLS technology. The limit of the

AM can be overcome with the application of the Gibson-Ashby model which allows to compare the mechanical properties of lattice structures for a given relative density.

The results of the compressive tests are useful to build the power-law relationship between mechanical properties and relative density. The results of the model confirmed that TAOR cell presents higher mechanical properties than Kelvin cell. Compared to the G7 cell, TAOR lattice shows lower mechanical properties at low relative densities, while they are higher at high relative densities. The Gibson-Ashby model also confirmed the bending-dominated behaviour of the TAOR cell previously estimated with the Maxwell stability criterion.

An extensive numerical analysis of the TAOR lattice was conducted. A preliminary linear static FE analysis was carried out to estimate the elastic modulus of the new TAOR cell, the stress distribution within the lattice structure and the unit cell size effect on the mechanical response. Elastic modulus significantly increases at the increase of the relative density, while it slightly decreases at the increase of the cell size. The cell size effect is more pronounced in the greater relative density. The comparison with the results of the experimental tests showed that the numerical model overestimates the elastic modulus of the lattice material, the differences between numerical and experimental results increase at the increase of the relative density.

The Johnson-Cook material model was developed and validated to simulate the plastic behaviour of the TAOR cell. A FE model of the single unit cell was developed to evaluate the compressive behaviour and the failure mode of the cell, without the presence of adjacent cells that affect the deformation process. The analysis confirmed that the failure appears at the cross nodes of the structure. A symmetric failure was evaluated, the central portion of the cell, which includes the vertical strut, is the last part to fail. The final collapse of the cell is due to the buckling of the vertical strut. The FE models of lattices with 2 or 3 unit cells for each specimen edge were developed to evaluate the mechanical properties of the TAOR cell. The results showed that the FE analysis represents a reliable support tool for the analysis of the mechanical behaviour of lattice materials. However, an extensive experimental analysis is necessary to exactly evaluate the mechanical properties of a lattice material, since the CAD models used in FE analysis does not include all the defects due to the AM process, leading to a bias of the mechanical properties.

One of the aims of the thesis was to test the mechanical performance of lattice structures applied in existing biomedical implants. A case study regarding the application of rhombic dodecahedron cell was conducted, in preparation for a future development of the

research with the inclusion of the novel TAOR cell. The subsidence phenomenon of lumbar intervertebral body fusion devices under the application of compressive load was investigated by means of experimental tests and finite element analyses. The contact pressure at the interface between implants and polyurethane foam blocks was evaluated by comparing a partially porous device and a skeletal device.

The experimental tests showed that the subsidence risk is higher in the traditional device, which is characterised by lower stiffness, lower maximum load, and a smaller contact surface compared to the partially porous device. On the contrary, it was observed that the presence of lattice structure guaranteed a smoother pressure distribution at the contact interface, despite not having any structural function as confirmed in the FE analyses.

The results of the present research do not aim at demonstrating that PP device has enhanced mechanical properties, since the peak stress values are comparable for the two analysed devices. On the other hand, the results showed that the presence of lattice structures resulted in an optimal pressure distribution on the bone surface, decreasing the risk of subsidence. This behaviour is particularly important in the lumbar region, in which vertebral bodies bear high compressive loads.

Both experimental and numerical results may be used in the design of novel intervertebral body fusion devices, considering the good agreement between the numerical results and the experimental data. In addition, they can be used to optimise the presence of both porous and bulk structure, to obtain more efficient devices.

The main advantage of the method used in the study is the possibility to validate FE analyses for a precise and careful design of the device. Nevertheless, the standard procedure didn't consider the possibility to test the device behaviour when a subject-specific design procedure is required for a peculiar geometry of the vertebra to be implanted. Such a limitation can be overcome by FEA, even though it gives an approximated result of the subsidence behaviour since it is calibrated on PU foam. Another drawback of the method stands also in the lack of consideration of the mechanical properties of the bone to be implanted. This aspect can be also overcome by developing a FEA based on the mechanical properties obtained by CT scans, through the evaluation of the bone apparent density.

The first part of the PhD was mainly focused on the study of strut-based lattice materials. During the stay at KU Leuven University, the focus of the research shifted on TPMS lattice materials. The mechanical properties of the TPMS gyroid lattice were evaluated by carrying out compressive tests in conformity with ISO 13314 standard. The results

showed good repeatability and the mechanical properties increase at the increase of the relative density according with data present in literature. The 50% relative density represents a sort of a limit for the gyroid lattice, indeed the specimens with 60% or higher relative densities showed a different trend in the stress-strain curve, with the almost complete absence of the plateau region.

The Gibson-Ashby model allowed to compare the results of the compressive tests with published models from literature. The gyroid lattice is one of the most studied structures, several models are present in literature, which show a high variety of mechanical properties. To perform a reliable comparison, limits were imposed in the choice of the models from literature; thus, only models that meet different requirements were taken into account. From the comparison, it can be seen that all the selected models match well for lower relative densities, while the results diverge at the increase of the relative density. In conclusion it can be asserted that the proposed TAOR cell meets the mechanical and morphological requirements for application in the biomedical field, thus it can represent a relevant design choice to produce bone scaffold. Further investigations are needed to assess the TAOR suitability with the biological requirement for application in this field. The present PhD thesis focused on the biomedical field and lower relative density values, proper to this field were analysed; however, the Gibson-Ashby model allows to predict the mechanical properties for higher relative density proper to other fields application. Titanium alloys are suitable for aerospace applications due to the possible joint with carbon.

# FIGURES AND TABLES

<b>Fig. 1</b> Cellular solids: (a) honeycomb; (b) foam; (c) lattice .....	2
<b>Fig. 2</b> From foam to lattice structure [8] .....	2
<b>Fig. 3</b> Gibson-Ashby lattice structure.....	9
<b>Fig. 4</b> Strut-based lattice structures: (a) BCC; (b) BCCZ; (c) FCC; (d) FCCZ; (e) cubic; (f) octet-truss; (g) diamond [10] .....	10
<b>Fig. 5</b> Structure of the octet-truss lattice material [46] .....	10
<b>Fig. 6</b> BCC derived lattice structures: (a) G7; (b) SCBCC [15].....	11
<b>Fig. 7</b> Archimedean and Catalan solids lattice structures: (a) cuboctahedron; (b) truncated cube; (c) truncated octahedron (Kelvin); (d) rhombicuboctahedron; (e) truncated cuboctahedron; (f) rhombic dodecahedron [48], [50].....	12
<b>Fig. 8</b> TPMS lattice structures: (a) skeletal gyroid; (b) skeletal diamond; (c) skeletal IWP; (d) sheet gyroid; (e) sheet diamond; (f) sheet IWP; (g) Schwarz primitive; (h) FRD; (i) Neovius .....	15
<b>Fig. 9</b> Novel lattice structure present in literature [69]–[71] .....	15
<b>Fig. 10</b> Stress-strain curve of a bending-dominated lattice [14].....	16
<b>Fig. 11</b> Stress-strain curve of a bending-dominated lattice [14].....	17
<b>Fig. 12</b> Gibson-Ashby model: relative modulus against relative density [14] .....	19
<b>Fig. 13</b> Gibson-Ashby model: relative strength against relative density [14] .....	19
<b>Fig. 14</b> Successive cell collapse failure mode [73] .....	20
<b>Fig. 15</b> Crack propagation through the lattice failure mode [73] .....	20
<b>Fig. 16</b> Diagonal shear failure mode [73] .....	20
<b>Fig. 17</b> Geometric parameters of the truncated octahedron (strut-based) lattice structure .....	21
<b>Fig. 18</b> Geometric parameters of the TPMS gyroid (sheet-based) lattice structure .....	22
<b>Fig. 19</b> Regular polygon dimensions .....	27
<b>Fig. 20</b> Boundary conditions of the first set of analyses on polygonal prisms .....	28
<b>Fig. 21</b> Polygonal prisms FE analysis results .....	29
<b>Fig. 22</b> Ring generated by the combination of multiple octagons.....	31
<b>Fig. 23</b> Boundary conditions of the analysis on polygonal rings .....	32

<b>Fig. 24</b> Polygonal rings FE analysis results .....	33
<b>Fig. 25</b> (a) ring of the new unit cell; (b) complete structure of the new unit cell .....	34
<b>Fig. 26</b> TAOR cell.....	34
<b>Fig. 27</b> Volume considered in the first method for the evaluation of the relative density .....	35
<b>Fig. 28</b> Volume considered in the second method for the evaluation of the relative density .....	36
<b>Fig. 29</b> Comparison of the relative densities evaluated with the two methods, as a function of: (a) $d/D$ ; (b) $d/L$ .....	37
<b>Fig. 30</b> Geometric parameters of the TAOR cell .....	39
<b>Fig. 31</b> Specimens: (a) TAOR_5%; (b) TAOR_10%; (c) TAOR_20%; (d) Kelvin_5%; (e) Kelvin_10%; (f) Kelvin_20%; (g) G7_5%; (h) G7_10%; (i) G7_20% .....	41
<b>Fig. 32</b> SEM images of lattices with 10% relative density: (a) TAOR; (b) Kelvin; (c) G7 .....	43
<b>Fig. 33</b> Topography of the strut surface: (a) roughness profiles; (b) 3D reconstruction of the surface. ....	46
<b>Fig. 34</b> Stress-strain curves .....	50
<b>Fig. 35</b> Gibson-Ashby diagrams: (a) relative modulus; (b) relative strength .....	52
<b>Fig. 36</b> Gibson-Ashby model for the comparison of the TAOR with other unit cells: (a) relative modulus against relative density; (b) relative strength against relative density [10]. .....	53
<b>Fig. 37</b> Failure mode for lattices of relative density 10%: (a) TAOR; (b) Kelvin; (c) G7 .....	55
<b>Fig. 38</b> SEM images, unit cells fracture: (a) TAOR; (b) Kelvin; (c) G7 .....	55
<b>Fig. 39</b> SEM images, particular of the surface fracture: (a) TAOR cell; (b) Kelvin cell	55
<b>Fig. 40</b> Linear static FE model boundary conditions .....	59
<b>Fig. 41</b> Linear static FE analysis results of TAOR with relative density 5% .....	60
<b>Fig. 42</b> Linear static FE analysis results of TAOR with relative density 10% .....	61
<b>Fig. 43</b> Linear static FE analysis results of TAOR with relative density 15% .....	62
<b>Fig. 44</b> Linear static FE analysis results of TAOR with relative density 20% .....	63
<b>Fig. 45</b> Linear static FE analysis results of TAOR with relative density 25% .....	64
<b>Fig. 46</b> Linear static FE analysis results of TAOR with relative density 30% .....	65
<b>Fig. 47</b> Peak Von Mises stresses for different cell sizes and relative densities .....	66
<b>Fig. 48</b> Gibson-Ashby diagram of the linear static FE analysis results .....	68

---

<b>Fig. 49</b> Tensile specimen .....	72
<b>Fig. 50</b> Boundary conditions FE model tensile test.....	73
<b>Fig. 51</b> Comparison between the results of the experimental test and the FE analysis for the validation of the material model .....	74
<b>Fig. 52</b> Boundary conditions for FE model validation .....	75
<b>Fig. 53</b> (a) load-displacement and (b) stress-strain curve of the FE validation analysis	76
<b>Fig. 54</b> Failure mode of the G7 specimen FE analysis for the validation of the JC material model to simulate the plastic behaviour of lattice materials.....	76
<b>Fig. 55</b> Steps for the meshing of the TAOR cell .....	79
<b>Fig. 56</b> Section of the TAOR cell mapped mesh .....	80
<b>Fig. 57</b> Steps for the meshing of the IWP cell .....	80
<b>Fig. 58</b> FE model boundary conditions of the non-linear analysis of the single unit cells .....	81
<b>Fig. 59</b> TAOR cell and Kelvin cell FE analysis results.....	84
<b>Fig. 60</b> G7 cell FE analysis results .....	85
<b>Fig. 61</b> IWP cell FE analysis results.....	86
<b>Fig. 62</b> FE model boundary conditions of the non-linear analysis of the TAOR specimens .....	88
<b>Fig. 63</b> Stress-strain curves of the non-linear FE analysis of the TAOR specimens.....	88
<b>Fig. 64</b> Surgical approaches to the lumbar spine for interbody fusion techniques.....	91
<b>Fig. 65</b> Devices object of the study: (a) with porous microlattice core; (b) without porous microlattice core .....	94
<b>Fig. 66</b> Surface analysis of the device .....	95
<b>Fig. 67</b> Tooling of Polyurethane foam blocks: (a) raw blocks; (b) CNC machining; (c) final result with a perfect fit of the device into the block .....	96
<b>Fig. 68</b> Polyurethane foam blocks with the cage implanted: (a) compression tests, (b) intradiscal height.....	97
<b>Fig. 69</b> Load-displacement curves for PP device and S device .....	98
<b>Fig. 70</b> Stress distribution at the interface between polyurethane foam blocks and: (a) PP device, (b) S device.....	100
<b>Fig. 71</b> Boundary conditions of the FE subsidence analysis .....	104
<b>Fig. 72</b> Comparison of the displacement in the front zone of the contact surface obtained with: (a) CT scan, (b) FE analysis .....	105

<b>Fig. 73</b> Contact pressure under a compressive load of 4 kN of the polyurethane foam blocks in the analyses with: (a) PP device, (b) S device .....	106
<b>Fig. 74</b> Pressure-distance curves at the interface between device and polyurethane blocks .....	107
<b>Fig. 75</b> Sections considered for the pressure-distance curves.....	107
<b>Fig. 76</b> Contact pressure under a compressive load of 0.5 kN of the polyurethane foam blocks in the analyses with: (a) PP device, (b) S device .....	108
<b>Fig. 77</b> Schematic illustration of test specimen in conformity to the ISO 13314 standard [170] .....	109
<b>Fig. 78</b> Geometric parameters of gyroid structure .....	111
<b>Fig. 79</b> Gyroid specimens with relative densities: (a) 10%; (b) 15%; (c) 20%; (d) 25%; (e) 30%; (f) 35%; (g) 40%; (h) 45%; (i) 50%; (l) 60%; (m) 70%; (n) 80% .....	111
<b>Fig. 80</b> Stress-strain curves of gyroid lattices .....	116
<b>Fig. 81</b> Bar graphs for the comparison of the mean values of the compressive tests results .....	123
<b>Fig. 82</b> Stress-strain curves for the comparison of the results for lattices with different relative densities .....	123
<b>Fig. 83</b> Collapse of gyroid lattices with relative densities: (a) 10%; (b) 15%; (c) 20%; (d) 25%; (e) 30%; (f) 35%; (g) 40%; (h) 45%; (i) 50%; (l) 60%; (m) 70%; (n) 80% .....	124
<b>Fig. 84</b> Comparison between the Gibson-Ashby model evaluated considering the designed or the actual relative density .....	125
<b>Fig. 85</b> Comparison of the Gibson-Ashby model between compressive tests results and models from literature .....	126
<b>Table 1</b> Width dimension of the prisms in the second set of analysis.....	27
<b>Table 2</b> Ti6Al4V ELI alloy mechanical properties [105].....	28
<b>Table 3</b> Dimensions of the polygons forming the perimeter of the rings.....	31
<b>Table 4</b> As designed geometric parameters of the TAOR, Kelvin and G7 unit cells....	39
<b>Table 5</b> As designed geometric parameters of the TAOR, Kelvin and G7 specimens...	41
<b>Table 6</b> Specimens dimensions comparison between designed and actual values.....	42
<b>Table 7</b> Cells dimensions comparison between designed and actual values .....	43
<b>Table 8</b> Designed relative density comparison between single unit cells and specimens .....	45

---

<b>Table 9</b> Actual specimen relative density .....	45
<b>Table 10</b> Compressive tests results .....	48
<b>Table 11</b> Relative modulus, relative strength and actual relative density of the tested lattice structures .....	51
<b>Table 12</b> Gibson-Ashby constants evaluated for the tested lattice structures .....	52
<b>Table 13</b> Mechanical properties of the tested lattice structures from Gibson-Ashby model .....	54
<b>Table 14</b> Geometric parameters of TAOR cell with 5 mm cell size.....	57
<b>Table 15</b> Geometric parameters of TAOR cell with 6 mm cell size.....	57
<b>Table 16</b> Geometric parameters of TAOR cell with 7.5 mm cell size .....	58
<b>Table 17</b> Geometric parameters of TAOR cell with 10 mm cell size.....	58
<b>Table 18</b> Ti6Al4V ELI alloy mechanical properties [105] .....	59
<b>Table 19</b> Linear static FE analysis results of TAOR with 5 mm cell size .....	66
<b>Table 20</b> Linear static FE analysis results of TAOR with 6 mm cell size .....	67
<b>Table 21</b> Linear static FE analysis results of TAOR with 7.5 mm cell size .....	67
<b>Table 22</b> Linear static FE analysis results of TAOR with 10 mm cell size .....	67
<b>Table 23</b> Gibson-Ashby constant of the linear static FE analysis.....	68
<b>Table 24</b> Material constants of JC model suggested for Ti6Al4V alloy .....	70
<b>Table 25</b> Tensile specimen dimensions.....	71
<b>Table 26</b> Mechanical properties of the Ti6Al4V ELI alloy .....	72
<b>Table 27</b> JC strength model parameters of Ti6Al4V ELI alloy .....	72
<b>Table 28</b> JC fracture model parameters of Ti6Al4V ELI alloy .....	73
<b>Table 29</b> Evaluation of the percentage error of the results of the tensile tests.....	74
<b>Table 30</b> Geometric parameters of TAOR cell and Kelvin cell for FE analysis.....	78
<b>Table 31</b> Geometric parameters of G7 cell for FE analysis .....	78
<b>Table 32</b> Geometric parameters of IWP cell for FE analysis.....	79
<b>Table 33</b> Geometric parameters of the TAOR cell for the FE analysis .....	87
<b>Table 34</b> FE analysis results of the non-linear model of the TAOR specimens .....	89
<b>Table 35</b> Surface analysis results .....	95
<b>Table 36</b> Device-foam stiffness and energy absorbed during experimental tests .....	99
<b>Table 37</b> Mesh sensitivity test of the device: compression stresses.....	101
<b>Table 38</b> Mesh sensitivity test of the device: tension stresses .....	101
<b>Table 39</b> Mesh sensitivity test of the polyurethane blocks .....	102
<b>Table 40</b> FE model material properties .....	103

<b>Table 41</b> Geometric parameters of the gyroid unit cells .....	110
<b>Table 42</b> Comparison between designed and actual specimens' mass for relative densities from 10% to 20% .....	112
<b>Table 43</b> Comparison between designed and actual specimens' mass for relative densities from 25% to 35% .....	112
<b>Table 44</b> Comparison between designed and actual specimens' mass for relative densities from 40% to 50% .....	113
<b>Table 45</b> Comparison between designed and actual specimens' mass for relative densities from 60% to 80% .....	113
<b>Table 46</b> Compressive tests results for gyroid lattices of relative densities from 10% to 20% .....	117
<b>Table 47</b> Compressive tests results for gyroid lattices of relative densities from 25% to 35% .....	117
<b>Table 48</b> Compressive tests results for gyroid lattices of relative densities from 40% to 50% .....	118
<b>Table 49</b> Compressive tests results for gyroid lattices of relative densities from 60% to 80% .....	118
<b>Table 50</b> Mean values and standard deviation of the compressive test results for relative densities from 10% to 35% .....	119
<b>Table 51</b> Mean values and standard deviation of the compressive test results for relative densities from 40% to 80% .....	120

## REFERENCES

- [1] T. Maconachie *et al.*, “The effect of topology on the quasi-static and dynamic behaviour of SLM AlSi10Mg lattice structures,” *International Journal of Advanced Manufacturing Technology*, vol. 118, no. 11–12, pp. 4085–4104, Feb. 2022, doi: 10.1007/s00170-021-08203-y.
- [2] T. Kim, C. Y. Zhao, T. J. Lu, and H. P. Hodson, “Convective heat dissipation with lattice-frame materials,” in *Mechanics of Materials*, Aug. 2004, vol. 36, no. 8, pp. 767–780. doi: 10.1016/j.mechmat.2003.07.001.
- [3] O. Al-Ketan, R. Rowshan, and R. K. Abu Al-Rub, “Topology-mechanical property relationship of 3D printed strut, skeletal, and sheet based periodic metallic cellular materials,” *Addit Manuf*, vol. 19, pp. 167–183, Jan. 2018, doi: 10.1016/j.addma.2017.12.006.
- [4] T. D. Ngo, A. Kashani, G. Imbalzano, K. T. Q. Nguyen, and D. Hui, “Additive manufacturing (3D printing): A review of materials, methods, applications and challenges,” *Composites Part B: Engineering*, vol. 143. Elsevier Ltd, pp. 172–196, Jun. 15, 2018. doi: 10.1016/j.compositesb.2018.02.012.
- [5] L. J. Gibson and M. F. Ashby, “Cellular Solids - Structure and Properties,” 1997.
- [6] L. J. Gibson, “Biomechanics of cellular solids,” *J Biomech*, vol. 38, no. 3, pp. 377–399, 2005, doi: 10.1016/j.jbiomech.2004.09.027.
- [7] K. Li, X. L. Gao, and A. K. Roy, “Micromechanics model for three-dimensional open-cell foams using a tetrakaidecahedral unit cell and Castigliano’s second theorem,” *Compos Sci Technol*, vol. 63, no. 12, pp. 1769–1781, 2003, doi: 10.1016/S0266-3538(03)00117-9.
- [8] A. G. Dement’ev and O. G. Tarakanov, “Effect of cellular structure on the mechanical properties of plastic foams,” *Polymer Mechanics*, vol. 6, no. 4, pp. 519–525, 1970, doi: 10.1007/BF00856299.

- [9] T. Maconachie *et al.*, “SLM lattice structures: Properties, performance, applications and challenges,” *Mater Des*, vol. 183, p. 108137, 2019, doi: 10.1016/j.matdes.2019.108137.
- [10] S. J. Li *et al.*, “Influence of cell shape on mechanical properties of Ti-6Al-4V meshes fabricated by electron beam melting method,” *Acta Biomater*, vol. 10, no. 10, pp. 4537–4547, Oct. 2014, doi: 10.1016/j.actbio.2014.06.010.
- [11] R. Hou, J. L. Beck, X. Zhou, and Y. Xia, “Structural damage detection of space frame structures with semi-rigid connections,” *Eng Struct*, vol. 235, May 2021, doi: 10.1016/j.engstruct.2021.112029.
- [12] R. Singh, R. Kumar, A. Mishra, and A. Agarwal, “Structural Analysis of Quadcopter Frame,” 2019. [Online]. Available: [www.sciencedirect.com](http://www.sciencedirect.com)
- [13] M. F. Ashby, “The properties of foams and lattices,” *Philosophical Transactions of the Royal Society A: Mathematical, Physical and Engineering Sciences*, vol. 364, no. 1838, pp. 15–30, Jan. 2006, doi: 10.1098/rsta.2005.1678.
- [14] C. Peng, P. Tran, H. Nguyen-Xuan, and A. J. M. Ferreira, “Mechanical performance and fatigue life prediction of lattice structures: Parametric computational approach,” *Compos Struct*, vol. 235, Mar. 2020, doi: 10.1016/j.compstruct.2019.111821.
- [15] D. Shidid, M. Leary, P. Choong, and M. Brandt, “Just-in-time design and additive manufacture of patient-specific medical implants,” in *Physics Procedia*, 2016, vol. 83, pp. 4–14. doi: 10.1016/j.phpro.2016.08.002.
- [16] H. Zhou *et al.*, “Lightweight structure of a phase-change thermal controller based on lattice cells manufactured by SLM,” *Chinese Journal of Aeronautics*, vol. 32, no. 7, pp. 1727–1732, Jul. 2019, doi: 10.1016/j.cja.2018.08.017.
- [17] B. K. Nagesha, V. Dhinakaran, M. Varsha Shree, K. P. Manoj Kumar, D. Chalawadi, and T. Sathish, “Review on characterization and impacts of the lattice structure in additive manufacturing,” in *Materials Today: Proceedings*, 2020, vol. 21, pp. 916–919. doi: 10.1016/j.matpr.2019.08.158.

- [18] E. Alabot, D. Barba, and R. C. Reed, “Design of metallic bone by additive manufacturing,” *Scr Mater*, vol. 164, pp. 110–114, Apr. 2019, doi: 10.1016/j.scriptamat.2019.01.022.
- [19] S. M. Ahmadi *et al.*, “Mechanical behavior of regular open-cell porous biomaterials made of diamond lattice unit cells,” *J Mech Behav Biomed Mater*, vol. 34, pp. 106–115, Jun. 2014, doi: 10.1016/j.jmbbm.2014.02.003.
- [20] M. Bici *et al.*, “Development of a multifunctional panel for aerospace use through SLM additive manufacturing,” in *Procedia CIRP*, 2018, vol. 67, pp. 215–220. doi: 10.1016/j.procir.2017.12.202.
- [21] K. Boomsma, D. Poulikakos, and F. Zwick, “Metal foams as compact high performance heat exchangers,” *Mechanics of Materials*, vol. 35, no. 12, pp. 1161–1176, Dec. 2003, doi: 10.1016/j.mechmat.2003.02.001.
- [22] J. A. Harris, R. E. Winter, and G. J. McShane, “Impact response of additively manufactured metallic hybrid lattice materials,” *Int J Impact Eng*, vol. 104, pp. 177–191, Jun. 2017, doi: 10.1016/j.ijimpeng.2017.02.007.
- [23] W. Tao and M. C. Leu, “Design of lattice structure for additive manufacturing,” in *International Symposium on Flexible Automation, ISFA 2016*, Dec. 2016, pp. 325–332. doi: 10.1109/ISFA.2016.7790182.
- [24] Y. Huang, M. C. Leu, J. Mazumder, and A. Donmez, “Additive manufacturing: Current state, future potential, gaps and needs, and recommendations,” *Journal of Manufacturing Science and Engineering, Transactions of the ASME*, vol. 137, no. 1, 2015, doi: 10.1115/1.4028725.
- [25] E. Louvis, P. Fox, and C. J. Sutcliffe, “Selective laser melting of aluminium components,” *J Mater Process Technol*, vol. 211, no. 2, pp. 275–284, Feb. 2011, doi: 10.1016/j.jmatprotec.2010.09.019.
- [26] A. Simchi, F. Petzoldt, and H. Pohl, “On the development of direct metal laser sintering for rapid tooling,” *J Mater Process Technol*, vol. 141, no. 3, pp. 319–328, Nov. 2003, doi: 10.1016/S0924-0136(03)00283-8.

- [27] C. Körner, “Additive manufacturing of metallic components by selective electron beam melting - A review,” *International Materials Reviews*, vol. 61, no. 5. Taylor and Francis Ltd., pp. 361–377, 2016. doi: 10.1080/09506608.2016.1176289.
- [28] S. Ghouse, S. Babu, R. J. van Arkel, K. Nai, P. A. Hooper, and J. R. T. Jeffers, “The influence of laser parameters and scanning strategies on the mechanical properties of a stochastic porous material,” *Mater Des*, vol. 131, pp. 498–508, Oct. 2017, doi: 10.1016/j.matdes.2017.06.041.
- [29] W. Gao *et al.*, “The status, challenges, and future of additive manufacturing in engineering,” *CAD Computer Aided Design*, vol. 69, pp. 65–89, Dec. 2015, doi: 10.1016/j.cad.2015.04.001.
- [30] K. Lin, L. Yuan, and D. Gu, “Influence of laser parameters and complex structural features on the bio-inspired complex thin-wall structures fabricated by selective laser melting,” *J Mater Process Technol*, vol. 267, pp. 34–43, May 2019, doi: 10.1016/j.jmatprotec.2018.12.004.
- [31] Sachs E.M., “U.S. Patent No. 6,036,777. Washington, DC: U.S. Patent and Trademark Office,” 2000.
- [32] L. Zhang, S. Zhang, H. Zhu, Z. Hu, G. Wang, and X. Zeng, “Horizontal dimensional accuracy prediction of selective laser melting,” *Mater Des*, vol. 160, pp. 9–20, Dec. 2018, doi: 10.1016/j.matdes.2018.08.059.
- [33] S. Nawada, S. Dimartino, and C. Fee, “Dispersion behavior of 3D-printed columns with homogeneous microstructures comprising differing element shapes,” *Chem Eng Sci*, vol. 164, pp. 90–98, 2017, doi: 10.1016/j.ces.2017.02.012.
- [34] O. Abdulhameed, A. Al-Ahmari, W. Ameen, and S. H. Mian, “Additive manufacturing: Challenges, trends, and applications,” *Advances in Mechanical Engineering*, vol. 11, no. 2, Feb. 2019, doi: 10.1177/1687814018822880.
- [35] A. du Plessis *et al.*, “Beautiful and Functional: A Review of Biomimetic Design in Additive Manufacturing,” *Addit Manuf*, vol. 27, no. March, pp. 408–427, 2019, doi: 10.1016/j.addma.2019.03.033.
- [36] Benyus J.M., *Biomimicry: Innovation inspired by nature*. 1997.

- [37] L. Badarnah and U. Kadri, “A methodology for the generation of biomimetic design concepts,” *Archit Sci Rev*, vol. 58, no. 2, pp. 120–133, Apr. 2015, doi: 10.1080/00038628.2014.922458.
- [38] A. du Plessis, C. Broeckhoven, I. Yadroitsev, I. Yadroitsava, and S. G. le Roux, “Analyzing nature’s protective design: The glyptodont body armor,” *J Mech Behav Biomed Mater*, vol. 82, pp. 218–223, Jun. 2018, doi: 10.1016/j.jmbbm.2018.03.037.
- [39] M. K. Thompson *et al.*, “Design for Additive Manufacturing: Trends, opportunities, considerations, and constraints,” *CIRP Ann Manuf Technol*, vol. 65, no. 2, pp. 737–760, 2016, doi: 10.1016/j.cirp.2016.05.004.
- [40] J. Liu *et al.*, “Current and future trends in topology optimization for additive manufacturing,” *Structural and Multidisciplinary Optimization*, vol. 57, no. 6. Springer Verlag, pp. 2457–2483, Jun. 01, 2018. doi: 10.1007/s00158-018-1994-3.
- [41] D. Brackett, I. Ashcroft, and R. Hague, “Topology optimization for additive manufacturing,” *International Solid Freeform Fabrication Symposium. University of Texas at Austin.*, 2011.
- [42] D. W. Rosen, “Computer-Aided Design for Additive Manufacturing of Cellular Structures,” 2007.
- [43] D. Bhate, C. A. Penick, L. A. Ferry, and C. Lee, “Classification and selection of cellular materials in mechanical design: Engineering and biomimetic approaches,” *Designs*, vol. 3, no. 1. MDPI AG, pp. 1–31, Mar. 01, 2019. doi: 10.3390/designs3010019.
- [44] A. A. Zadpoor, “Mechanical performance of additively manufactured meta-biomaterials,” *Acta Biomater*, vol. 85, pp. 41–59, 2019, doi: 10.1016/j.actbio.2018.12.038.
- [45] L. J. Gibson and M. F. Ashby, “Mechanics of three-dimensional cellular materials,” *Proc R Soc Lond A Math Phys Sci*, vol. 382, no. 1782, pp. 43–59, 1982, doi: 10.1098/rspa.1982.0088.

- [46] V. S. Deshpande, N. A. Fleck, and M. F. Ashby, “Effective properties of the octet-truss lattice material,” *J Mech Phys Solids*, vol. 49, pp. 1747–1769, 2001, [Online]. Available: [www.elsevier.com/locate/jmps](http://www.elsevier.com/locate/jmps)
- [47] M. W. Wu, J. K. Chen, B. H. Lin, P. H. Chiang, and M. K. Tsai, “Compressive fatigue properties of additive-manufactured Ti-6Al-4V cellular material with different porosities,” *Materials Science and Engineering A*, vol. 790, no. May, p. 139695, 2020, doi: 10.1016/j.msea.2020.139695.
- [48] J. K. Chen, M. W. Wu, T. L. Cheng, and P. H. Chiang, “Continuous compression behaviors of selective laser melting Ti-6Al-4V alloy with cuboctahedron cellular structures,” *Materials Science and Engineering C*, vol. 100, pp. 781–788, Jul. 2019, doi: 10.1016/j.msec.2019.03.054.
- [49] R. Hedayati, M. Sadighi, M. Mohammadi-Aghdam, and A. A. Zadpoor, “Mechanical properties of regular porous biomaterials made from truncated cube repeating unit cells: Analytical solutions and computational models,” *Materials Science and Engineering C*, vol. 60, pp. 163–183, 2016, doi: 10.1016/j.msec.2015.11.001.
- [50] S. M. Ahmadi *et al.*, “Additively manufactured open-cell porous biomaterials made from six different space-filling unit cells: The mechanical and morphological properties,” *Materials*, vol. 8, no. 4, pp. 1871–1896, 2015, doi: 10.3390/ma8041871.
- [51] R. Guerra Silva, C. Salinas Estay, G. Morales Pavéz, M. J. Torres, and J. Zahr Viñuela, “Assessment of analytical relationships for mechanical properties of truncated octahedron and diamond lattice structures,” *Mater Today Commun*, vol. 29, Dec. 2021, doi: 10.1016/j.mtcomm.2021.102756.
- [52] D. Qi *et al.*, “Mechanical behaviors of SLM additive manufactured octet-truss and truncated-octahedron lattice structures with uniform and taper beams,” *Int J Mech Sci*, vol. 163, Nov. 2019, doi: 10.1016/j.ijmecsci.2019.105091.
- [53] R. Hedayati, M. Sadighi, M. Mohammadi-Aghdam, and A. A. Zadpoor, “Mechanics of additively manufactured porous biomaterials based on the rhombicuboctahedron unit cell,” *J Mech Behav Biomed Mater*, vol. 53, pp. 272–294, 2016, doi: 10.1016/j.jmbbm.2015.07.013.

- [54] R. Hedayati, M. Sadighi, M. Mohammadi-Aghdam, and A. A. Zadpoor, “Mechanical behavior of additively manufactured porous biomaterials made from truncated cuboctahedron unit cells,” *Int J Mech Sci*, vol. 106, pp. 19–38, Feb. 2016, doi: 10.1016/j.ijmecsci.2015.11.033.
- [55] L. Xiao and W. Song, “Additively-manufactured functionally graded Ti-6Al-4V lattice structures with high strength under static and dynamic loading: Experiments,” *Int J Impact Eng*, vol. 111, pp. 255–272, Jan. 2018, doi: 10.1016/j.ijimpeng.2017.09.018.
- [56] S. Ma, K. Song, J. Lan, and L. Ma, “Biological and mechanical property analysis for designed heterogeneous porous scaffolds based on the refined TPMS,” *J Mech Behav Biomed Mater*, vol. 107, Jul. 2020, doi: 10.1016/j.jmbbm.2020.103727.
- [57] K. Michielsen and S. Kole, “Photonic band gaps in materials with triply periodic surfaces and related tubular structures,” *Phys Rev B Condens Matter Mater Phys*, vol. 68, no. 11, 2003, doi: 10.1103/PhysRevB.68.115107.
- [58] E. Yang *et al.*, “Effect of geometry on the mechanical properties of Ti-6Al-4V Gyroid structures fabricated via SLM: A numerical study,” *Mater Des*, vol. 184, Dec. 2019, doi: 10.1016/j.matdes.2019.108165.
- [59] A. Ataee, Y. Li, D. Fraser, G. Song, and C. Wen, “Anisotropic Ti-6Al-4V gyroid scaffolds manufactured by electron beam melting (EBM) for bone implant applications,” *Mater Des*, vol. 137, pp. 345–354, Jan. 2018, doi: 10.1016/j.matdes.2017.10.040.
- [60] J. Maszybrocka, B. Gapiński, M. Dworak, G. Skrabalak, and A. Stwora, “The manufacturability and compression properties of the Schwarz Diamond type Ti6Al4V cellular lattice fabricated by selective laser melting,” *International Journal of Advanced Manufacturing Technology*, vol. 105, no. 7–8, pp. 3411–3425, Dec. 2019, doi: 10.1007/s00170-019-04422-6.
- [61] C. Yan, L. Hao, A. Hussein, and P. Young, “Ti-6Al-4V triply periodic minimal surface structures for bone implants fabricated via selective laser melting,” *J Mech Behav Biomed Mater*, vol. 51, pp. 61–73, Nov. 2015, doi: 10.1016/j.jmbbm.2015.06.024.

- [62] J. Kadkhodapour, H. Montazerian, A. C. Darabi, A. Zargarian, and S. Schmauder, “The relationships between deformation mechanisms and mechanical properties of additively manufactured porous biomaterials,” *J Mech Behav Biomed Mater*, vol. 70, pp. 28–42, Jun. 2017, doi: 10.1016/j.jmbbm.2016.09.018.
- [63] Z. Li, Z. Chen, X. Chen, and R. Zhao, “Effect of unit configurations and parameters on the properties of Ti–6Al–4V unit-stacked scaffolds: A trade-off between mechanical and permeable performance,” *J Mech Behav Biomed Mater*, vol. 116, Apr. 2021, doi: 10.1016/j.jmbbm.2021.104332.
- [64] X. Guo *et al.*, “Enhancement in the mechanical behaviour of a Schwarz Primitive periodic minimal surface lattice structure design,” *Int J Mech Sci*, vol. 216, Feb. 2022, doi: 10.1016/j.ijmecsci.2021.106977.
- [65] D. W. Lee, K. A. Khan, and R. K. Abu Al-Rub, “Stiffness and yield strength of architectured foams based on the Schwarz Primitive triply periodic minimal surface,” *Int J Plast*, vol. 95, pp. 1–20, Aug. 2017, doi: 10.1016/j.ijplas.2017.03.005.
- [66] T. Gao, K. Liu, X. Wang, Z. Li, and Z. Wang, “Elastic mechanical property hybridization of configuration-varying TPMS with geometric continuity,” *Mater Des*, vol. 221, p. 110995, Sep. 2022, doi: 10.1016/j.matdes.2022.110995.
- [67] K. A. Khan and R. K. Abu Al-Rub, “Time dependent response of architectured Neovius foams,” *Int J Mech Sci*, vol. 126, pp. 106–119, Jun. 2017, doi: 10.1016/j.ijmecsci.2017.03.017.
- [68] A. S. Dalaq, D. W. Abueidda, R. K. Abu Al-Rub, and I. M. Jasiuk, “Finite element prediction of effective elastic properties of interpenetrating phase composites with architectured 3D sheet reinforcements,” *Int J Solids Struct*, vol. 83, pp. 169–182, Apr. 2016, doi: 10.1016/j.ijsolstr.2016.01.011.
- [69] X. Cao *et al.*, “Numerical analysis of the mechanical behavior and energy absorption of a novel P-lattice,” *Thin-Walled Structures*, vol. 157, Dec. 2020, doi: 10.1016/j.tws.2020.107147.
- [70] M. Mahbod and M. Asgari, “Elastic and plastic characterization of a new developed additively manufactured functionally graded porous lattice structure:

- Analytical and numerical models,” *Int J Mech Sci*, vol. 155, pp. 248–266, May 2019, doi: 10.1016/j.ijmecsci.2019.02.041.
- [71] Z. Alomar and F. Concli, “Compressive behavior assessment of a newly developed circular cell-based lattice structure,” *Mater Des*, vol. 205, Jul. 2021, doi: 10.1016/j.matdes.2021.109716.
- [72] V. S. Deshpande, M. F. Ashby, and N. A. Fleck, “Foam topology bending versus stretching dominated architectures,” *Acta Mater*, vol. 49, pp. 1035–1040, 2001, [Online]. Available: [www.elsevier.com/locate/actamat](http://www.elsevier.com/locate/actamat)
- [73] I. Maskery, N. T. Aboulkhair, A. O. Aremu, C. J. Tuck, and I. A. Ashcroft, “Compressive failure modes and energy absorption in additively manufactured double gyroid lattices,” *Addit Manuf*, vol. 16, pp. 24–29, Aug. 2017, doi: 10.1016/j.addma.2017.04.003.
- [74] A. A. Zadpoor and R. Hedayati, “Analytical relationships for prediction of the mechanical properties of additively manufactured porous biomaterials,” *Journal of Biomedical Materials Research - Part A*, vol. 104, no. 12. John Wiley and Sons Inc., pp. 3164–3174, Dec. 01, 2016. doi: 10.1002/jbm.a.35855.
- [75] D. W. Abueidda, M. Bakir, R. K. Abu Al-Rub, J. S. Bergström, N. A. Sobh, and I. Jasiuk, “Mechanical properties of 3D printed polymeric cellular materials with triply periodic minimal surface architectures,” *Mater Des*, vol. 122, pp. 255–267, May 2017, doi: 10.1016/j.matdes.2017.03.018.
- [76] L. Zhang *et al.*, “Energy absorption characteristics of metallic triply periodic minimal surface sheet structures under compressive loading,” *Addit Manuf*, vol. 23, pp. 505–515, Oct. 2018, doi: 10.1016/j.addma.2018.08.007.
- [77] M. Mazur, M. Leary, M. McMillan, S. Sun, D. Shidid, and M. Brandt, “Mechanical properties of Ti6Al4V and AlSi12Mg lattice structures manufactured by Selective Laser Melting (SLM),” in *Laser Additive Manufacturing: Materials, Design, Technologies, and Applications*, Elsevier Inc., 2017, pp. 119–161. doi: 10.1016/B978-0-08-100433-3.00005-1.
- [78] L. Nickels, “AM and aerospace: An ideal combination,” *Metal Powder Report*, vol. 70, no. 6, pp. 300–303, Nov. 2015, doi: 10.1016/j.mprp.2015.06.005.

- [79] J. Zhou, P. Shrotriya, and W. O. Soboyejo, “On the deformation of aluminum lattice block structures: From struts to structures,” in *Mechanics of Materials*, Aug. 2004, vol. 36, no. 8, pp. 723–737. doi: 10.1016/j.mechmat.2003.08.007.
- [80] M. Helou and S. Kara, “Design, analysis and manufacturing of lattice structures: An overview,” *Int J Comput Integr Manuf*, vol. 31, no. 3, pp. 243–261, 2018, doi: 10.1080/0951192X.2017.1407456.
- [81] Z. Ozdemir *et al.*, “Energy absorption in lattice structures in dynamics: Experiments,” *Int J Impact Eng*, vol. 89, pp. 49–61, Mar. 2016, doi: 10.1016/j.ijimpeng.2015.10.007.
- [82] O. L. A. Harrysson, O. Cansizoglu, D. J. Marcellin-Little, D. R. Cormier, and H. A. West, “Direct metal fabrication of titanium implants with tailored materials and mechanical properties using electron beam melting technology,” *Materials Science and Engineering C*, vol. 28, no. 3, pp. 366–373, 2008, doi: 10.1016/j.msec.2007.04.022.
- [83] H. M. A. Kolken *et al.*, “Additively manufactured space-filling meta-implants,” *Acta Biomater*, vol. 125, pp. 345–357, Apr. 2021, doi: 10.1016/j.actbio.2021.02.020.
- [84] E. Liverani, G. Rogati, S. Pagani, S. Brogini, A. Fortunato, and P. Caravaggi, “Mechanical interaction between additive-manufactured metal lattice structures and bone in compression: implications for stress shielding of orthopaedic implants,” *J Mech Behav Biomed Mater*, vol. 121, Sep. 2021, doi: 10.1016/j.jmbbm.2021.104608.
- [85] X. Pei *et al.*, “Fabrication of customized Ti6Al4V heterogeneous scaffolds with selective laser melting: Optimization of the architecture for orthopedic implant applications,” *Acta Biomater*, vol. 126, pp. 485–495, May 2021, doi: 10.1016/j.actbio.2021.03.040.
- [86] G. Epasto, F. Distefano, R. Mineo, and E. Guglielmino, “Subject-specific finite element analysis of a lumbar cage produced by electron beam melting,” *Med Biol Eng Comput*, vol. 57, no. 12, pp. 2771–2781, Dec. 2019, doi: 10.1007/s11517-019-02078-8.

- [87] H. Gao, X. Li, C. Wang, P. Ji, and C. Wang, “Mechanobiologically optimization of a 3D titanium-mesh implant for mandibular large defect: A simulated study,” *Materials Science and Engineering C*, vol. 104, Nov. 2019, doi: 10.1016/j.msec.2019.109934.
- [88] F. Günther, M. Wagner, S. Pilz, A. Gebert, and M. Zimmermann, “Design procedure for triply periodic minimal surface based biomimetic scaffolds,” *J Mech Behav Biomed Mater*, vol. 126, Feb. 2022, doi: 10.1016/j.jmbbm.2021.104871.
- [89] X. Wang *et al.*, “Topological design and additive manufacturing of porous metals for bone scaffolds and orthopaedic implants: A review,” *Biomaterials*, vol. 83. Elsevier Ltd, pp. 127–141, Mar. 01, 2016. doi: 10.1016/j.biomaterials.2016.01.012.
- [90] N. Abbasi, S. Hamlet, R. M. Love, and N. T. Nguyen, “Porous scaffolds for bone regeneration,” *Journal of Science: Advanced Materials and Devices*, vol. 5, no. 1, pp. 1–9, 2020, doi: 10.1016/j.jsamd.2020.01.007.
- [91] S. Bose, S. Vahabzadeh, and A. Bandyopadhyay, “Bone tissue engineering using 3D printing,” *Materials Today*, vol. 16, no. 12. pp. 496–504, Dec. 2013. doi: 10.1016/j.mattod.2013.11.017.
- [92] M. Long and H. J. Rack, “Titanium alloys in total joint replacement-a materials science perspective,” 1998.
- [93] S. J. Hollister, “Scaffold design and manufacturing: From concept to clinic,” *Advanced Materials*, vol. 21, no. 32–33. pp. 3330–3342, Sep. 04, 2009. doi: 10.1002/adma.200802977.
- [94] S. Ghose *et al.*, “The design and in vivo testing of a locally stiffness-matched porous scaffold,” *Appl Mater Today*, vol. 15, pp. 377–388, Jun. 2019, doi: 10.1016/j.apmt.2019.02.017.
- [95] Y. Efraim *et al.*, “3D Structure and Processing Methods Direct the Biological Attributes of ECM-Based Cardiac Scaffolds,” *Sci Rep*, vol. 9, no. 1, pp. 1–13, 2019, doi: 10.1038/s41598-019-41831-9.
- [96] A. I. Itä Lä, H. O. Ylä, C. Ekholm, K. H. Karlsson, and H. T. Aro, “Pore Diameter of More Than 100 m Is Not Requisite for Bone Ingrowth in Rabbits,” 2001.

- [97] F. Bai *et al.*, “The correlation between the internal structure and vascularization of controllable porous bioceramic materials in vivo: A quantitative study,” *Tissue Eng Part A*, vol. 16, no. 12, pp. 3791–3803, Dec. 2010, doi: 10.1089/ten.tea.2010.0148.
- [98] N. Taniguchi *et al.*, “Effect of pore size on bone ingrowth into porous titanium implants fabricated by additive manufacturing: An in vivo experiment,” *Materials Science and Engineering C*, vol. 59, pp. 690–701, Feb. 2016, doi: 10.1016/j.msec.2015.10.069.
- [99] Z. Zhang *et al.*, “Hierarchical tailoring of strut architecture to control permeability of additive manufactured titanium implants,” *Materials Science and Engineering C*, vol. 33, no. 7, pp. 4055–4062, Oct. 2013, doi: 10.1016/j.msec.2013.05.050.
- [100] A. Aydin and J. M. Degriff, “Evolution of Polygonal Fracture Patterns in Lava Flows,” 1988.
- [101] D. L. Peck and T. Minakami, “The formation of columnar joints in the upper part of Kilauean lava lakes, Hawaii,” *Geol Soc Am Bull*, vol. 79, no. 9, pp. 1151–1166, 1968.
- [102] N. H. Gray, J. B. Anderson, J. D. Devine, and J. M. Kwasnik, “Topological properties of random crack networks,” *Journal of the International Association for Mathematical Geology*, vol. 8, no. 6, pp. 617–626, 1976.
- [103] G. Hetényi, B. Taisne, F. Garel, É. Médard, S. Bosshard, and H. B. Mattsson, “Scales of columnar jointing in igneous rocks: Field measurements and controlling factors,” *Bull Volcanol*, vol. 74, no. 2, pp. 457–482, Mar. 2012, doi: 10.1007/s00445-011-0534-4.
- [104] G. C. Sih, “Energy-density concept in fracture mechanics,” Pergamon Press, 1973.
- [105] G. Epasto, G. Palomba, D. D’Andrea, E. Guglielmino, S. di Bella, and F. Traina, “Ti-6Al-4V ELI microlattice structures manufactured by electron beam melting: Effect of unit cell dimensions and morphology on mechanical behaviour,” *Materials Science and Engineering A*, vol. 753, pp. 31–41, Apr. 2019, doi: 10.1016/j.msea.2019.03.014.

- [106] R. Hedayati, M. Sadighi, M. Mohammadi-Aghdam, and A. A. Zadpoor, “Effect of mass multiple counting on the elastic properties of open-cell regular porous biomaterials,” *Mater Des*, vol. 89, pp. 9–20, Jan. 2016, doi: 10.1016/j.matdes.2015.09.052.
- [107] F. Perez-Boerema, M. Barzegari, and L. Geris, “A flexible and easy-to-use open-source tool for designing functionally graded 3D porous structures,” *Virtual Phys Prototyp*, vol. 17, no. 3, pp. 682–699, 2022, doi: 10.1080/17452759.2022.2048956.
- [108] O. Al-Ketan and R. K. Abu Al-Rub, “MSLattice: A free software for generating uniform and graded lattices based on triply periodic minimal surfaces,” *Material Design and Processing Communications*, vol. 3, no. 6, Dec. 2021, doi: 10.1002/mdp2.205.
- [109] T. Tancogne-Dejean, A. B. Spierings, and D. Mohr, “Additively-manufactured metallic micro-lattice materials for high specific energy absorption under static and dynamic loading,” *Acta Mater*, vol. 116, pp. 14–28, Sep. 2016, doi: 10.1016/j.actamat.2016.05.054.
- [110] F. Distefano, E. Guglielmino, R. Mineo, and G. Epasto, “Mechanical and morphological characterization of BCC - derived unit cells for biomedical devices,” *Procedia Structural Integrity*, vol. 41, pp. 470–485, 2022, doi: 10.1016/j.prostr.2022.05.053.
- [111] R. Gümrük, R. A. W. Mines, and S. Karadeniz, “Static mechanical behaviours of stainless steel micro-lattice structures under different loading conditions,” *Materials Science and Engineering A*, vol. 586, pp. 392–406, 2013, doi: 10.1016/j.msea.2013.07.070.
- [112] H. Lei *et al.*, “Evaluation of compressive properties of SLM-fabricated multi-layer lattice structures by experimental test and  $\mu$ -CT-based finite element analysis,” *Mater Des*, vol. 169, May 2019, doi: 10.1016/j.matdes.2019.107685.
- [113] M. M. Shalabi, A. Gortemaker, M. A. V. Hof, J. A. Jansen, and N. H. J. Creugers, “Implant Surface Roughness and Bone Healing: a Systematic Review,” *J Dent Res*, vol. 85, no. 6, pp. 496–500, Jun. 2006, doi: 10.1177/154405910608500603.

- [114] X. P. Tan, Y. J. Tan, C. S. L. Chow, S. B. Tor, and W. Y. Yeong, "Metallic powder-bed based 3D printing of cellular scaffolds for orthopaedic implants: A state-of-the-art review on manufacturing, topological design, mechanical properties and biocompatibility," *Materials Science and Engineering C*, vol. 76. Elsevier Ltd, pp. 1328–1343, Jul. 01, 2017. doi: 10.1016/j.msec.2017.02.094.
- [115] S. Y. Choy, C. N. Sun, K. F. Leong, and J. Wei, "Compressive properties of Ti-6Al-4V lattice structures fabricated by selective laser melting: Design, orientation and density," *Addit Manuf*, vol. 16, pp. 213–224, 2017, doi: 10.1016/j.addma.2017.06.012.
- [116] L. Yang *et al.*, "Insights into unit cell size effect on mechanical responses and energy absorption capability of titanium graded porous structures manufactured by laser powder bed fusion," *J Mech Behav Biomed Mater*, vol. 109, Sep. 2020, doi: 10.1016/j.jmbbm.2020.103843.
- [117] M. Leary *et al.*, "Inconel 625 lattice structures manufactured by selective laser melting (SLM): Mechanical properties, deformation and failure modes," *Mater Des*, vol. 157, pp. 179–199, Nov. 2018, doi: 10.1016/j.matdes.2018.06.010.
- [118] M. Sadati, S. Ghofrani, and A. A. Mehrizi, "Investigation of porous cells interface on elastic property of orthopedic implants: Numerical and experimental studies," *J Mech Behav Biomed Mater*, vol. 120, Aug. 2021, doi: 10.1016/j.jmbbm.2021.104595.
- [119] F. Wang, J. Zhao, N. Zhu, and Z. Li, "A comparative study on Johnson-Cook constitutive modeling for Ti-6Al-4V alloy using automated ball indentation (ABI) technique," *J Alloys Compd*, vol. 633, pp. 220–228, Jun. 2015, doi: 10.1016/j.jallcom.2015.01.284.
- [120] Y. Zhang, J. C. Outeiro, and T. Mabrouki, "On the selection of Johnson-Cook constitutive model parameters for Ti-6Al-4V using three types of numerical models of orthogonal cutting," in *Procedia CIRP*, 2015, vol. 31, pp. 112–117. doi: 10.1016/j.procir.2015.03.052.
- [121] G. R. Johnson, "FRACTURE CHARACTERISTICS OF THREE METALS SUBJECTED TO VARIOUS STRAINS, STRAIN RATES, TEMPERATURES AND PRESSURES," 1985.

- [122] J. Cai, F. Li, T. Liu, B. Chen, and M. He, “Constitutive equations for elevated temperature flow stress of Ti-6Al-4V alloy considering the effect of strain,” *Mater Des*, vol. 32, no. 3, pp. 1144–1151, Mar. 2011, doi: 10.1016/j.matdes.2010.11.004.
- [123] N. Kotkunde, A. D. Deole, A. K. Gupta, and S. K. Singh, “Comparative study of constitutive modeling for Ti-6Al-4V alloy at low strain rates and elevated temperatures,” *Mater Des*, vol. 55, pp. 999–1005, 2014, doi: 10.1016/j.matdes.2013.10.089.
- [124] X. Yan *et al.*, “Mechanical and in vitro study of an isotropic Ti6Al4V lattice structure fabricated using selective laser melting,” *J Alloys Compd*, vol. 782, pp. 209–223, Apr. 2019, doi: 10.1016/j.jallcom.2018.12.220.
- [125] M. Çakircali, C. Kiliçaslan, M. Güden, E. Kiranli, V. Y. Shchukin, and V. v. Petronko, “Cross wedge rolling of a Ti6Al4V (ELI) alloy: The experimental studies and the finite element simulation of the deformation and failure,” *International Journal of Advanced Manufacturing Technology*, vol. 65, no. 9–12, pp. 1273–1287, Apr. 2013, doi: 10.1007/s00170-012-4256-3.
- [126] W.-S. Lee and C.-F. Lin, “Plastic deformation and fracture behaviour of Ti-6Al-4V alloy loaded with high strain rate under various temperatures,” 1998.
- [127] H. W. Meyer and D. S. Kleponis, “MODELING THE HIGH STRAIN RATE BEHAVIOR OF TITANIUM UNDERGOING BALLISTIC IMPACT AND PENETRATION,” 2001. [Online]. Available: [www.eisevier.com/locaite/ijimpeng](http://www.eisevier.com/locaite/ijimpeng)
- [128] F. Ducobu, E. Rivière-Lorphèvre, and E. Filippi, “On the importance of the choice of the parameters of the Johnson-Cook constitutive model and their influence on the results of a Ti6Al4V orthogonal cutting model,” *Int J Mech Sci*, vol. 122, pp. 143–155, Mar. 2017, doi: 10.1016/j.ijmecsci.2017.01.004.
- [129] A. S. Khoddami, D. Salimi-Majd, and B. Mohammadi, “Finite element and experimental investigation of multiple solid particle erosion on Ti-6Al-4V titanium alloy coated by multilayer wear-resistant coating,” *Surf Coat Technol*, vol. 372, pp. 173–189, Aug. 2019, doi: 10.1016/j.surfcoat.2019.05.042.
- [130] F. Tamburrino, S. Graziosi, and M. Bordegoni, “The design process of additively manufactured mesoscale lattice structures: A review,” *Journal of Computing and*

- Information Science in Engineering*, vol. 18, no. 4. American Society of Mechanical Engineers (ASME), Dec. 01, 2018. doi: 10.1115/1.4040131.
- [131] Y. L. Wei, Q. S. Yang, X. Liu, and R. Tao, “Multi-bionic mechanical metamaterials: A composite of FCC lattice and bone structures,” *Int J Mech Sci*, vol. 213, Jan. 2022, doi: 10.1016/j.ijmecsci.2021.106857.
- [132] K. Michielsen and S. Kole, “Photonic band gaps in materials with triply periodic surfaces and related tubular structures,” *Phys Rev B Condens Matter Mater Phys*, vol. 68, no. 11, 2003, doi: 10.1103/PhysRevB.68.115107.
- [133] R. J. Mobbs, K. Phan, G. Malham, K. Seex, and P. J. Rao, “Lumbar interbody fusion: techniques, indications and comparison of interbody fusion options including PLIF, TLIF, MI-TLIF, OLIF/ATP, LLIF and ALIF.,” *J Spine Surg*, vol. 1, no. 1, pp. 2–18, 2015, doi: 10.3978/j.issn.2414-469X.2015.10.05.
- [134] di Paola C.P. and Molinari R.W., “Posterior Lumbar Interbody Fusion,” *JAAOS-Journal of the American Academy of Orthopaedic Surgeons*, vol. 16, no. 3, pp. 130–139, 2008.
- [135] J. X. Julian Li, R. J. Mobbs, and K. Phan, “Morphometric MRI Imaging Study of the Corridor for the Oblique Lumbar Interbody Fusion Technique at L1-L5,” *World Neurosurg*, vol. 111, pp. e678–e685, Mar. 2018, doi: 10.1016/j.wneu.2017.12.136.
- [136] B. Kwon and D. H. Kim, “Lateral lumbar interbody fusion: Indications, outcomes, and complications,” *Journal of the American Academy of Orthopaedic Surgeons*, vol. 24, no. 2. Lippincott Williams and Wilkins, pp. 96–105, Feb. 01, 2016. doi: 10.5435/JAAOS-D-14-00208.
- [137] B. M. Ozgur, H. E. Aryan, L. Pimenta, and W. R. Taylor, “Extreme Lateral Interbody Fusion (XLIF): a novel surgical technique for anterior lumbar interbody fusion,” *Spine Journal*, vol. 6, no. 4. pp. 435–443, Jul. 2006. doi: 10.1016/j.spinee.2005.08.012.
- [138] L. Hackenberg, H. Halm, V. Bullmann, V. Vieth, M. Schneider, and U. Liljenqvist, “Transforaminal lumbar interbody fusion: A safe technique with satisfactory three to five year results,” *European Spine Journal*, vol. 14, no. 6, pp. 551–558, Aug. 2005, doi: 10.1007/s00586-004-0830-1.

- [139] Holly L.T., Schwender J.D., Rouben D.P., and Foley K.T., “Minimally invasive transforaminal lumbar interbody fusion—indications, technique, and complications,” *Neurosurg Focus*, vol. 20, no. 3, pp. 1–5, 2006.
- [140] C. B. Theodotou and M. Y. Wang, “Minimally invasive transforaminal lumbar interbody fusion,” *Semin Spine Surg*, vol. 33, no. 3, pp. 1–6, 2021, doi: 10.1016/j.semss.2021.100888.
- [141] I. M. Punt *et al.*, “Complications and reoperations of the SB Charité lumbar disc prosthesis: Experience in 75 patients,” *European Spine Journal*, vol. 17, no. 1, pp. 36–43, 2008, doi: 10.1007/s00586-007-0506-8.
- [142] S. A. Rundell, J. E. Isaza, and S. M. Kurtz, “Biomechanical evaluation of a spherical lumbar interbody device at varying levels of subsidence,” *SAS J*, vol. 5, no. 1, pp. 16–25, 2011, doi: 10.1016/j.esas.2010.12.001.
- [143] M. F. Dvorak, B. K. Kwon, C. G. Fisher, H. L. Eiserloh, M. Boyd, and P. C. Wing, “Effectiveness of titanium mesh cylindrical cages in anterior column reconstruction after thoracic and lumbar vertebral body resection,” *Spine (Phila Pa 1976)*, vol. 28, no. 9, pp. 902–908, 2003, doi: 10.1097/00007632-200305010-00012.
- [144] J. R. Stieber and G. D. Donald, “Early failure of lumbar disc replacement: Case report and review of the literature,” *J Spinal Disord Tech*, vol. 19, no. 1, pp. 55–60, 2006, doi: 10.1097/01.bsd.0000163414.53732.a3.
- [145] C. Ji *et al.*, “Risk factors for subsidence of titanium mesh cage following single-level anterior cervical corpectomy and fusion,” *BMC Musculoskelet Disord*, vol. 21, no. 1, p. 32, 2020, doi: 10.1186/s12891-019-3036-8.
- [146] A. I. Hussein, Z. D. Mason, and E. F. Morgan, “Presence of intervertebral discs alters observed stiffness and failure mechanisms in the vertebra,” *J Biomech*, vol. 46, no. 10, pp. 1683–1688, 2013, doi: 10.1016/j.jbiomech.2013.04.004.
- [147] A. Joshi, C. J. Massey, A. Karduna, E. Vresilovic, and M. Marcolongo, “The effect of nucleus implant parameters on the compressive mechanics of the lumbar intervertebral disc: A finite element study,” *J Biomed Mater Res B Appl Biomater*, vol. 90 B, no. 2, pp. 596–607, 2009, doi: 10.1002/jbm.b.31322.

- [148] A. Calvo-Echenique, J. Cegoñino, R. Chueca, and A. Pérez-del Palomar, “Stand-alone lumbar cage subsidence: A biomechanical sensitivity study of cage design and placement.,” *Comput Methods Programs Biomed*, vol. 162, pp. 211–219, 2018, doi: 10.1016/j.cmpb.2018.05.022.
- [149] N. Bocahut *et al.*, “Incidence and impact of implant subsidence after stand-alone lateral lumbar interbody fusion,” *Orthopaedics and Traumatology: Surgery and Research*, vol. 104, no. 3, pp. 405–410, 2018, doi: 10.1016/j.otsr.2017.11.018.
- [150] C. Adam, M. Pearcy, and P. McCombe, “Stress analysis of interbody fusion - Finite element modelling of intervertebral implant and vertebral body,” *Clinical Biomechanics*, vol. 18, no. 4, pp. 265–272, 2003, doi: 10.1016/S0268-0033(03)00022-6.
- [151] S. Rastegar, P. J. Arnoux, X. Wang, and C. É. Aubin, “Biomechanical analysis of segmental lumbar lordosis and risk of cage subsidence with different cage heights and alternative placements in transforaminal lumbar interbody fusion,” *Comput Methods Biomech Biomed Engin*, vol. 0, no. 0, pp. 1–11, 2020, doi: 10.1080/10255842.2020.1737027.
- [152] M. H. Mohammad-Shahi, V. S. Nikolaou, D. Giannitsios, J. Ouellet, and P. F. Jarzem, “The effect of angular mismatch between vertebral endplate and vertebral body replacement endplate on implant subsidence,” *J Spinal Disord Tech*, vol. 26, no. 5, pp. 268–273, 2013, doi: 10.1097/BSD.0b013e3182425eab.
- [153] J. H. Lee, D. W. Jeon, S. J. Lee, B. S. Chang, and C. K. Lee, “Fusion rates and subsidence of morselized local bone grafted in titanium cages in posterior lumbar interbody fusion using quantitative three-dimensional computed tomography scans,” *Spine (Phila Pa 1976)*, vol. 35, no. 15, pp. 1460–1465, 2010, doi: 10.1097/BRS.0b013e3181c4baf5.
- [154] J. S. Tan, C. S. Bailey, M. F. Dvorak, C. G. Fisher, and T. R. Oxland, “Interbody device shape and size are important to strengthen the vertebra-implant interface,” *Spine (Phila Pa 1976)*, vol. 30, no. 6, pp. 638–644, 2005, doi: 10.1097/01.brs.0000155419.24198.35.
- [155] C. C. Hsu, “Shape optimization for the subsidence resistance of an interbody device using simulation-based genetic algorithms and experimental validation,”

- Journal of Orthopaedic Research*, vol. 31, no. 7, pp. 1158–1163, 2013, doi: 10.1002/jor.22317.
- [156] V. K. Goel, M. M. Panjabi, A. G. Patwardhan, A. P. Dooris, and H. Serhan, “Test protocols for evaluation of spinal implants,” *Journal of Bone and Joint Surgery - Series A*, vol. 88, no. SUPPL. 2, pp. 103–109, 2006, doi: 10.2106/JBJS.E.01363.
- [157] W. Yuan, A. K. Kaliya-Perumal, S. M. Chou, and J. Y. L. Oh, “Does Lumbar Interbody Cage Size Influence Subsidence? A Biomechanical Study,” *Spine (Phila Pa 1976)*, vol. 45, no. 2, pp. 88–95, 2020, doi: 10.1097/BRS.0000000000003194.
- [158] A. C. M. Chong, S. W. Harrer, M. H. Heggeness, and P. H. Wooley, “Biomechanical evaluation of CIBOR spine interbody fusion device,” *J Biomed Mater Res B Appl Biomater*, vol. 105, no. 5, pp. 1157–1168, 2017, doi: 10.1002/jbm.b.33665.
- [159] K. M. Lim, T. H. Park, S. J. Lee, and S. J. Park, “Design and Biomechanical Verification of Additive Manufactured Composite Spinal Cage Composed of Porous Titanium Cover and PEEK Body,” *Applied Sciences (Switzerland)*, vol. 9, no. 20, 2019, doi: 10.3390/app9204258.
- [160] Z. Zhang, H. Li, G. R. Fogel, D. Xiang, Z. Liao, and W. Liu, “Finite element model predicts the biomechanical performance of transforaminal lumbar interbody fusion with various porous additive manufactured cages,” *Comput Biol Med*, vol. 95, pp. 167–174, Apr. 2018, doi: 10.1016/j.combiomed.2018.02.016.
- [161] F. Rupp, L. Scheideler, D. Rehbein, D. Axmann, and J. Geis-Gerstorfer, “Roughness induced dynamic changes of wettability of acid etched titanium implant modifications,” *Biomaterials*, vol. 25, no. 7–8, pp. 1429–1438, 2004, doi: 10.1016/j.biomaterials.2003.08.015.
- [162] V. Palepu, M. D. Helgeson, M. Molyneaux-Francis, and S. Nagaraja, “The effects of bone microstructure on subsidence risk for ALIF, LLIF, PLIF, and TLIF spine cages,” *J Biomech Eng*, vol. 141, no. 3, 2019, doi: 10.1115/1.4042181.
- [163] K. Han, A. Rohlmann, T. Zander, and W. R. Taylor, “Lumbar spinal loads vary with body height and weight,” *Med Eng Phys*, vol. 35, no. 7, pp. 969–977, 2013, doi: 10.1016/j.medengphy.2012.09.009.

- [164] H. Y. Yu, Z. B. Cai, Z. R. Zhou, and M. H. Zhu, “Fretting behavior of cortical bone against titanium and its alloy,” *Wear*, vol. 259, no. 7–12, pp. 910–918, 2005, doi: 10.1016/j.wear.2005.01.037.
- [165] J. H. Kuiper and R. Huiskes, “Friction and Stem Stiffness Affect Dynamic Interface Motion in Total Hip Replacement.”
- [166] M. Viceconti, R. Muccini, M. Bernakiewicz, M. Baleani, and L. Cristofolini, “Large-sliding contact elements accurately predict levels of bone}implant micromotion relevant to osseointegration,” 2000. [Online]. Available: <http://www.elsevier.nl:80/inca/>
- [167] P. B. Suh, C. Puttlitz, C. Lewis, B. S. Bal, and K. McGilvray, “The effect of cervical interbody cage morphology, material composition, and substrate density on cage subsidence,” *Journal of the American Academy of Orthopaedic Surgeons*, vol. 25, no. 2, pp. 160–168, 2017, doi: 10.5435/JAAOS-D-16-00390.
- [168] M. Niinomi, “Mechanical properties of biomedical titanium alloys,” *Materials Science and Engineering: A*, vol. 243, no. 1–2, pp. 231–236, Mar. 1998, doi: 10.1016/S0921-5093(97)00806-X.
- [169] M. A. Adams, D. S. McNally, H. Chinn, and P. Dolan, “Posture and the compressive strength of the lumbar spine,” *Clinical Biomechanics*, vol. 9, no. 1, pp. 5–14, Jan. 1994, doi: 10.1016/0268-0033(94)90052-3.
- [170] International Organization for Standardization, “Mechanical testing of metals - Ductility testing - Compression test for porous and cellular metal,” *ISO standard 13314*, 2011.
- [171] A. Ataee, Y. Li, M. Brandt, and C. Wen, “Ultrahigh-strength titanium gyroid scaffolds manufactured by selective laser melting (SLM) for bone implant applications,” *Acta Mater*, vol. 158, pp. 354–368, Oct. 2018, doi: 10.1016/j.actamat.2018.08.005.

# LIST OF PUBLICATIONS

## Patent

- Cella a struttura ottagonale e struttura reticolare comprendente detta cella per applicazioni biomedicali

Industrial Patent application number: 102022000010730

Presented on: 25 May 2022

## Journal articles

Published:

- Distefano, F., Epasto, G., Guglielmino, E., Amata, A., & Mineo, R. (2022). Subsidence of a partially porous titanium lumbar cage produced by electron beam melting technology. *Journal of Biomedical Materials Research Part B: Applied Biomaterials*.

<https://doi.org/10.1002/jbm.b.35176>

- Mozafari, H., Distefano, F., Epasto, G., Gu, L., Linul, E., & Crupi, V. (2022). Design of an Innovative Hybrid Sandwich Protective Device for Offshore Structures. *Journal of Marine Science and Engineering*, 10(10), 1385.

<https://doi.org/10.3390/jmse10101385>

- Distefano, F., Guglielmino, E., Mineo, R., & Epasto, G. (2022). Mechanical and morphological characterization of BCC-derived unit cells for biomedical devices. *Procedia Structural Integrity*, 41, 470-485.

<https://doi.org/10.1016/j.prostr.2022.05.053>

Scopus ID: 1-s2.0-S245232162200511

- Epasto, G., Distefano, F., Mozafari, H., Linul, E., & Crupi, V. (2021). Nondestructive evaluation of aluminium foam panels subjected to impact

loading. *Applied Sciences*, 11(3), 1148.

<https://doi.org/10.3390/app11031148>

Scopus ID: 2-s2.0-85100101020

Journal Impact Factor: 2,679

- Epasto, G., Distefano, F., Gu, L., Mozafari, H., & Linul, E. (2020). Design and optimization of Metallic Foam Shell protective device against flying ballast impact damage in railway axles. *Materials & Design*, 196, 109120..  
<https://doi.org/10.1016/j.matdes.2020.109120>  
Scopus ID: 2-s2.0-85090560916  
Journal Impact Factor: 6,289
  
- Epasto, G., Distefano, F., Mineo, R., & Guglielmino, E. (2019). Subject-specific finite element analysis of a lumbar cage produced by electron beam melting. *Medical & Biological Engineering & Computing*, 57(12), 2771-2781.  
<https://doi.org/10.1007/s11517-019-02078-8>  
Scopus ID: 2-s2.0-85075195966  
Journal Impact Factor: 2,039

Revision:

- Mechanical behaviour of a novel biomimetic lattice structure for bone scaffold  
Authors: Distefano F., Mineo R., & Epasto G.  
Submitted to: Journal of the Mechanical Behavior of Biomedical Materials

## Conferences

Oral presentation:

- Experimental mechanical analysis of 3D-printed titanium gyroid scaffolds  
Presentation in: National Conference AIAS 2022 (Padova, Italy) – 9 September 2022  
Authors: Distefano F., Perez-Boerema F., Geris L., Epasto G.

- Additively manufactured microlattice structures for an innovative intervertebral device  
Presentation in: ESB 2022 – 27<sup>th</sup> Congress of the European Society of Biomechanics (Porto, Portugal) – 26 June 2022  
Authors: Distefano F., Epasto G., Guglielmino E., & Mineo R.
  
- Mechanical and morphological characterization of BCC - derived unit cells for biomedical devices  
Presentation in: MedFract2 Conference (Catania, Italy) – 15 February 2022  
Authors: Distefano F., Epasto G., Guglielmino E., & Mineo R.
  
- Progettazione di una nuova struttura microreticolare per applicazioni in campo biomeccanico  
Presentation in: Virtual National Conference AIAS 2021 – 2 September 2021  
Authors: Distefano F., Epasto G., Guglielmino E., & Mineo R.

#### Participation:

- Analisi del fenomeno della subsidenza di dispositivi lombari prodotti mediante additive manufacturing  
Participation at: Virtual National Conference AIAS 2020 – 4 September 2020  
Authors: Distefano F., Epasto G., Guglielmino E., Amata A., & Mineo R.
  
- Analisi agli elementi finiti di un dispositivo vertebrale prodotto mediante Additive Manufacturing  
Participation at: National Conference AIAS 2019 (Assisi (PG), Italy) – 5 September 2019  
Authors: Epasto G., Distefano F., Mineo R., & Guglielmino E.

Submitted abstract:

- A Round-Robin Three- and Four-Point Bending Test of a Bone Surrogate with Finite Element Analysis

Submitted to: ORS 2023 Annual Meeting – Orthopaedic Research Society  
(Dallas, Texas) – 10-14 February 2023

Authors: Zojaji M., Roth J., Edwards B., Quenneville C., Kluess D., Epasto G., Distefano F., Pasta S., & Ploeg H.